

The Pennsylvania State University

The Graduate School

Department of Electrical Engineering

**MODULATING THE RESPONSE OF OPTICAL NANOSTRUCTURES BY  
INTEGRATING NOVEL PLASMONIC BUILDING BLOCKS**

A Dissertation in

Electrical Engineering

by

Yu Yuwen

© 2014 Yu Yuwen

Submitted in Partial Fulfillment  
of the Requirements  
for the Degree of

Doctor of Philosophy

December 2014

The dissertation of Yu Yuwen was reviewed and approved\* by the following:

Theresa Mayer  
Professor of Electrical Engineering  
Dissertation Advisor  
Chair of Committee

Joan Redwing  
Professor of Electrical Engineering

Douglas Werner  
Professor of Electrical Engineering

Thomas Mallouk  
Professor of Chemical Engineering

Dennis Lin  
Professor of Statistics

Kultegin Aydin  
Professor of Electrical Engineering  
Head of the Department of Electrical Engineering

\*Signatures are on file in the Graduate School

## ABSTRACT

Plasmonic nanostructures are of great interest due to the broad range of applications from biodetection to metamaterial. The desired optical functionality of these nanostructures can only be realized if the designed geometries and constituent material quality are accurately reproduced experimentally. This dissertation research developed new fabrication methods to create planar and freestanding plasmonic nanostructures, including two-dimensional (2D) planar gold (Au) nanoparticle quasicrystals, one-dimensional (1D) Au nanoparticle arrays, and ring-loaded Au nanoparticle dimer nanoantennas. The measured and modeled optical properties of each type of structure were found to be in strong agreement with one another, thereby confirming the effectiveness of the fabrication approaches in reproducing the designed structure.

In Chapter 2, planar 2D plasmonic quasicrystal arrays composed of spherical Au nanoparticles were created by Au-enhanced oxidation of lithographically patterned stacks of evaporated amorphous silicon (*a*-Si) and Au thin films. In contrast to 2D periodic plasmonic structures, which can be accurately simulated for arbitrarily shaped nanoparticles, computationally efficient models for quasicrystals require spherical particle geometries. Using the process developed in this research, broadband Ammann-Beenker and multiband Penrose plasmonic quasicrystals were fabricated and optically characterized. The measured transmission spectra of the fabricated structures agreed well with simulation, thereby enabling an experimental validation of the modeled interaction between the plasmonic and photonic modes of the two structures.

In Chapter 3, freestanding 1D Au nanoparticle arrays encapsulated within a silicon dioxide (SiO<sub>2</sub>) shell were produced by Au-enhanced oxidation of Au-coated, surface modulated Si nanowires. This lithography-free process overcomes the linear relationship between nanoparticle diameter and interparticle spacing imposed by the Rayleigh instability, and provides accurate and reproducible control of both of these parameters over a wide range of particle diameters and

spacings. The modeled optical properties of fabricated 1D arrays were confirmed experimentally by extinction measurements of a randomly oriented ensemble of wires as well as by scanning transmission electron microscopy (STEM) electron energy loss spectra (EELS) and energy filtered transmission electron microscopy (EFTEM) analysis of individual wire arrays.

In Chapter 4, a nanoring-loaded dimer nanoantenna was designed to give a multiband optical plasmonic response. The center wavelength and bandwidth of the two bands was varied by modifying the nanoring inner diameter. A top-down process was optimized to reproducibly fabricate the ring-loaded nanoantenna with sub-10 nm wide gaps between the three particles and an inner/outer nanoring diameter of 30nm and 55nm, respectively. Electromagnetic modeling showed that the multi-band response originated from differences in coupling between the nanoring and nanoparticle building blocks for the long- and short-wavelength resonances. The optical response was also understood by modeling the electric/magnetic field and charge distribution of the nanoantennas at the two resonant wavelengths.

## TABLE OF CONTENTS

List of Figures .....	vii
List of Tables .....	xiii
Acknowledgements.....	xiv
Chapter 1 Introduction .....	1
1.1 Background and Motivation.....	1
1.1.1 Analytical Methods for Predicting the Performance of Plasmonic Nanostructures.....	3
1.1.2 Fabrication Methods for Plasmonic Nanostructure .....	6
1.1.3 Engineering the Arrangement of Nanoparticle Building Blocks to Create Plasmonic Nanostructures .....	13
1.2 Overview.....	20
1.3 References.....	22
Chapter 2 Synthesis of 2D Quasicrystal Spherical Nanoparticle Arrays.....	28
2.1 Background and Motivation.....	28
2.2 Periodic Cylindrical Nanoparticle Arrays .....	31
2.3 Simulation Methods .....	34
2.4 Cylindrical Ammann-Beenker Au Nanoparticle Arrays.....	38
2.5 Nanofabrication of Spherical Nanoparticle Arrays by Au Enhanced Oxidation .....	40
2.6 Periodic Spherical Au Nanoparticle Array.....	45
2.7 Ammann-Beenker Spherical Au Nanoparticle Array .....	49
2.8 Penrose Spherical Au Nanoparticle Array .....	55
2.9 Summary .....	62
2.10 References.....	63
Chapter 3 Self-Organized Freestanding 1D Au Nanoparticle Arrays.....	67
3.1 Background and Motivation.....	68
3.2 Rayleigh Instability .....	70
3.3 Synthesis Process.....	74
3.3.1 Smooth Nanowire Template Results.....	74
3.3.2 Surface-Modulated Nanowire Template Result .....	75
3.3.3 Variable Diameter Surface Modulated Nanowire Template Results .....	79
3.4 Optical Characterization of Freestanding 1D Nanoparticle Arrays .....	79
3.5 Transmission Electron Microscopy Characterization .....	83
3.6 Summary .....	87
3.7 References.....	87
Chapter 4 Dual-band Optical Nanoantenna with Nanoring Load.....	91

4.1 Background and Motivation.....	91
4.2 Design Optimization .....	93
4.3 Fabrication Process Optimization .....	95
4.4 Far-Field Scattering Measurement and Simulation.....	98
4.5 Electric and Magnetic Field Distribution .....	102
4.6 Charge Distribution.....	105
4.7 Summary .....	107
4.8 References.....	107
Chapter 5 Summary and Future Work .....	110
5.1 Summary .....	110
5.2 Recommendations for Future Work.....	113
5.2.1 Three-Dimensional Nanoparticle Arrays .....	113
5.2.2 Alternative Patterning and Etching Processes for Plasmonic Nanoparticle Arrays .....	116
5.2.3 Multiplexed Nanoantenna Array as Bar-Codes.....	119
5.7 References.....	120
Appendix A Periodic and Quasicrystal Nanoparticle Array Fabrication.....	122
A.1 Nanoparticle Array Fabrication and Characterization Processes.....	122
A.2 Electromagnetic Simulation Method .....	123
A.3 Optical Properties of Bulk Au and Au Thin Films .....	124
A.4 Polarization Dependent Measurements of the Periodic Array .....	125
Appendix B Self-Organized 1D Nanoparticle Arrays .....	126
B.1 Nanofabrication and Characterization Processes .....	126
B.2 Detailed Simulation Method .....	127

## LIST OF FIGURES

Figure 1-1. Collective oscillation of electrons with the incident electromagnetic field in a nanoparticle <sup>1</sup> . Copyright 2011 Nature Photonics. ....	2
Figure 1-2. (a) Scanning electron microscope (SEM) images of different types of Au nanostructures with ~10 nm gaps fabricated by using an HSQ-based lift-off process on a silicon substrate <sup>42</sup> . Copyright 2011 American Chemical Society; (b) Various nanoantennas with gap sizes down to ~10 nm, fabricated by focused ion beam milling <sup>45</sup> . Copyright 2011 Nature Photonics; (c) SEM and atomic force microscope (AFM) images of silver (Ag) nanoparticles grown by nanoimprint lithography and physical vapor deposition <sup>47</sup> . Copyright 2007 American Chemical Society. ....	7
Figure 1-3. (a) SEM of single crystal Ag sharp nanocubes <sup>55</sup> ; (b) SEM of single crystal Ag rounded nanocubes <sup>55</sup> ; (c) SEM of single crystal Ag bipyramid <sup>55</sup> . Copyright 2006 American Chemical Society; (d) SEM image of single crystal Ag nanobar <sup>57</sup> . Copyright 2007 American Chemical Society; (e) SEM (left) and TEM (right) images of hematite-Au core-shell nanoparticles with different shell thickness <sup>59</sup> . Copyright 2006 American Chemical Society. ....	10
Figure 1-4. (a) SEM image of fabricated 2D and 3D plasmonic metamaterials by layer-by-layer assembly <sup>62</sup> ; (b) Examples of plasmonic nanostructures assembled by nanomanipulation <sup>62</sup> . Copyright 2012 American Chemical Society; (c) Dynamic and structural response of Janus particles to AC electric field intensity versus frequency <sup>65</sup> . Copyright 2008 American Chemical Society; (d) SEM image of a monolayer of Ag nanorods assembled via Langmuir-Blodgett <sup>68</sup> . Copyright 2003 American Chemical Society; (e) SEM images of Au particle arrays after micro-contact printing <sup>70</sup> . Copyright 2007 Nature Nanotechnology. ....	11
Figure 1-5. (a) Two building blocks of the Penrose quasicrystal array; (b) Tiling rule for the Penrose quasicrystal array; (c) Two building blocks for the Ammann-Beenker quasicrystal array; (d) Tiling rule for the Ammann-Beenker quasicrystal array. ....	14
Figure 1-6. (a) SEM images of fabricated Periodic, Fibonacci, Thue-Morse and Rudin-Shapiro arrays with cylindrical nanoparticles; (b) Measured far-field scattering spectra of the same arrays; (c) GMT simulated extinction spectra of Periodic, Fibonacci, Thue-Morse and Rudin-Shapiro arrays with spherical nanoparticles <sup>89</sup> . Copyright 2008 American Chemical Society. ....	15
Figure 1-7. SPP propagation in straight (left column) and bent (right column) Ag nanoparticle arrays. (a) SEM images of straight (left) and bent (right) nanoparticle array taken after the BIIPP experiment; (b) Fluorescence image of straight (left) and bent (right) dye coated nanoparticle array; (c) Fluorescence image of the same array recorded after a 20 min exposure to 633 nm light focused at the left end of the straight (left) and bent (right) array; (d) Difference image created by subtracting image c from image b <sup>90</sup> . Copyright 2013 American Chemical Society. ....	17

- Figure 1-8. (a) Dark-field image of 1D Ag nanoparticle arrays on glass cover slides; (b) Experimental and simulated scattering spectra of the fabricated arrays<sup>41</sup>. Copyright 2005 American Chemical Society.....18
- Figure 2-1. (a) FESEM image of fabricated periodic cylindrical nanoparticle arrays with 135nm diameter, 90nm height, and 360nm interparticle spacing; (b) top view and (c) cross sectional view of the array; (d) Measured (red) and simulated (black, blue, pink) transmission spectra of the periodic cylindrical nanoparticle arrays. Black: corrected cylindrical shape from SEM with measured Au properties; Blue: vertical sidewall with crystalline JC Au properties; Pink: vertical sidewall with measured Au properties.....33
- Figure 2-2. (a) Quasicrystal Ammann-Beenker tiling showing the square and rhombohedral prototiles in yellow and blue; (b) The designed Ammann-Beenker quasicrystal with a prototile side length  $a$  of 392nm; (c) FESEM image of a fabricated cylindrical Ammann-Beenker quasicrystal with nanoparticles that are 160nm in diameter and 60nm tall; Inset: Enlarged view of the Ammann-Beenker array; (d) Measured (red) and simulated (black) transmission spectra of the Ammann-Beenker cylindrical nanoparticle arrays. The simulation was performed using the measured thin-film Au properties and a spherical nanoparticle geometry. ....39
- Figure 2-3. Schematic diagrams and FESEM images showing the evolution of the Au: (a) evaporated Au is in direct contact with Si at  $t=0$ min; (b) Au hemisphere is encapsulated in  $\text{SiO}_2$  and there is Si left for oxidation at  $t=5$ min;(c) Au hemisphere is in direct contact with the substrate and no more Si can be provided for the oxidation at  $t=30$ min;(d) formation of Au spherical nanoparticle to reduce the surface energy at  $t=60$ min. ....42
- Figure 2-4. (a) FESEM image of fabricated periodic arrays with spherical Au nanoparticles that are 135nm in diameter and have an interparticle spacing of 360nm; (b) top view and (c) cross sectional view of the array; (d) FESEM image of the fabricated spherical Ammann-Beenker nanoparticle arrays of 135 nm in diameter and 392 nm prototile side length; Inset: Enlarged view of the Ammann-Beenker array. ....46
- Figure 2-5. (a) Measured (red) and simulated (blue and black) transmission spectra of periodic arrays with spherical Au nanoparticles that are 135nm in diameter and interparticle spacing of 360nm; Blue: crystalline JC Au property; Black: measured Au property ; (b) Far-field scattering map of the periodic spherical arrays, which have a uniform red color. ....48
- Figure 2-6. (a) Measured (red) and simulated (blue) transmission spectra of Ammann-Beenker spherical Au nanoparticle arrays with 135nm diameter and 392nm prototile side length. The simulation was performed using the bulk JC Au properties and spherical nanoparticle shape; (b) Far-field scattering map of the Ammann-Beenker spherical Au nanoparticle arrays, which show an inhomogeneous light distribution. ....50
- Figure 2-7. (a) Fourier transform image of the Ammann-Beenker arrays (log scale); (b) The corresponding real space distances are marked in the Ammann-Beenker array,  $a$



is the prototile side length of the tiling, $d_1$ is the distance between two adjacent square prototiles, $d_2$ is the diagonal of the rhombus prototile and $d_3$ is the diagonal of the square prototile.....	52
Figure 2-8. Enlarged view of the Fourier transform image of the Ammann-Beenker arrays between the first and second circles (log scale). ....	54
Figure 2-9. (a) The quasicrystal Penrose tiling that highlights two rhombohedral prototiles in yellow and blue; (b) The designed Penrose nanoparticle arrays with prototile side length $s$ of 485nm; (c) FESEM image of the fabricated Penrose quasicrystal arrays with spherical Au nanoparticles that are 135 nm in diameter; Inset: Enlarged view of the Penrose array.....	56
Figure 2-10. (a) Measured (red) and simulated (blue) transmission spectra of Penrose quasicrystals with spherical Au nanoparticle that are 135nm in diameter and a prototile side length of 485nm; the simulation was performed using the bulk Au properties and a spherical nanoparticle shape; (b) Far-field scattering map of the fabricated Penrose arrays shows an inhomogeneous light distribution dominated by three colors.....	58
Figure 2-11. (a) The Fourier transform image of the Penrose array (log scale); (b) The corresponding real space distances are marked in the Penrose arrays, where $s$ is the prototile side length, $d_1$ is the diagonal of the narrower rhombus prototile, $d_2$ is long diagonal of the wide rhombus prototile and $d_3$ is short diagonal of the wide rhombus prototile. ....	60
Figure 3-1. (a) Schematic process for Au nanoparticle chain formed on smooth wire; (b) TEM image of the Au wire formed within the SiO <sub>2</sub> shell. Scale bar, 50nm; (c) TEM image of the Au nanoparticle chain formed within the SiO <sub>2</sub> shell after further thermal treatment. Scale bar, 50nm.....	71
Figure 3-2 (a) Schematic illustration of process for 1D Au nanoparticle array formed using wires with controlled surface undulations; (b) and (c) Evolution of Au nanoparticle array formation inside the SiO <sub>2</sub> wire. Scale bar, 200nm. ....	73
Figure 3-3. (a) Distribution of Au nanoparticle arrays with controlled interparticle spacing and diameter formed by the same thermal treatment at 800 °C for 2 hours; (b), (c), (d) and (e) corresponding FESEM images: the top image in each colored box was taken at an accelerating voltage of 5kV, and the bottom image was taken at an accelerating voltage of 20kV. All scale bars, 200nm. The symbol represents the Au coating thickness/the modulation wavelength; ★20nm/630nm; ●10nm /630nm; ▲5nm /230nm; ★20nm /430nm; ▲5nm /430nm; ●10nm /230nm; ★20nm/230nm; ◆ Tapered wires with 10nm Au coating; ✱ smooth wires with 10nm Au coating. ....	77
Figure 3-4. (a) Illustration of optical extinction measurement of freestanding 1D Au nanoparticle arrays chain ensemble in isopropanol solution; (b) Calculated (top) extinction spectrum of individual Au nanoparticle chain in IPA solution, measured (bottom) extinction spectrum of the 1D Au nanoparticle chain ensemble in IPA	

- solution; Inset: the dark field microscopy images of the individual 1D Au nanoparticle array; the green color agrees well with the plasmonic peak.....81
- Figure 3-5. (a) Electron energy loss spectrum of the individual 1D Au nanoparticle array. The surface plasmon peak is at 2.25eV. Scale bar: 500nm The inset shows the STEM image of the measured Au nanoparticle array, the red box is the region from which the spectrum image is taken, the beam is positioned at the red cross outside the particle and the yellow box is the area that was used for drift correction during experiment; (b) Energy map of the individual 1D nanoparticle array at beam energy of  $2.25\text{eV} \pm 0.25\text{eV}$  (left) and  $3.25\text{eV} \pm 0.25\text{eV}$ . Scale bar: 100nm. The maps are extracted from the spectrum image data with a window of width 0.5eV. The energy intensity around the particle is enhanced at the resonance energy. Note: The “halo” only occurs along the axial direction because the thick 100nm oxide in the radial direction prevents electrons from being collected.....84
- Figure 3-6. EFTEM images at (a)1.6eV (b) 2.2eV(c) 3.2eV of an individual Au nanoparticle chain, scale bar :200 nm; theoretical distribution of the electromagnetic field intensity  $|E|^2$  at (d)1.6eV (e) 2.2eV (f) 3.2eV of the chain with surface modulation when the light is incident along the chain; theoretical distribution of the electromagnetic field intensity  $|E|^2$  at (g)1.6eV (h) 2.2eV (i) 3.2eV of the chain with surface modulation when the light is incident perpendicular to the chain direction; the electric field is greatly enhanced around the plasmonic resonance energy both from the simulation and experiment result. Beyond or below the resonant energy, the electric field is not as strong as at the resonance energy. The arrow in the figures indicates the polarization direction. ....86
- Figure 4-1. (a) Schematic illustration of the dimer nanoantenna loaded with a nanoring; (b) The simulated scattering spectrum of the nanoring-loaded nanoantenna with different inner ring radius.....94
- Figure 4-2. (a) Process simulation results for the nanoring-loaded dimer antenna with specific dose and process blur; FESEM images of the nanoring-loaded nanoantenna written with high process blur and low dose (b), high process blur and high dose (c) and low process blur and intermediate dose (d). Scale bar: 100nm. ....96
- Figure 4-3. The schematic and FESEM images of the fabricated nanoantenna with air load (a), solid load (b), nanoring load (c). Scale bar: 100nm; Far-field scattering measurement result for the nanoantenna with air load (d), solid load (e), nanoring load (f) under unpolarized light excitation; Far-field scattering simulation result for the nanoantenna with air load (g), solid load (h), nanoring load (i) under  $0^\circ$ (Orange),  $45^\circ$ (red) and  $90^\circ$ (Blue) polarized light excitation under  $0^\circ$ (Orange),  $45^\circ$ (red) and  $90^\circ$ (Blue) polarized light excitation. ....99
- Figure 4-4. (a) The electric field and (e) magnetic field distribution of the fabricated nanoantenna with air load under parallel polarization excitation; (b) The electric field and (f) magnetic field distribution of the fabricated nanoantenna with solid load under parallel polarization excitation; (c) The electric field and (g) magnetic field distribution of the fabricated nanoantenna with nanoring load at longer wavelength peak around 850nm under parallel polarization excitation; (d) The electric field and

(h) magnetic field distribution of the fabricated nanoantenna with nanoring load at short wavelength peak around 650nm under parallel polarization excitation. ....	103
Figure 4-5. (a) The charge distribution of the fabricated nanoantenna with air load under parallel polarization excitation; (b) The charge distribution of the fabricated nanoantenna with solid load under parallel polarization excitation; (c) The charge distribution of the fabricated nanoantenna with nanoring load at longer wavelength peak around 850nm under parallel polarization excitation; (d) The charge distribution of the fabricated nanoantenna with nanoring load at short wavelength peak around 650nm under parallel polarization excitation. ....	106
Figure 5-1. Schematic illustration of the nanofabrication process: (a) patterning the array features; (b) forming the Au/ <i>a</i> -Si/SiO <sub>2</sub> / <i>a</i> -Si/Au cylindrical arrays by deposition and lift off; (c) forming the 3D spherical nanoparticle arrays by Au-enhanced oxidation; (d) Top view FESEM of fabricated 3D spherical nanoparticle arrays; (e) Cross-sectional FESEM of 3D spherical nanoparticle arrays. ....	114
Figure 5-2. (a) FESEM image of the 3D spherical nanoparticle arrays that show the two Au nanoparticles stacked in the vertical direction; (b) Measured and simulated far-field scattering spectra for the 3D arrays. ....	115
Figure 5-3. Schematic illustration of the fabrication process: (a) Deposit and lift-off Au mask; (b) MACE to form high aspect-ratio <i>a</i> -Si/ <i>a</i> -SiGe superlattice nanowires; (c) Selective etching of the <i>a</i> -SiGe segment and conformal deposition of Au on the wire surface; (d) Au enhanced oxidation to form the 3D nanoparticle arrays. Preliminary experimental demonstration: (e) Photoresist features after electron-beam patterning; (f) <i>a</i> -Si/ <i>a</i> -SiGe superlattice nanowires after etching; (g) <i>a</i> -Si/ <i>a</i> -SiGe surface modulated nanowires after selective etching of the <i>a</i> -SiGe segment; (h) 3D nanoparticle arrays after Au-enhanced oxidation. Scale bar: 100nm. ....	116
Figure 5-4. Schematic of the etching process. H <sub>2</sub> O <sub>2</sub> is reduced at the interface between metal and solution injecting holes (h) into the silicon valence band, creating a hole-rich region around the catalyst particle. The holes (h) are consumed by the oxidation of Si <sup>0</sup> to Si <sup>4+</sup> at the HF interface to form soluble H <sub>2</sub> SiF <sub>4</sub> . The metal travels into the silicon wafer as silicon around and beneath the metal is dissolved <sup>9</sup> . ....	117
Figure 5-5. Preliminary result for <i>a</i> -Si/ <i>a</i> -SiGe superlattice nanowire arrays with high aspect ratio. ....	118
Figure 5-6. Schematic illustration of the fabrication process: (a) The Au deposition using the self-assembled polystyrene beads as a mask and removing the beads after the deposition via sonication; (b) MACE etch to form a high aspect-ratio <i>a</i> -Si/ <i>a</i> -SiGe superlattice rectangle; (c) Selective etching the <i>a</i> -SiGe segment and conformally depositing Au on the rectangle surface; (d) Au enhanced oxidation to form the 3D nanoparticle arrays. ....	119
Figure A-2. The optical properties of Bulk Au and Au thin film. Johnson-Christy <i>n</i> (solid blue) and <i>k</i> (dash blue); Au thin film <i>n</i> (solid black) and <i>k</i> (dash black). ....	124

Figure A-2. Measured (red) and simulated (gray) transmission spectra of the periodic spherical nanoparticle arrays under transverse electric field (a) and transverse magnetic field (c) polarized light; Measured (red) and simulated (gray) transmission spectra of the periodic cylindrical nanoparticle arrays under transverse electric field (b) and transverse magnetic field (d) polarized light. .... 125

**LIST OF TABLES**

Table 3-1. Summary of etching conditions for the four types of surface modulated Si nanowires used to create the 1D Au nanoparticle arrays. ....	76
--	----

## ACKNOWLEDGEMENTS

First and foremost, I offer my most sincere gratitude to my dissertation advisor, Professor Theresa Mayer, for her invaluable advice and devotion during my years at The Pennsylvania State University. I thank her for recognizing me as a potential doctoral candidate when I applied for the PhD program in the summer of 2007 as well as for her continuous support in providing me with a research assistantship. I specially appreciate Professor Mayer's efforts in spending time on revising my dissertation while managing her many other responsibilities. Her ingenuity, high standard of research quality and work ethic have set a great example for me concerning scientific research and my future career in industry. My doctoral work would not be possible without her support.

I am also indebted to my dissertation committee members, Professor Joan Redwing, Professor Douglas Werner, Professor Tom Mallouk and Professor Dennis Lin, for their support in my research work. I thank them for their guidance and for providing insightful advice from their expertise, which made it possible for my work to bridge across different disciplines.

During my seven years at Penn State, I had the honor and pleasure to work with some of the brightest and kindest people that I have ever met. I want to thank the following people for their support in my doctoral work and their continuous encouragement that helped me to get through the lows of the seven years and made the high notes worth celebrating. These special people are: Dr. Tsung-ta Ho, Dr. Bangzhi Liu, Dr. Wenchong Hu, Dr. Heayoung Yoon, Dr. Aaron Vallett, Dr. Jie Li, Dr. Chito Kendrick, Dr. Yue Ke, Dr. Sean (Xiaming) Liu, Dr. Seokho Yoon, Dr. Haoting Shen, Dr. Chad Eichfeld, Dr. Alexey Kovalev, Dr. Yan Tang, Dr. Jaekyun Kim, Xiahua Zhong, Xin Wang, Lan Lin, Scott Levin, Liu Liu and Huichu Liu.

I would also like to thank the Department of Energy (DOE) and Material Research Science and Engineering Centers (MRSEC) for providing research funding and career placement opportunities. Also, I want to thank the Penn State University MRI-Nanofab, MRI-MCL and EE-

Microfab for providing first-class research facilities, training and support that have been required in my doctoral work.

Finally, I thank my family in China for their patience, encouragement and support all these years. Their love is felt from the other side of the Earth here in the United States without time zone difference.

# **Chapter 1**

## **Introduction**

The research presented in this dissertation focuses on manipulating the optical response of plasmonic resonant nanostructures by arranging noble metal nanoparticle building blocks in one- and two-dimensional (1D, 2D) periodic and quasicrystal arrays. This chapter provides a brief background of previous theoretical studies and experimental demonstrations of plasmonic nanostructures, along with a discussion of the current limitations and challenges in plasmonic devices and technologies. The chapter concludes with a summary of the key contributions this dissertation makes to the field of plasmonic nanostructures.

### **1.1 Background and Motivation**

Plasmonic resonances are the collective oscillations of electron clouds relative to fixed ions<sup>1</sup>, as illustrated in Figure 1-1. These resonances play an important role in the optical properties of metals. When this oscillation occurs at the surface of a metal nanoparticle with size comparable to or smaller than the incident excitation, the induced electric field is much larger than the incident field<sup>2</sup>, and the optical behavior is distinct from that of bulk metal<sup>2</sup>. This phenomenon opens a route to amplify, concentrate and manipulate<sup>3</sup> light at the nanoscale. This allows for the possibility of overcoming the diffraction limit of traditional optics, thereby increasing the resolution and sensitivity of optical probes<sup>4,5</sup>. These unique properties can also be exploited in a wide range of applications, including biomedical devices<sup>6,7</sup>, solar energy harvesting<sup>8-12</sup>, communication technologies<sup>13-15</sup>, and others. This has promoted active research to develop the theoretical models



needed to engineer the plasmonic building blocks and to experimentally fabricate the resonant nanostructures required to realize the desired functionality in the optical wavelength regime.

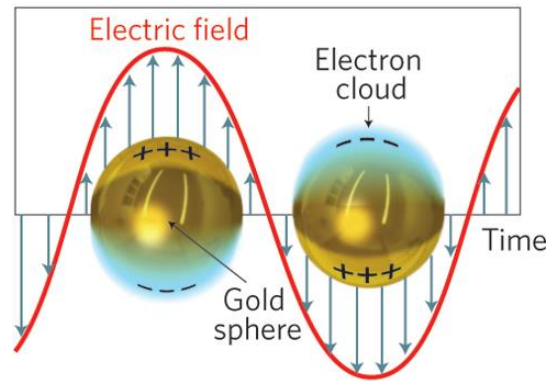


Figure 1-1. Collective oscillation of electrons with the incident electromagnetic field in a nanoparticle<sup>1</sup>. Copyright 2011 Nature Photonics.

Due to the nature of plasmonic resonance, the resonant frequency of localized surface plasmons is very sensitive to both the intrinsic properties of the building blocks<sup>16-21</sup> (shape, diameter, height, material) and the extrinsic properties of the environment<sup>22,23</sup> (dielectric environment, incident polarization). When the nanoresonators are arranged in arrays, the resonant properties of the array can also depend sensitively on the distance between the adjacent building blocks and their geometry. If the distance between two adjacent building blocks is much smaller than the incident wavelength, near-field interactions that have a distance dependence of  $d^{-3}$  dominate.<sup>2</sup> In this case, far-field scattering is suppressed by the excitation of the plasmonic mode in the nanostructure, and this leads to strong field localization<sup>24,25</sup> in the gaps between adjacent particles. In contrast, far-field diffractive coupling dominates for structures with larger particle separations. Far-field coupling has a distance dependence of  $d^{-1}$ , and it affects the plasmonic line shape caused by changes in the grating orders from evanescent to radiative<sup>26,27</sup>. This flexibility provides the possibility of building novel nanostructures with complex functionality by carefully

engineering the building block itself and/or properly arranging the building blocks in specific array configurations.

In the following subsections, prior work on the development of electromagnetic models and fabrication methods for the design and experimental realization of plasmonic devices is discussed. The limitations and challenges of these models and methods are described, and the research goals for this dissertation are defined.

### **1.1.1 Analytical Methods for Predicting the Performance of Plasmonic Nanostructures**

Accurate electromagnetic modeling of plasmonic nanostructures requires substantial computational resources. This has sparked significant interest in developing highly efficient analytical approaches that are several orders of magnitude faster than conventional finite-difference and finite-element simulation methods. The five common modeling methods include: Mie theory, Discrete Dipole Approximation (DDA), Beam Boundary Methods (BEM), Finite Element Method (FEM) and Finite Difference Time Domain (FDTD).

Mie theory was named after physicist Gustav Mie, and was first used to model the optical response of spherical nanoparticles<sup>28</sup> (or infinitely long cylinders). The approach was extended to elliptical nanoparticles by Gans<sup>29,30</sup>. In this theory, it is assumed that spherical nanoparticles with arbitrary size are embedded in a linear, isotropic and homogeneous medium. Due to the symmetry of the spherical particle geometry, the incident and scattered electric field can be expanded into vector spherical harmonics in the orthogonal field. In this case, the superposition of the scattered field from individual spheres gives the total scattered field. The undetermined scattering coefficient can be obtained by imposing appropriate boundary conditions on the tangential component of the electric and magnetic field and truncating the multipolar order. Once the scattering coefficients are determined, the extinction, absorption and scattering cross section as well as the electromagnetic

field inside and outside of nanoparticles can be calculated. The same information can also be calculated for elliptical-spheroidal particles if there is no significant change in the phase of incident field over the particle volume, which is known as the quasi-static approximation. By controlling the multipolar orders, any desired level of accuracy can be achieved. This method has been very important in the analysis of arrays with larger nanoparticles and strong higher-order multipolar interactions. However, this method is limited to spherical or spheroidal shaped nanoparticles.

In contrast to Mie theory, which is only applicable to spherical-like particles, the DDA<sup>31,32</sup> can model nanoparticles with arbitrary shape. In this approach, arbitrary shaped nanoparticles are discretized to be finite point dipole arrays. Each point dipole acquires a dipole moment in a local electric field. The scattering problem can then be expressed by simple matrix equations. Using iterative methods with a predefined error criteria, the polarizability vector can be solved. The extinction cross section can be calculated from the optical theorem based on the polarizability vector. This gives a simple, yet effective analysis method. However, the DDA method becomes time consuming when all of the multipolar scattering order corrections are considered, which are important for particles with large diameters beyond 50nm<sup>33</sup>. In addition, the results are not accurate for closely packed metal sphere clusters, particularly touching spheres. It has been shown that obtaining accurate results for gold (Au) spheres (diameter of 100 nm) in the near-IR region using the DDA method requires  $10^7$  dipoles per sphere<sup>34</sup>. This renders the method impractical for arrays due to the demanding computational load.

The BEM is a powerful numerical technique that is based on the Gauss, Green and Stokes theorems. Computation efficiency is obtained by reducing the volume differential equations to boundary integral equations<sup>35</sup>. The continuous boundary is segmented into a number of points located at the centroids of small surface elements, and the surface charge and currents are determined from the integral equations. The electromagnetic field can then be found, and the scattering, absorption and extinction cross section can be computed from the Poynting vectors<sup>36</sup>.

Compared to the DDA, the discretization for BEM is only performed on the surface, and the computational demand is low. However, the BEM process requires complex parameterization and is only applicable to structures in a homogeneous and isotropic dielectric environment<sup>37</sup>.

FDTD and FEM are numerical methods that involve discretization in both time and space. After discretizing the entire region containing nanoparticles, the differential form of Maxwell's equations are solved. These methods are simple to implement for periodic arrays with translation symmetry because they can be simplified to an individual nanoparticle problem with periodic boundary conditions. In addition, this method is not limited to particles embedded in a homogeneous and isotropic environment. However, the larger area outside of the nanoparticles must be included in the simulation to properly account for light propagation in the surrounding medium. Moreover, a perfectly matched layer boundary condition must also be applied. This greatly increases the simulation volume and computational load.

In prior simulations using GMT, DDA and BEM, the plasmonic nanostructures have been illuminated with infinite plane waves. This only provides qualitative information for the optical properties of the structure, including extinction, scattering, and absorption cross sections. Therefore, the values cannot be quantitatively compared with the experimentally measured results. Although FDTD and FEM can provide quantitative information for the optical response, including reflectance and transmittance, the computational load is great when complex nanostructures without translational symmetry are simulated.

Several modeling methods that overcome these limitations were used in this dissertation research. In Chapter 2, a modified GMT with a finite width incident beam was used to determine transmission and reflection coefficients as well as the scattering properties of 2D quasicrystal nanoparticle arrays. This approach provides a quantitative comparison between the experiment and simulation, which is essential for applications such as solar cells and absorbers. In Chapters 3 and

4, FDTD and FEM were adopted due to the simple nanostructure configuration, and thus relatively low computational load.

### **1.1.2 Fabrication Methods for Plasmonic Nanostructure**

Due to the sensitivity of the plasmonic resonance on the intrinsic properties of the building blocks, it is essential to control the size, shape and spacing of the nanostructures when they are fabricated. Top-down and bottom-up methods have been used to define plasmonic building blocks with predetermined shapes. Top-down approaches include electron-beam lithography and focused ion beam (FIB) milling, which are able to produce nearly identical building blocks with well-controlled dimensions and arrangements. Bottom-up methods typically rely on chemical synthesis and self-assembly of the nanoparticle building blocks, which are conducted from solutions.

#### ***1.1.2.1 Top-down Approaches***

The most commonly used top-down nanofabrication approach employs electron-beam lithography to pattern the array features followed by metal deposition and lift-off to create the nanoparticles<sup>38-41</sup>. Electron-beam lithography provides a spatial pattern resolution of less than 5nm, as illustrated in Figure 1-2(a)<sup>42</sup>. This method begins by applying an electron-sensitive resist on a planar substrate, and selectively exposing the desired region. The patterned resist is then developed, and a noble metal such as Au is deposited on the entire sample. Normally, a thin layer of titanium (Ti) or chromium (Cr) is added to improve the adhesion of the noble metal nanoparticles to the substrate. However, this layer also increases surface plasmon damping<sup>43,44</sup>, thereby increasing the optical loss of the plasmonic nanostructure.

Another top-down approach that is gaining in popularity uses FIB milling, which is based on the localized sputtering of material by accelerated Ga ions extracted from a liquid metal ion source. This process produces nanoscale resolution features by direct patterning of the noble metal<sup>45</sup>. The accelerated Ga ions are focused into a beam of a few nanometer and scanned over the substrate to achieve the desired patterns<sup>46</sup>, as illustrated in Figure 1-2(b). The primary advantage of the FIB

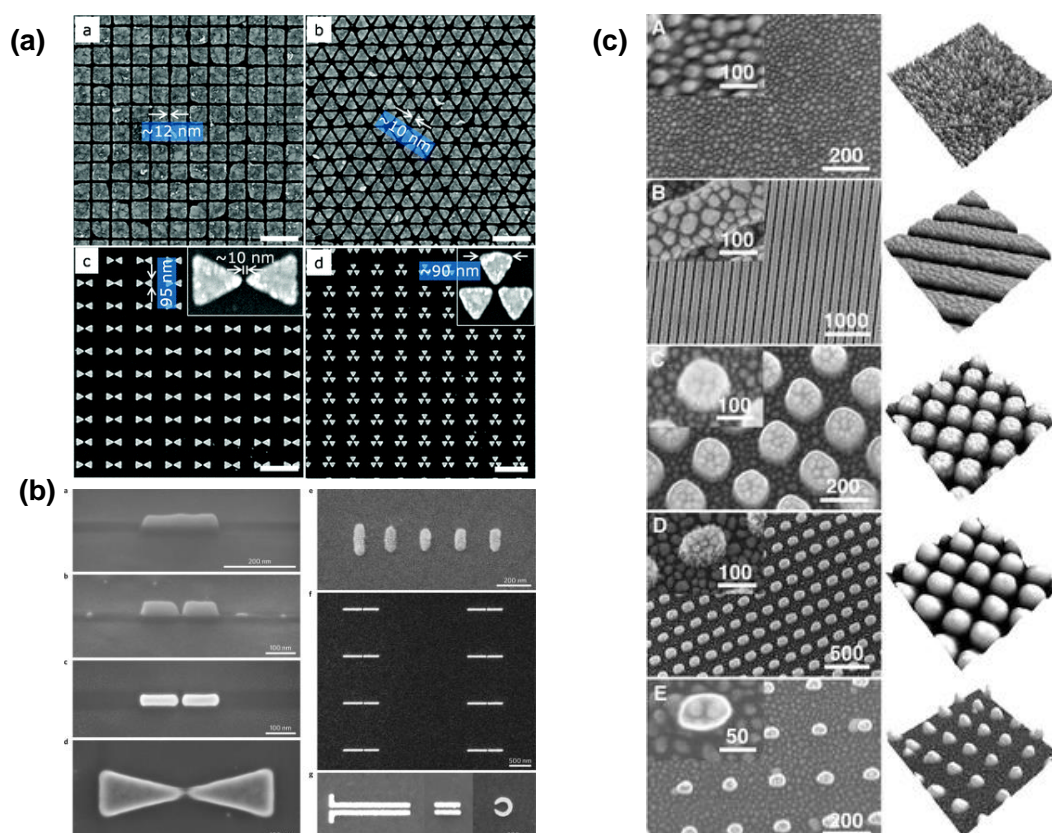


Figure 1-2. (a) Scanning electron microscope (SEM) images of different types of Au nanostructures with ~10 nm gaps fabricated by using an HSQ-based lift-off process on a silicon substrate<sup>42</sup>. Copyright 2011 American Chemical Society; (b) Various nanoantennas with gap sizes down to ~10 nm, fabricated by focused ion beam milling<sup>45</sup>. Copyright 2011 Nature Photonics; (c) SEM and atomic force microscope (AFM) images of silver (Ag) nanoparticles grown by nanoimprint lithography and physical vapor deposition<sup>47</sup>. Copyright 2007 American Chemical Society.

technique is its high resolution, which can reach down to 10 to 20nm feature sizes<sup>44</sup> with high reproducibility. However, the surface is often contaminated due to re-deposition of the sputtered material during ion beam milling. In addition, the FIB-defined patterns typically have a tapered

sidewall profile, which leads to non-uniformity in the pattern dimensions. Finally, the high energy Ga ions<sup>44</sup> can also be implanted into the metal film and the substrate, which can influence the dielectric properties of the materials.

Direct write electron-beam and FIB patterning processes are not well suited for high throughput patterning of nanoscale features over large substrate areas. Nanoimprint lithography is an alternative top-down approach, which has the potential to overcome this limitation<sup>47-49</sup>. Examples of nanoimprinted structures are shown in Figure 1-2(c)<sup>47</sup>. Nanoimprint techniques have used thermoplastic and photo-curable imprint resists. In both approaches, a hard mold with predefined surface topological features is pressed against a substrate coated with an imprint resist under a well-controlled pressure and temperature. The pattern is transferred onto the substrate when the mold is removed. The differences between these two processes are related to the mold material and the resist. In thermoplastic imprint, the resists are thermoplastic polymers that undergo a glass transition at low temperature. In contrast, photo-nanoimprint resists are ultraviolet (UV) curable, and the mold is made of UV transparent fused silica. Both processes can achieve resolution down to the limit of the fabricated template, which is in the range of 10nm. However, surface contamination and defects are difficult to avoid due to the direct contact between the mold and the imprint resist.

### ***1.1.2.1 Bottom-up Approaches***

Polycrystalline evaporated or sputtered noble metal films give increased ohmic damping (electron-electron scattering, electron-phonon scattering, etc.) compared to ideal crystalline metals. The metal surface roughness of top-down fabricated structures also further increases the damping rate<sup>50</sup>. Bottom-up synthesis provides an alternative route to produce high-quality, single-crystal metal nanostructures with nearly atomically smooth surfaces. Chemical routes<sup>51-53</sup> can create

plasmonic building blocks with different shapes such as spheres, rods<sup>54</sup>, cubes<sup>55</sup> (Figure 1-3 a-b), tetrahedra<sup>56</sup>, nanobars and nanorice<sup>57</sup> (Figure 1-3 d) from a variety of materials, including core-shell particles<sup>58-60</sup> (Figure 1-3 e). However, the building blocks must be arranged in specific configurations to realize designed optical functionalities. The arrangements can be achieved by self-assembly methods, including layer-by-layer process<sup>61</sup>, nano-manipulation<sup>62,63</sup>, dielectrophoresis<sup>64-67</sup>, Langmuir-Blodgett techniques<sup>68,69</sup> and micro-contact printing<sup>70</sup>.

The layer-by-layer deposition process creates alternating layers of densely packed nanoparticles in a series of self-assembly processes. Starting with a seed layer, a self-passivated layer of nanoparticles is formed over an initial seed layer by immersing the substrate in a solution containing the complementary functionalized nanoparticles. Linker molecules are added to the first layer of nanoparticles before the substrate is immersed in a solution containing the second type of building block. The nanoparticles selectively bind to the linker molecules to form the second layer. As illustrated in Figure 1-4(a), the sequential process is repeated until the desired thickness is obtained. This process is suitable for low-cost, large-area device fabrication. However, the nanoparticle materials and geometries can only be varied in the axial deposition direction. In addition, controlled spacing between particles in a single layer is not possible.

Individual nanoparticles have been manipulated on a particle-by-particle basis using the tip of atomic force microscope (AFM) or a manipulator in a field emission scanning electron microscope (FESEM), as shown in Figure 1-4(b). In this approach, the building blocks of interest are first deposited on the substrate randomly, and then the substrate is loaded into an AFM or a FESEM in imaging mode. The tip or manipulator is parked “behind” the building blocks and piezo-driven stage is moved in the desired direction. In this way, the gap between particles can be reduced until they contact one another<sup>71</sup>. This method has enabled the construction of nanostructures that have been used to understand complex plasmonic coupling effects. However, it is impractical for large-scale fabrication.



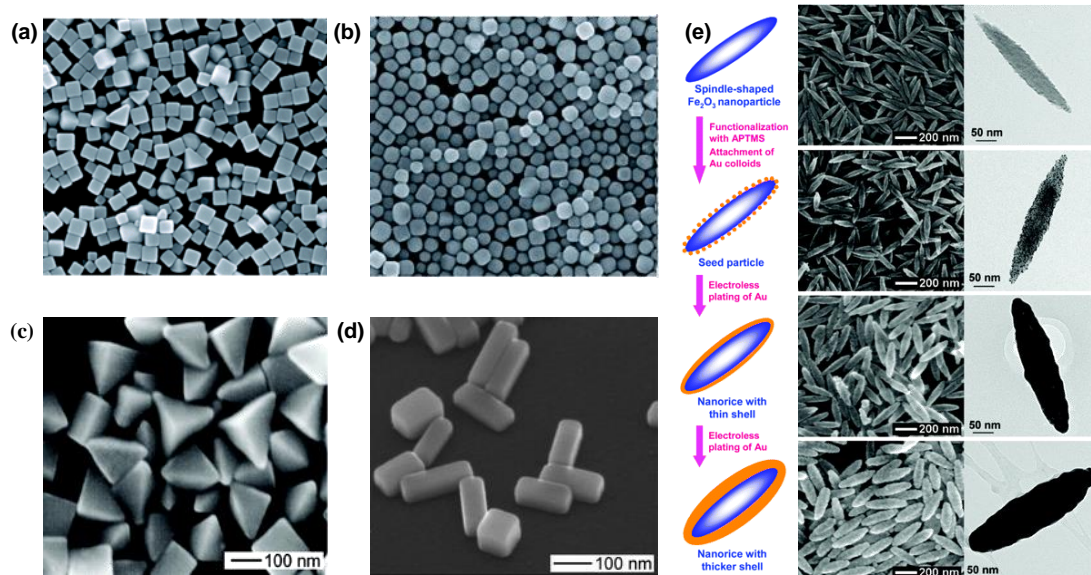


Figure 1-3. (a) SEM of single crystal Ag sharp nanocubes<sup>55</sup>; (b) SEM of single crystal Ag rounded nanocubes<sup>55</sup>; (c) SEM of single crystal Ag bipyramid<sup>55</sup>. Copyright 2006 American Chemical Society; (d) SEM image of single crystal Ag nanobar<sup>57</sup>. Copyright 2007 American Chemical Society; (e) SEM (left) and TEM (right) images of hematite-Au core-shell nanoparticles with different shell thickness<sup>59</sup>. Copyright 2006 American Chemical Society.

Dielectrophoresis can be used to manipulate polarizable, solution-suspended nanoparticles in a non-uniform electric field. Figure 1-4(c) shows that an array of nanoparticle building blocks can be assembled within the gap between electrodes energized by an alternating (AC) voltage. This method allows the manipulation and assembly of particles without the interference of electroosmotic and electrochemical effects present in direct current (DC) systems<sup>64</sup>. However, the yield for this process is still a concern for large-scale applications.

Langmuir-Blodgett techniques, which were initially developed to assemble molecular monolayers, have been extended to plasmonic building blocks. In this case, a small volume of nanoparticles suspended in an organic solution is dispersed at a water-air interface, forming a sparse monolayer of particles on the water surface. The sparse monolayer is then compressed by sliding a barrier across the surface to create a compact monolayer<sup>72</sup>. The monolayer is transferred to a

substrate by lifting it through the interface, as illustrated in Figure 1-4(d). This method has been extended to form different packing configurations with nanoparticles of different sized and shapes<sup>73</sup>. However, the process is restricted to the fabrication of compact arrays, and thus is not suitable for the sparse arrays with well-defined order. Additionally, defects are difficult to avoid.

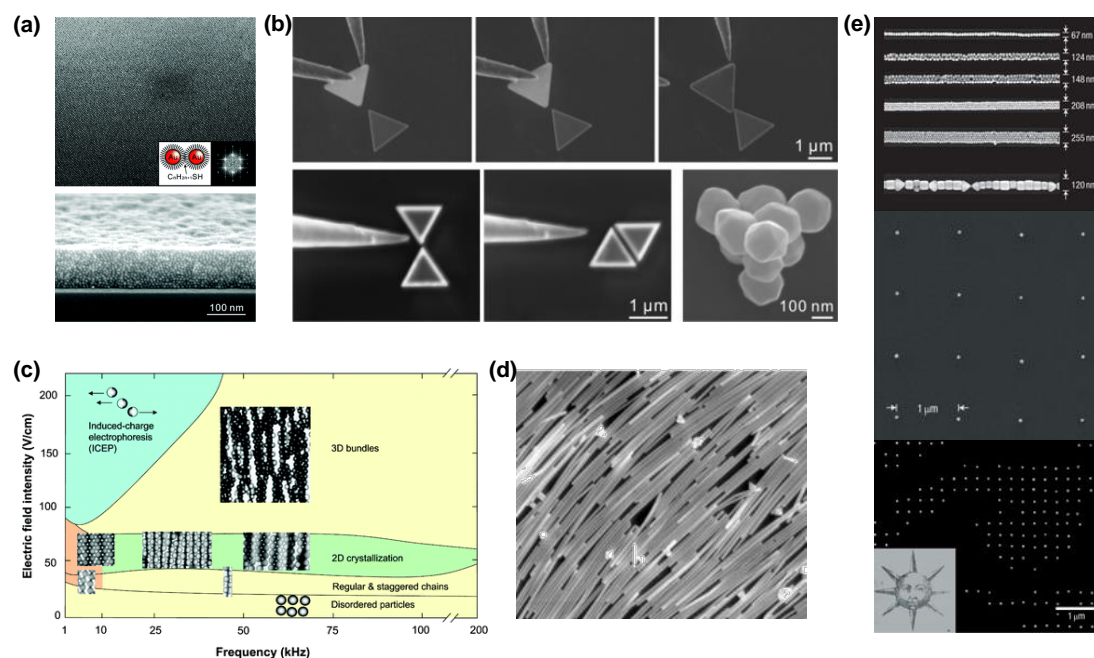


Figure 1-4. (a) SEM image of fabricated 2D and 3D plasmonic metamaterials by layer-by-layer assembly<sup>62</sup>; (b) Examples of plasmonic nanostructures assembled by nano-manipulation<sup>62</sup> Copyright 2012 American Chemical Society; (c) Dynamic and structural response of Janus particles to AC electric field intensity versus frequency<sup>65</sup> Copyright 2008 American Chemical Society; (d) SEM image of a monolayer of Ag nanorods assembled via Langmuir-Blodgett<sup>68</sup> Copyright 2003 American Chemical Society; (e) SEM images of Au particle arrays after micro-contact printing<sup>70</sup>. Copyright 2007 Nature Nanotechnology.

Micro-contact printing is a technique that was developed to position sparse arrays of nanoparticles on substrates. This process was scaled down from gravure printing to handle particles that are less than 100nm in diameter. The printing plates are first fabricated using self-assembly processes to control the arrangement of building blocks. The entire assembly is then printed onto a

different substrate by bringing the plate and substrate into proximity contact. As shown in Figure 1-4(e), the particle positions are retained during the printing process. This printing process has a resolution three orders of magnitude higher than that of the conventional printing<sup>70</sup>. However, contamination and defects must be controlled for repeatable production.

### ***1.1.2.3 Other Approaches***

Nanosphere lithography<sup>74-76</sup> combines top-down and bottom-up approaches. It provides a route to realize low-cost, large-scale and high-throughput lithography. This method uses self-assembled monolayers of nanospheres as a template, and metal evaporation and lift-off to form metal patterns at the interstices of the assembled spheres. This process is very efficient at forming sharp-edged metallic nanostructures. However, the structures created by this process are limited to close-packed arrangements that have relatively high defect densities.

Several different thermal and laser heating processes have been developed to improve the optical properties of vapor deposited noble metals by crystallizing the films. For example, localized laser heating of planar<sup>77,78</sup> and nanosphere patterned Au<sup>79</sup> has been used to create plasmonic arrays. The minimum spacing between adjacent particles has been limited to the micron scale, which prevents the use of these structures in arrays with strong inter-particle coupling. In the case of thermal annealing of deposited metal films<sup>80</sup>, the particle placement is not well controlled and their size distribution is large.

Limitations in conventional top-down and bottom-up methods necessitate the development of alternate fabrication strategies. In Chapter 2, by combining the merits of top-down patterning with thermal heating, a process was developed to create uniform spherical Au nanoparticle arrays with controlled placement, diameter, and spacing down to the nanometer scale. In Chapter 3, a method was developed to synthesize self-organized 1D Au nanoparticle arrays encapsulated within

freestanding SiO<sub>2</sub> nanowires. The process provides independent and precise control of the nanoparticle diameter and spacing without the use of direct-write electron-beam lithographic patterning.

### **1.1.3 Engineering the Arrangement of Nanoparticle Building Blocks to Create Plasmonic Nanostructures**

As discussed in the previous sections, plasmonic building blocks can be arranged into a variety of configurations to achieve specific functions, including biomedical devices, solar energy harvesting devices, and communication technology devices. The nanoparticle building blocks can be of the same or different shapes and dimensions. In this thesis, planar 2D plasmonic quasicrystals and freestanding 1D periodic arrays were fabricated by organizing the same type of spherical Au nanoparticle building blocks on a substrate or within a nanowire. In addition, a dual-band nanoantenna was realized by integrating nanoring and nanoparticle building blocks on a planar substrate. The following subsections provide a brief overview of the 2D quasicrystal arrays, 1D nanowire arrays, and nanoantennas developed in this dissertation.

#### ***1.1.3.1 Quasicrystal Au Nanoparticle Plasmonic Arrays***

Quasicrystals are a special class of structures that possess long-range order without translational symmetry. They were first discovered by Shechtman<sup>81</sup> in the diffraction pattern of solidified aluminum (Al) alloys, which display a discrete spectrum and five-fold rotational symmetry. Quasicrystals are formed by proper tiling of two or more building blocks, which together fill an entire space. Figure 1-5 illustrates Penrose and Ammann-Beenker quasicrystal tilings. The two basic building blocks for the Penrose arrays are narrow (vertex angles  $\pi/5$  and  $4\pi/5$ ) and wide (vertex angles  $2\pi/5$  and  $3\pi/5$ ) rhombi with equal sides. For Ammann-Beenker arrays, a square and

a rhombus with vertex angles of  $\pi/4$  and  $3\pi/4$  and equal length sides are the two basic building blocks. Plasmonic quasicrystal arrays are created by positioning noble metal nanoparticles at the vertices of the arrays.

Due to the diversity of the potential building blocks and substitution rules, quasicrystals provide greater flexibility in engineering the plasmonic optical response than conventional periodic crystals. Therefore, plasmonic quasicrystals are promising for use in a wide range of applications, including ultra-wideband antenna arrays<sup>82,83</sup>, optical bandgap materials<sup>84,85</sup>, broadband plasmonic enhancement devices<sup>8,9,86,87</sup>, and surface-enhanced Raman surfaces<sup>88</sup>. For example, Bauer *et al.*<sup>9</sup> used the Fano model to predict the transmittance through quasicrystals, and found that the enhancement factor for absorbed light was less dependent on the azimuthal and polar angle than for periodic structures. This results in a more uniform spectral absorption, which is important for many types of optoelectronic and solar devices. As shown in Figure 1-6(a), Negro *et al.*<sup>89</sup> fabricated

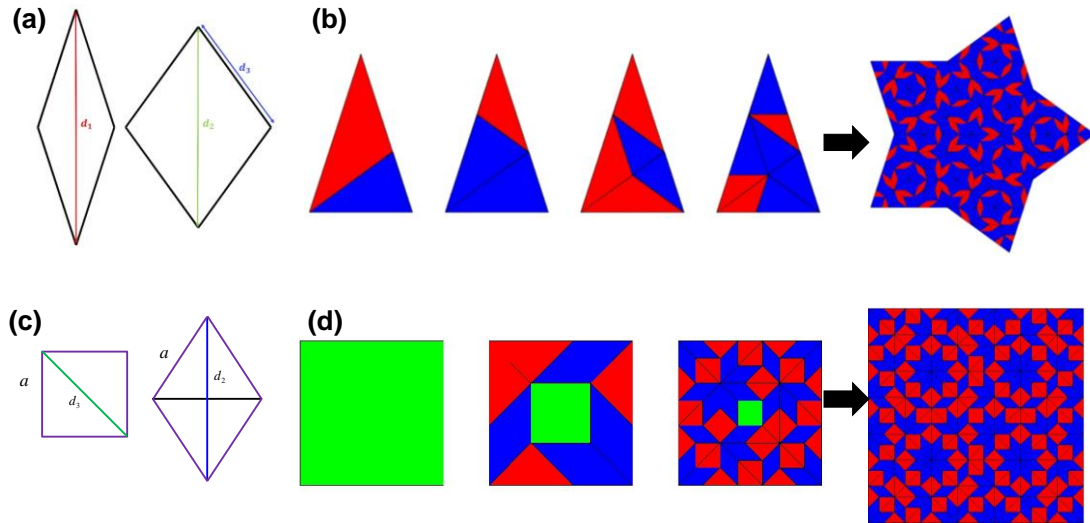


Figure 1-5. (a) Two building blocks of the Penrose quasicrystal array; (b) Tiling rule for the Penrose quasicrystal array; (c) Two building blocks for the Ammann-Beenker quasicrystal array; (d) Tiling rule for the Ammann-Beenker quasicrystal array.

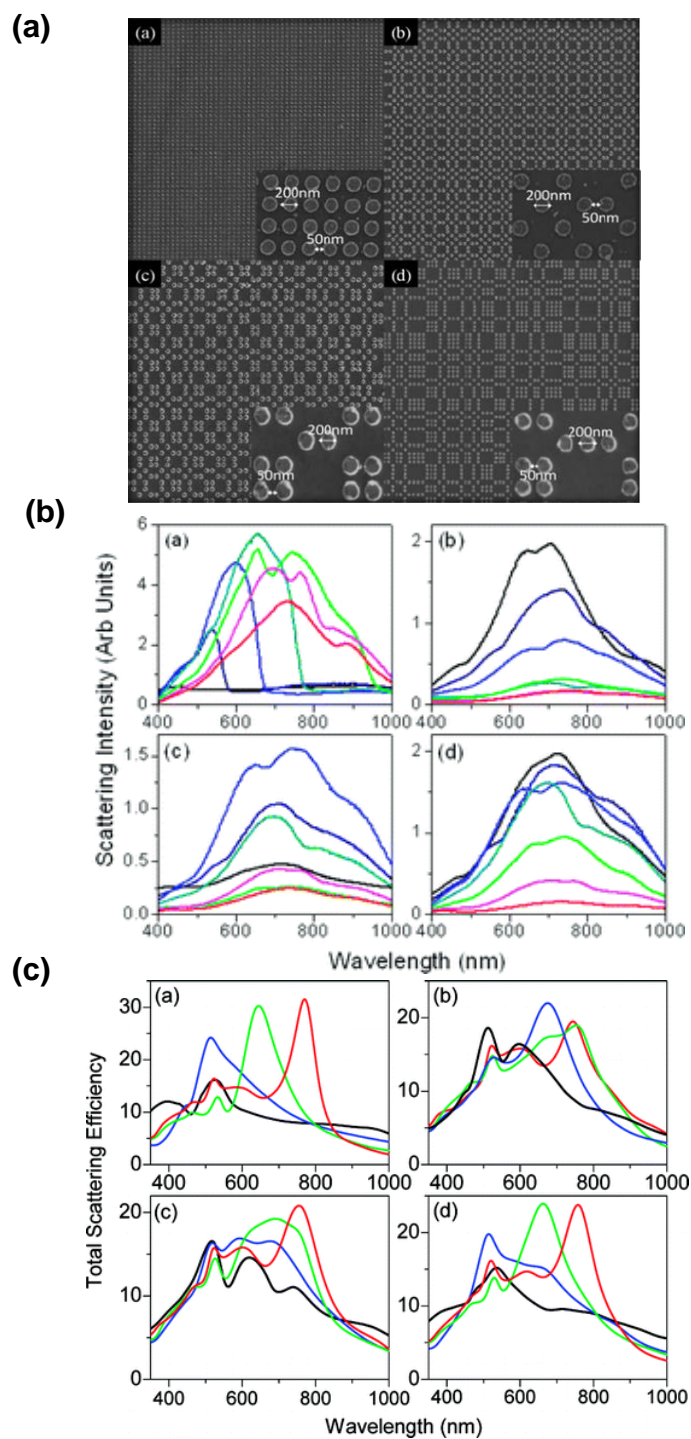


Figure 1-6. (a) SEM images of fabricated Periodic, Fibonacci, Thue-Morse and Rudin-Shapiro arrays with cylindrical nanoparticles; (b) Measured far-field scattering spectra of the same arrays; (c) GMT simulated extinction spectra of Periodic, Fibonacci, Thue-Morse and Rudin-Shapiro arrays with spherical nanoparticles<sup>89</sup>. Copyright 2008 American Chemical Society.

Fibonacci, Thur-Morse and Rudin-Shapiro quasicrystals and characterized their optical scattering properties. These structures demonstrated high scattering over a broad range of wavelengths. However, the extinction spectra predicted by numerical simulation of spherical nanoparticle arrays differed from the experimentally measured spectra from fabricated cylindrical nanoparticle arrays.

In Chapter 2, the gap between experiment and theory was bridged by producing spherical nanoparticle arrays, and studying their optical properties. Cylindrical arrays were first fabricated to explore the origin of the discrepancy between simulation and experiment. Then a new Au-enhanced oxidation approach was developed to fabricate uniformly sized spherical nanoparticle arrays with control over the size and location of the particles. The plasmonic response of the periodic and the quasicrystal spherical arrays demonstrated excellent agreement between the optical measurements and the modified GMT simulations<sup>86</sup>.

### ***1.1.3.2 Freestanding 1D Nanoparticle Chain***

Prior work has shown that 1D arrays of plasmonic nanoparticles have several unique properties. When particles are arranged with small inter-particle spacing within the near-field coupling regime, electromagnetic energy can be guided below the diffraction limit and through a 90° corner without significant loss, which makes them of interest as waveguides<sup>90-93</sup>. Specifically, Marier *et al.*<sup>93</sup> experimentally showed that electromagnetic energy can be transported from a localized sub-wavelength source to a localized detector over a distance of 0.5  $\mu\text{m}$  in a plasmonic waveguide consisting of closely spaced silver (Ag) nanorods. The propagation of plasmonic polaritons around 90° corners in Ag nanoparticle arrays without significant bending loss was also demonstrated by Solis *et al.*<sup>90</sup>. They found that the plasmonic propagation length for straight and bent Ag nanoparticle arrays was around 8.0  $\mu\text{m}$  and 7.8  $\mu\text{m}$  at the resonant excitation wavelength of 633 nm (Figure 1-7).



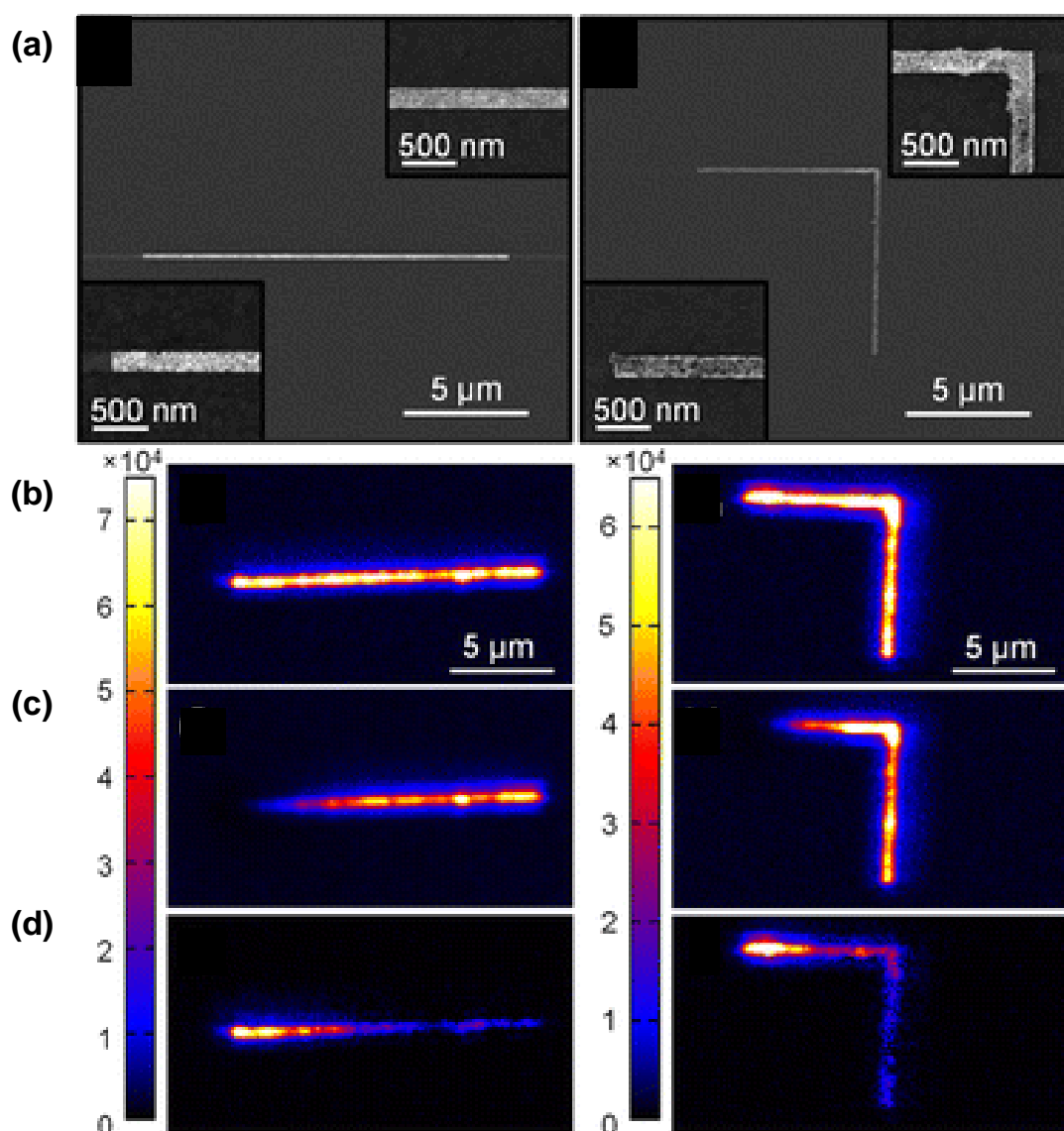


Figure 1-7. SPP propagation in straight (left column) and bent (right column) Ag nanoparticle arrays. (a) SEM images of straight (left) and bent (right) nanoparticle array taken after the BIIPP experiment; (b) Fluorescence image of straight (left) and bent (right) dye coated nanoparticle array; (c) Fluorescence image of the same array recorded after a 20 min exposure to 633 nm light focused at the left end of the straight (left) and bent (right) array; (d) Difference image created by subtracting image c from image b<sup>90</sup>. Copyright 2013 American Chemical Society.

When 1D plasmonic nanoparticle arrays are configured with large interparticle spacing, sharp plasmonic peaks can be achieved through far-field diffractive coupling between the nanoparticles, which offers high sensitivity for sensor applications. Zou *et al.*<sup>94</sup> theoretically



demonstrated that spherical 1D Ag nanoparticle arrays can produce remarkably narrow ( $\sim$  meV or less) plasmon resonance spectra upon irradiation with light polarized perpendicular to the array axis. This sharp peak occurs at a wavelength that is nearly twice that of the nanoparticle spacing. Later Hick *et al.*<sup>95</sup> experimentally demonstrated the sharp plasmon lineshape using electron-beam patterned Ag nanoparticle arrays with varying inter-particle spacing from 350 nm to 800 nm. They clearly found that the extra peak in the Rayleigh scattering spectra followed the theoretical predictions. However, the predicted line-shape of this peak was not achieved (Figure 1-8). They pointed out that defects, lattice imperfections, incoherent light source and local variations in the index of refraction were possible reasons that contributed to the broadening observed experimentally.

To accurately control the geometry of the 1D nanoparticle arrays and to minimize the effect of variation of local refraction index, a method based on Au-enhanced oxidation of Si nanowires with predefined surface features was developed in Chapter 3.

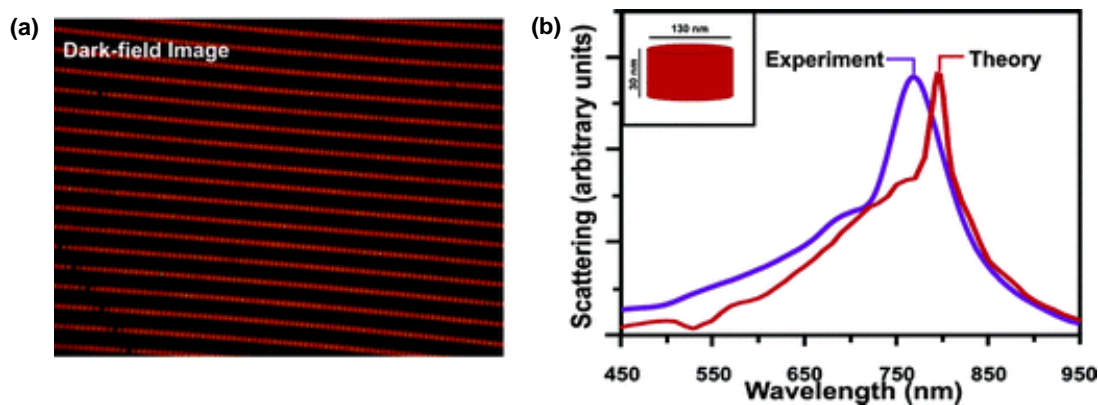


Figure 1-8. (a) Dark-field image of 1D Ag nanoparticle arrays on glass cover slides; (b) Experimental and simulated scattering spectra of the fabricated arrays<sup>41</sup>. Copyright 2005 American Chemical Society.

### ***1.1.3.3 Plasmonic Nanoantenna***

Optical nanoantennas are being developed to provide communication between nano- and micro-scale devices and to convert light to electric power. Similar to a radio frequency (RF) antennas, which convert electromagnetic waves at RF frequency into direct current electricity<sup>96</sup>, nanoantennas absorb light of specific wavelengths that are comparable to the dimension of the structure. Nanoantenna arrays with optimized geometries can efficiently absorb light with wavelengths from 0.4 to 1.6  $\mu\text{m}$ , which comprises 85% of the solar radiation spectrum<sup>97</sup>. This makes nanoantennas not only an indispensable asset to scientific research, but also a potential technological innovation in solar energy conversion.

Optical nanoantennas, which operate at visible to near-infrared wavelengths, have gained attention recently because information can be encoded at higher frequencies and at high device densities. This development has paved the way for realizing integrated optical nanocircuits<sup>13</sup>, all-optical wireless communication<sup>15</sup> and data storage devices. Similar to their RF counterparts, the capability of flexibly modifying the response of nanoantennas in the optical frequency domain is crucial for their application in both the receiving and transmitting modes. The optical nanoantenna is typically realized by using plasmonic structures, including individual nanorods/nanospheres<sup>98,99</sup>, coupled nanoparticle/nanorod dimers<sup>100,101</sup>, bow-tie nanoantennas<sup>38,102</sup> and Yagi-Uda nanoantennas<sup>103,104</sup>. The localized surface plasmon resonance of these plasmonic structures enables strong near-field and far-field diffractive coupling, which has led to many promising applications, including biological sensors<sup>6,98</sup>, photovoltaic enhancement<sup>10,11</sup>, metamaterials<sup>105,106</sup>.

Efforts have been made to develop new theoretical models for optical nanoantennas, and to experimentally validate these models. From the perspective of the theoretical studies, lumped circuit analysis methods<sup>107,108</sup> have provided a simple and useful methodology to better design and optimize nanoantennas by varying the input impedance loading. Coupled oscillator models<sup>109</sup> have

provided insight into the physical mechanisms responsible for the response by describing the plasmonic resonance with a simple mass-spring model. The Fabry-Perot model<sup>110,111</sup> connects optical nanoantennas to their RF counterparts by considering the eigenmodes of the plasmonic structures.

From the perspective of experimental studies, optical nanoantennas have been demonstrated from various nanoparticle building blocks<sup>20,112</sup> and by loading the antenna with lumped circuit elements<sup>113,114</sup>, including capacitance, inductance and resistance. However, previous work only investigated arranging building blocks of the same shape with either the same or different dimensions. This limits the range of nanoantenna responses that can be realized, and prevents the design of multiband nanoantennas. In Chapter 4, a dual-band nanoantenna is experimentally demonstrated by properly arranging nanoring and nanoparticle building blocks.

## 1.2 Overview

This dissertation introduces a novel approach to create a variety of plasmonic structures with tailored optical responses in the visible wavelength regime. This section provides an overview of the concepts covered in each of the chapters along with a brief summary.

In Chapter 2, Ammann-Beenker and Penrose quasicrystal nanoparticle arrays are investigated to achieve a broadband and a multispectral optical response in the visible regime of the spectrum. To quantitatively compare simulation and experiment, the structures were modeled using a modified GMT approach with an aperture to confine the width of the light beam. The optimized Ammann-Beenker array design was fabricated using a conventional electron-beam patterning and metal liftoff method to accurately control the diameter and spacing of the nanoparticles in the array. Discrepancies between the experimentally measured and simulated

transmission response were observed, and were attributed to the approximation of the cylindrical nanoparticles with spheres.

A new nanofabrication method based on the oxidation of Au and *a*-Si stacks was developed to transform cylindrical Au particles into spherical Au nanoparticles encapsulated in a SiO<sub>2</sub> shell. The isotropic spherical particle shape was confirmed by FESEM. Periodic arrays and quasicrystals were fabricated using this process, and excellent agreement was obtained between experiment and theory in all cases. The origin of the broadband behavior of the Ammann-Beenker arrays and multiband response of the Penrose arrays was correlated to the spacing in the lattice using Fourier transform methods. This provides guidance for future design optimization of quasicrystal plasmonic arrays beyond Ammann-Beenker and Penrose tilings.

Chapter 3 presents the design, fabrication, and characterization of self-organized free-standing 1D arrays of Au nanoparticles. The structures were fabricated by Au-enhanced oxidation of Au-coated Si nanowires with a predefined surface modulation. This surface structure causes the Au nanowire to fragment into an array of Au nanoparticles with well-controlled size and interparticle spacing. The optical properties of the freestanding nanoparticle arrays were characterized by optical absorption measurements of randomly oriented ensembles and by electron energy loss spectrum (EELS) measurements of individual nanoparticle arrays. The plasmonic distribution was characterized by scanning transmission electron microscopy (STEM) and energy filtered transmission electron microscopy (EFTEM) at the resonance energy and at energies far from resonance.

In Chapter 4, a plasmonic nanostructure that consisted of a nanoring and two solid Au nanoparticles is optimized to realize a dual-band nanoantenna in the visible wavelength regime. This structure was patterned by electron-beam lithography on a glass substrate and characterized by far-field scattering measurements. It was found that the measured spectra accurately matched the simulated spectra. The physical origin of multiband properties was investigated by

electromagnetic simulations to determine the electric field, magnetic field and charge distributions on the structure when it is illuminated with parallel and perpendicularly polarized light.

Chapter 5 summarizes the research presented in this dissertation by outlining the accomplishments and contributions in each chapter, and proposes directions of future research based on the results that were obtained.

### 1.3 References

- 1 Juan, M. L., Righini, M. & Quidant, R. Plasmon nano-optical tweezers. *Nat Photonics* **5**, 349-356 (2011).
- 2 Maier, S. A. *Plasmonics : fundamentals and applications*. (Springer, 2007).
- 3 Schuller, J. A. *et al.* Plasmonics for extreme light concentration and manipulation. *Nat Mater* **9**, 193-204 (2010).
- 4 Betzig, E. & Trautman, J. K. Near-Field Optics: Microscopy, Spectroscopy, and Surface Modification Beyond the Diffraction Limit. *Science* **257**, 189-195 (1992).
- 5 Nie, S. & Emory, S. R. Probing single molecules and single nanoparticles by surface-enhanced Raman scattering. *Science* **275**, 1102-1106 (1997).
- 6 Haes, A. J. & Van Duyne, R. P. A nanoscale optical biosensor: sensitivity and selectivity of an approach based on the localized surface plasmon resonance spectroscopy of triangular silver nanoparticles. *J Am Chem Soc* **124**, 10596-10604 (2002).
- 7 Kabashin, A. *et al.* Plasmonic nanorod metamaterials for biosensing. *Nat Mater* **8**, 867-871 (2009).
- 8 Pala, R. A., White, J., Barnard, E., Liu, J. & Brongersma, M. L. Design of Plasmonic Thin-Film Solar Cells with Broadband Absorption Enhancements. *Adv Mater* **21**, 3504-+ (2009).
- 9 Bauer, C. & Giessen, H. Light harvesting enhancement in solar cells with quasicrystalline plasmonic structures. *Opt Express* **21**, A363-A371 (2013).
- 10 Pala, R. A., White, J., Barnard, E., Liu, J. & Brongersma, M. L. Design of Plasmonic Thin - Film Solar Cells with Broadband Absorption Enhancements. *Adv Mater* **21**, 3504-3509 (2009).
- 11 Chen, P. Y. & Alu, A. Nanoantenna-Enhanced Optical Heterodyning and Photoemission Devices. *Ieee Antennas Prop*, 144-145 (2013).
- 12 Atwater, H. A. & Polman, A. Plasmonics for improved photovoltaic devices. *Nat Mater* **9**, 205-213 (2010).
- 13 Adato, R., Yanik, A. A. & Altug, H. On Chip Plasmonic Monopole Nano-Antennas and Circuits. *Nano Lett* **11**, 5219-5226 (2011).
- 14 Zhao, Y. & Alu, A. Optical Nanoantennas and Their Applications. *Ieee Radio Wireless*, 58-60 (2013).
- 15 Alu, A. & Engheta, N. Wireless at the Nanoscale: Optical Interconnects using Matched Nanoantennas. *Phys Rev Lett* **104** (2010).

- 16 Wang, E. C., Mokkapati, S., Soderstrom, T., Varlamov, S. & Catchpole, K. R. Effect of Nanoparticle Size Distribution on the Performance of Plasmonic Thin-Film Solar Cells: Monodisperse Versus Multidisperse Arrays. *Ieee J Photovolt* **3**, 267-270 (2013).
- 17 Kravets, V. G., Schedin, F. & Grigorenko, A. N. Extremely narrow plasmon resonances based on diffraction coupling of localized plasmons in arrays of metallic nanoparticles. *Phys Rev Lett* **101** (2008).
- 18 Henson, J., DiMaria, J. & Paiella, R. Influence of nanoparticle height on plasmonic resonance wavelength and electromagnetic field enhancement in two-dimensional arrays. *Journal of Applied Physics* **106**, 093111 (2009).
- 19 Zou, S. & Schatz, G. C. Narrow plasmonic/photonic extinction and scattering line shapes for one and two dimensional silver nanoparticle arrays. *The Journal of Chemical Physics* **121**, 12606-12612 (2004).
- 20 Nikitin, A. G., Kabashin, A. V. & Dallaporta, H. Plasmonic resonances in diffractive arrays of gold nanoantennas: near and far field effects. *Opt Express* **20**, 27941-27952 (2012).
- 21 Link, S. & El-Sayed, M. A. Shape and size dependence of radiative, non-radiative and photothermal properties of gold nanocrystals. *Int Rev Phys Chem* **19**, 409-453 (2000).
- 22 Nikitin, A. G., Nguyen, T. & Dallaporta, H. Narrow plasmon resonances in diffractive arrays of gold nanoparticles in asymmetric environment: Experimental studies. *Appl Phys Lett* **102** (2013).
- 23 Zhou, W. & Odom, T. W. Tunable subradiant lattice plasmons by out-of-plane dipolar interactions. *Nat Nanotechnol* **6**, 423-427 (2011).
- 24 Kawata, S., Inouye, Y. & Verma, P. Plasmonics for near-field nano-imaging and superlensing. *Nat Photonics* **3**, 388-394 (2009).
- 25 Fan, J. A. *et al.* Self-assembled plasmonic nanoparticle clusters. *Science* **328**, 1135-1138 (2010).
- 26 Lamprecht, B. *et al.* Metal nanoparticle gratings: Influence of dipolar particle interaction on the plasmon resonance. *Phys Rev Lett* **84**, 4721-4724 (2000).
- 27 Meier, M., Wokaun, A. & Liao, P. F. Enhanced Fields on Rough Surfaces - Dipolar Interactions among Particles of Sizes Exceeding the Rayleigh Limit. *J Opt Soc Am B* **2**, 931-949 (1985).
- 28 Mie, G. Beiträge zur Optik trüber Medien, speziell kolloidaler Metallösungen. *Annalen der Physik* **330**, 377-445 (1908).
- 29 Hulst, H. C. v. d. *Light scattering by small particles*. (Dover Publications, 1981).
- 30 Bohren, C. F. & Huffman, D. R. *Absorption and scattering of light by small particles*. (Wiley, 1983).
- 31 Draine, B. T. & Flatau, P. J. Discrete-Dipole Approximation For Scattering Calculations. *J. Opt. Soc. Am. A* **11**, 1491-1499 (1994).
- 32 Draine, B. T. The Discrete-Dipole Approximation and Its Application to Interstellar Graphite Grains. *Astrophys J* **333**, 848-872 (1988).
- 33 Yurkin, M. A. & Hoekstra, A. G. The discrete dipole approximation: An overview and recent developments. *J Quant Spectrosc Ra* **106**, 558-589 (2007).
- 34 Yurkin, M. A., de Kanter, D. & Hoekstra, A. G. Accuracy of the discrete dipole approximation for simulation of optical properties of gold nanoparticles. *J Nanophotonics* **4** (2010).
- 35 Sutradhar, A., Paulino, G. H. & Gray, L. J. *Symmetric galerkin boundary element method*. (Springer, 2008).
- 36 Jackson, J. D. *Classical electrodynamics*. 2d edn, (Wiley, 1975).
- 37 Wriedt, T. & Comberg, U. Comparison of computational scattering methods. *J Quant Spectrosc Ra* **60**, 411-423 (1998).

- 38 Schuck, P. J., Fromm, D. P., Sundaramurthy, A., Kino, G. S. & Moerner, W. E. Improving the mismatch between light and nanoscale objects with gold bowtie nanoantennas. *Phys Rev Lett* **94** (2005).
- 39 Muskens, O. L., Giannini, V., Sanchez-Gil, J. A. & Rivas, J. G. Strong enhancement of the radiative decay rate of emitters by single plasmonic nanoantennas. *Nano Lett* **7**, 2871-2875 (2007).
- 40 Schnell, M. *et al.* Controlling the near-field oscillations of loaded plasmonic nanoantennas. *Nat Photonics* **3**, 287-291 (2009).
- 41 Hicks, E. M. *et al.* Controlling plasmon line shapes through diffractive coupling in linear arrays of cylindrical nanoparticles fabricated by electron beam lithography. *Nano Lett* **5**, 1065-1070 (2005).
- 42 Duan, H. G., Hu, H. L., Kumar, K., Shen, Z. X. & Yang, J. K. W. Direct and Reliable Patterning of Plasmonic Nanostructures with Sub-10-nm Gaps. *Acs Nano* **5**, 7593-7600 (2011).
- 43 Jiao, X., Goeckeritz, J., Blair, S. & Oldham, M. Localization of near-field resonances in bowtie antennae: influence of adhesion layers. *Plasmonics* **4**, 37-50 (2009).
- 44 Huang, J.-S. *et al.* Atomically flat single-crystalline gold nanostructures for plasmonic nanocircuitry. *Nat Commun* **1**, 150 (2010).
- 45 Novotny, L. & van Hulst, N. Antennas for light. *Nat Photonics* **5**, 83-90 (2011).
- 46 Orloff, J., Swanson, L. & Utlaut, M. W. *High resolution focused ion beams : FIB and its applications : the physics of liquid metal ion sources and ion optics and their application to focused ion beam technology.* (Kluwer Academic/Plenum Publishers, 2003).
- 47 Alvarez-Puebla, R., Cui, B., Bravo-Vasquez, J.-P., Veres, T. & Fenniri, H. Nanoimprinted SERS-active substrates with tunable surface plasmon resonances. *The Journal of Physical Chemistry C* **111**, 6720-6723 (2007).
- 48 Guo, L. J. Nanoimprint lithography: Methods and material requirements. *Adv Mater* **19**, 495-513 (2007).
- 49 Boltasseva, A. Plasmonic components fabrication via nanoimprint. *J Opt a-Pure Appl Op* **11** (2009).
- 50 Trugler, A., Tinguely, J. C., Krenn, J. R., Hohenau, A. & Hohenester, U. Influence of surface roughness on the optical properties of plasmonic nanoparticles. *Phys Rev B* **83** (2011).
- 51 Yu, Y. Y., Chang, S. S., Lee, C. L. & Wang, C. R. C. Gold nanorods: Electrochemical synthesis and optical properties. *J Phys Chem B* **101**, 6661-6664 (1997).
- 52 Sun, Y. G. & Xia, Y. N. Shape-controlled synthesis of gold and silver nanoparticles. *Science* **298**, 2176-2179 (2002).
- 53 Wiley, B. J., Xiong, Y. J., Li, Z. Y., Yin, Y. D. & Xia, Y. N. Right bipyramids of silver: A new shape derived from single twinned seeds. *Nano Lett* **6**, 765-768 (2006).
- 54 Kim, F., Song, J. H. & Yang, P. Photochemical synthesis of gold nanorods. *J Am Chem Soc* **124**, 14316-14317 (2002).
- 55 Wiley, B. J. *et al.* Maneuvering the Surface Plasmon Resonance of Silver Nanostructures through Shape-Controlled Synthesis. *The Journal of Physical Chemistry B* **110**, 15666-15675 (2006).
- 56 Mock, J., Barbic, M., Smith, D., Schultz, D. & Schultz, S. Shape effects in plasmon resonance of individual colloidal silver nanoparticles. *The Journal of Chemical Physics* **116**, 6755-6759 (2002).
- 57 Wiley, B. J. *et al.* Synthesis and optical properties of silver nanobars and nanorice. *Nano Lett* **7**, 1032-1036 (2007).

- 58 Pham, T., Jackson, J. B., Halas, N. J. & Lee, T. R. Preparation and characterization of gold nanoshells coated with self-assembled monolayers. *Langmuir* **18**, 4915-4920 (2002).
- 59 Wang, H., Brandl, D. W., Le, F., Nordlander, P. & Halas, N. J. Nanorice: a hybrid plasmonic nanostructure. *Nano Lett* **6**, 827-832 (2006).
- 60 Cao, Y., Jin, R. & Mirkin, C. A. DNA-modified core-shell Ag/Au nanoparticles. *J Am Chem Soc* **123**, 7961-7962 (2001).
- 61 Fu, Y. *et al.* Fabrication of a Stable Polyelectrolyte/Au Nanoparticles Multilayer Film. *Macromolecular Rapid Communications* **23**, 256-259 (2002).
- 62 Gwo, S., Lin, M.-H., He, C.-L., Chen, H.-Y. & Teranishi, T. Bottom-Up Assembly of Colloidal Gold and Silver Nanostructures for Designable Plasmonic Structures and Metamaterials. *Langmuir* **28**, 8902-8908 (2012).
- 63 Yang, S.-C. *et al.* Plasmon hybridization in individual gold nanocrystal dimers: direct observation of bright and dark modes. *Nano Lett* **10**, 632-637 (2010).
- 64 Hermanson, K. D., Lumsdon, S. O., Williams, J. P., Kaler, E. W. & Velev, O. D. Dielectrophoretic assembly of electrically functional microwires from nanoparticle suspensions. *Science* **294**, 1082-1086 (2001).
- 65 Gangwal, S., Cayre, O. J. & Velev, O. D. Dielectrophoretic assembly of metallodielectric Janus particles in AC electric fields. *Langmuir* **24**, 13312-13320 (2008).
- 66 Lumsdon, S. O., Kaler, E. W. & Velev, O. D. Two-dimensional crystallization of microspheres by a coplanar AC electric field. *Langmuir* **20**, 2108-2116 (2004).
- 67 Singh, J. P., Lele, P. P., Nettesheim, F., Wagner, N. J. & Furst, E. M. One-and two-dimensional assembly of colloidal ellipsoids in ac electric fields. *Phys Rev E* **79**, 050401 (2009).
- 68 Tao, A. *et al.* Langmuir-Blodgett silver nanowire monolayers for molecular sensing using surface-enhanced Raman spectroscopy. *Nano Lett* **3**, 1229-1233 (2003).
- 69 Kim, F., Kwan, S., Akana, J. & Yang, P. Langmuir-Blodgett nanorod assembly. *J Am Chem Soc* **123**, 4360-4361 (2001).
- 70 Kraus, T. *et al.* Nanoparticle printing with single-particle resolution. *Nat Nanotechnol* **2**, 570-576 (2007).
- 71 Merlein, J. *et al.* Nanomechanical control of an optical antenna. *Nat Photonics* **2**, 230-233 (2008).
- 72 Heath, J. R., Knobler, C. M. & Leff, D. V. Pressure/temperature phase diagrams and superlattices of organically functionalized metal nanocrystal monolayers: the influence of particle size, size distribution, and surface passivant. *The Journal of Physical Chemistry B* **101**, 189-197 (1997).
- 73 Tao, A., Sinsermsuksakul, P. & Yang, P. Tunable plasmonic lattices of silver nanocrystals. *Nat Nanotechnol* **2**, 435-440 (2007).
- 74 Wang, H., Levin, C. S. & Halas, N. J. Nanosphere arrays with controlled sub-10-nm gaps as surface-enhanced Raman spectroscopy substrates. *J Am Chem Soc* **127**, 14992-14993 (2005).
- 75 Haynes, C. L. & Van Duyne, R. P. Nanosphere lithography: a versatile nanofabrication tool for studies of size-dependent nanoparticle optics. *The Journal of Physical Chemistry B* **105**, 5599-5611 (2001).
- 76 Hulteen, J. C. *et al.* Nanosphere lithography: size-tunable silver nanoparticle and surface cluster arrays. *The Journal of Physical Chemistry B* **103**, 3854-3863 (1999).
- 77 Kuznetsov, A. I. *et al.* Laser-induced transfer of metallic nanodroplets for plasmonics and metamaterial applications. *J Opt Soc Am B* **26**, B130-B138 (2009).



- 78 Inasawa, S., Sugiyama, M. & Yamaguchi, Y. Laser-induced shape transformation of gold nanoparticles below the melting point: The effect of surface melting. *J Phys Chem B* **109**, 3104-3111 (2005).
- 79 Kuznetsov, A. I. *et al.* Laser Fabrication of Large-Scale Nanoparticle Arrays for Sensing Applications. *Acs Nano* **5**, 4843-4849 (2011).
- 80 Wang, D., Ji, R. & Schaaf, P. Formation of precise 2D Au particle arrays via thermally induced dewetting on pre-patterned substrates. *Beilstein J Nanotech* **2**, 318-326 (2011).
- 81 Shechtman, D., Blech, I., Gratias, D. & Cahn, J. W. Metallic Phase with Long-Range Orientational Order and No Translational Symmetry. *Phys Rev Lett* **53**, 1951-1953 (1984).
- 82 Spence, T. G. & Werner, D. H. Design of Broadband Planar Arrays Based on the Optimization of Aperiodic Tilings. *Antennas and Propagation, IEEE Transactions on* **56**, 76-86 (2008).
- 83 Namin, F., Petko, J. S. & Werner, D. H. Analysis and Design Optimization of Robust Aperiodic Micro-UAV Swarm-Based Antenna Arrays. *Ieee T Antenn Propag* **60**, 2295-2308 (2012).
- 84 Della Villa, A. *et al.* A comparative study of representative categories of EBG dielectric quasi-crystals. *Ieee Antenn Wirel Pr* **5**, 331-334 (2006).
- 85 Della Villa, A. *et al.* Band gap formation and multiple scattering in photonic quasicrystals with a Penrose-type lattice. *Phys Rev Lett* **94** (2005).
- 86 Namin, F. A., Wang, X. & Werner, D. H. Reflection and transmission coefficients for finite-sized aperiodic aggregates of spheres. *J. Opt. Soc. Am. B* **30**, 1008-1016 (2013).
- 87 Bauer, C., Kobiela, G. & Giessen, H. 2D quasiperiodic plasmonic crystals. *Sci Rep-Uk* **2** (2012).
- 88 Gopinath, A., Boriskina, S. V., Reinhard, B. M. & Dal Negro, L. Deterministic aperiodic arrays of metal nanoparticles for surface-enhanced Raman scattering (SERS). *Opt Express* **17**, 3741-3753 (2009).
- 89 Gopinath, A., Boriskina, S. V., Feng, N. N., Reinhard, B. M. & Dal Negro, L. Photonic-plasmonic scattering resonances in deterministic aperiodic structures. *Nano Lett* **8**, 2423-2431 (2008).
- 90 Solis, D., Jr. *et al.* Turning the Corner: Efficient Energy Transfer in Bent Plasmonic Nanoparticle Chain Waveguides. *Nano Lett* (2013).
- 91 Maier, S. A. *et al.* Observation of coupled plasmon-polariton modes of plasmon waveguides for electromagnetic energy transport below the diffraction limit. *Materials and Devices for Optoelectronics and Microphotonics* **722**, 431-436 (2002).
- 92 Maier, S. A., Kik, P. G. & Atwater, H. A. Observation of coupled plasmon-polariton modes in Au nanoparticle chain waveguides of different lengths: Estimation of waveguide loss. *Appl Phys Lett* **81**, 1714-1716 (2002).
- 93 Maier, S. A. *et al.* Local detection of electromagnetic energy transport below the diffraction limit in metal nanoparticle plasmon waveguides. *Nat Mater* **2**, 229-232 (2003).
- 94 Zou, S. L. & Schatz, G. C. Narrow plasmonic/photonic extinction and scattering line shapes for one and two dimensional silver nanoparticle arrays. *J Chem Phys* **121**, 12606-12612 (2004).
- 95 Hicks, E. M. *et al.* Controlling plasmon line shapes through diffractive coupling in linear arrays of cylindrical nanoparticles fabricated by electron beam lithography. *Nano Lett* **5**, 1065-1070 (2005).
- 96 Graf, R. F. *Modern dictionary of electronics*. 7th edn, (Newnes, 1999).
- 97 Berland, B. Photovoltaic Technologies Beyond the Horizon: Optical Rectenna Solar Cell (National Renewable Energy Laboratory, U.S., 2009).

- 98 Kuhn, S., Hakanson, U., Rogobete, L. & Sandoghdar, V. Enhancement of single-molecule fluorescence using a gold nanoparticle as an optical nanoantenna. *Phys Rev Lett* **97** (2006).
- 99 Mohammadi, A., Sandoghdar, V. & Agio, M. Gold nanorods and nanospheroids for enhancing spontaneous emission. *New J Phys* **10** (2008).
- 100 Alu, A. & Engheta, N. Hertzian plasmonic nanodimer as an efficient optical nanoantenna. *Phys Rev B* **78** (2008).
- 101 Pramod, P. & Thomas, K. G. Plasmon Coupling in Dimers of Au Nanorods. *Adv Mater* **20**, 4300-4305 (2008).
- 102 Fromm, D. P., Sundaramurthy, A., Schuck, P. J., Kino, G. & Moerner, W. E. Gap-dependent optical coupling of single "Bowtie" nanoantennas resonant in the visible. *Nano Lett* **4**, 957-961 (2004).
- 103 Kosako, T., Kadoya, Y. & Hofmann, H. F. Directional control of light by a nano-optical Yagi-Uda antenna. *Nat Photonics* **4**, 312-315 (2010).
- 104 Li, J. J., Salandrino, A. & Engheta, N. Shaping light beams in the nanometer scale: A Yagi-Uda nanoantenna in the optical domain. *Phys Rev B* **76** (2007).
- 105 Luk'yanchuk, B. *et al.* The Fano resonance in plasmonic nanostructures and metamaterials. *Nat Mater* **9**, 707-715 (2010).
- 106 Monticone, F. & Alu, A. Metamaterials and plasmonics: From nanoparticles to nanoantenna arrays, metasurfaces, and metamaterials. *Chinese Phys B* **23** (2014).
- 107 Alu, A. & Engheta, N. Input impedance, nanocircuit loading, and radiation tuning of optical nanoantennas. *Phys Rev Lett* **101** (2008).
- 108 Alu, A. & Engheta, N. Tuning the scattering response of optical nanoantennas with nanocircuit loads. *Nat Photonics* **2**, 307-310 (2008).
- 109 Neubrech, F. *et al.* Resonant Plasmonic and Vibrational Coupling in a Tailored Nanoantenna for Infrared Detection. *Phys Rev Lett* **101**, 157403 (2008).
- 110 Ditlbacher, H. *et al.* Silver Nanowires as Surface Plasmon Resonators. *Phys Rev Lett* **95**, 257403 (2005).
- 111 Shegai, T. *et al.* Unidirectional broadband light emission from supported plasmonic nanowires. *Nano Lett* **11**, 706-711 (2011).
- 112 Wang, H., Fu, K., Drezek, R. A. & Halas, N. J. Light scattering from spherical plasmonic nanoantennas: effects of nanoscale roughness. *Appl. Phys. B* **84**, 191-195 (2006).
- 113 Chen, P. Y. & Alu, A. Optical nanoantenna arrays loaded with nonlinear materials. *Phys Rev B* **82** (2010).
- 114 Liu, N. *et al.* Individual Nanoantennas Loaded with Three-Dimensional Optical Nanocircuits. *Nano Lett* **13**, 142-147 (2013).

## **Chapter 2**

### **Synthesis of 2D Quasicrystal Spherical Nanoparticle Arrays**

In this chapter, a new nanofabrication method that is based on gold (Au)-enhanced oxidation of lithographically defined Au and amorphous silicon (*a*-Si) nanoparticle stacks was developed to create spherical plasmonic nanoparticle arrays with controlled nanoparticle placement, diameter and spacing. The spherical nanoparticles allowed accurate electromagnetic modeling of the optical transmission, reflection, and scattering spectra of quasicrystal arrays using a modified Generalized Mie Theory (GMT) approach. The optical spectra of a periodic nanoparticle array and two quasicrystal nanoparticle arrays were characterized through normally incident specular transmission measurements in the visible wavelength regime, and excellent quantitative agreement was achieved with simulation. The broadband response of the Ammann-Beenker quasicrystal array and the multiband response of the Penrose array was further investigated by studying the interaction of the photonic resonance and the plasmonic resonance of the arrays.

Design optimization was conducted by electromagnetic simulations performed by Dr. Frank Namin under the guidance of Prof. Douglas H. Werner in the Electrical Engineering Department at Penn State University.

#### **2.1 Background and Motivation**

Advanced nanofabrication techniques have enabled rapid progress in realizing plasmonic nanoparticle arrays with complex optical properties that are determined by the intrinsic particle geometry and the extrinsic environment. These structures are being explored for a wide range of applications that rely on either near-field enhancement or far-field diffractive coupling, including

sensors<sup>1,2</sup>, solar cells<sup>3-8</sup>, waveguides<sup>9-12</sup>, and metamaterials<sup>13-15</sup>. Strong and sharp plasmonic resonances from far-field diffractive coupling in one-dimensional (1D) and two-dimensional (2D) periodic configurations have been recently reported both theoretically<sup>16,17</sup> and experimentally<sup>18</sup>. It was found that the resonance frequency depends sensitively on the geometry and the arrangement of the nanoparticles, the dielectric environment, the polarization and angle of the incident light. These structures can be used as refractive index sensors with a sensitivity of a few hundred nm per refractive index unit (RIU)<sup>2</sup> in biosensing applications<sup>1</sup>. Periodic and quasicrystal nanoparticle arrays<sup>19</sup> that exhibit a broadband scattering response in the visible wavelength regime have the potential to enhance solar cell conversion efficiencies. Near-field dipole-dipole interactions between closely spaced nanoparticles allow transport of confined plasmonic excitations below the diffraction limit<sup>9</sup> and without radiation loss<sup>10</sup>, which makes these structures candidates for waveguide applications. The high effective permittivity values caused by the plasmonic resonance of the nanoparticles can also allow them to act as magnetic dipoles, which can be used to create negative permeability metamaterials<sup>15</sup> at optical frequencies.

A particular area of interest in recent years has been the development of plasmonic structures that are based on quasicrystal tilings<sup>19-29</sup>. The unique properties of these structures make them strong candidates for applications such as enhanced absorption with large angular tolerance for solar cells<sup>21,30</sup>, surface enhanced Raman scattering (SERS) substrates<sup>22</sup>, and broadband plasmonic enhancement devices<sup>19</sup>. The lack of simulation tools to accurately and efficiently model quasicrystal nanoparticle arrays has presented significant challenges to the field. Traditionally, the electromagnetic properties of metamaterials and photonic crystals have been determined by exploiting their translational symmetry, or periodicity. This approach dramatically simplifies the analysis by allowing the use of periodic boundary conditions, which only requires a solution for Maxwell's equations in one unit cell rather than for the entire structure. However, quasicrystals

lack translational symmetry, and hence cannot be modeled accurately using periodic boundary conditions.

Analyzing plasmonic structures using traditional finite-difference and finite-element techniques requires considerable computational resources even for relatively simple structures. For this reason, there has been interest in developing more efficient analytical tools that offer solutions several orders of magnitude faster than these methods. Examples include methods such as the discrete dipole approximation (DDA) and GMT. The DDA method is not limited to a spherical particle shape. However, it only accounts for dipole interactions and it neglects higher order terms that are important in nanoparticles with large dimensions or for arrays of closely packed particles. The GMT<sup>31-33</sup> method accounts for higher-order mode interactions and provides better accuracy. However, it is limited to particles with spherical shape. To bridge the gap between simulation and experiment, robust and reproducible nanofabrication methods must be developed to form spherical nanoparticle arrays that can be modelled by the GMT method.

In this research, a new nanofabrication approach that employs electron-beam lithography and subsequent thermal treatment was developed to create two-dimensional (2D) spherical plasmonic nanoparticle arrays. This technique combines the merits of deterministic lithographic patterning with those of laser heating approaches, thereby enabling individual particle control of sphere placement, array placement, and interparticle spacing down to the nanometer scale. In this process, cylindrical Au particles formed by top-down patterning are transformed into spheres when subjected to a thermal treatment in oxygen (O<sub>2</sub>). The final spherical Au nanoparticle diameter and inter-particle spacing is determined entirely by the starting lithographic pattern and the evaporated Au volume. This thermal process eliminates fabrication-induced variations in the cylindrical particle geometry, which can distort the optical spectrum and broaden the plasmonic peaks. Periodic and quasicrystal arrays were fabricated using this approach, and excellent quantitative agreement was obtained between the experimentally measured and GMT simulated transmission

spectra for both types of arrays. The broadband transmission properties of Ammann-Beenker quasicrystal and the multiband properties of the Penrose quasicrystal were further explored by studying the interaction of the photonic and plasmonic resonances of the Au nanoparticle arrays.

## 2.2 Periodic Cylindrical Nanoparticle Arrays

Typically plasmonic nanoparticle arrays have been fabricated using standard lithographic patterning followed by lift-off of the evaporated metal layer<sup>2,9,15,34</sup>. In this research, this top-down method was used to produce the periodic cylindrical nanoparticle array shown in Figure 2-1 as a control sample for subsequent analysis of the quasicrystal nanoparticle arrays. The square lattice structure has individual cylindrical Au nanoparticles that are 135nm in diameter and 90nm in height, and the particles are surrounded by silicon dioxide (SiO<sub>2</sub>). The particle diameter is large enough to ensure that the extinction is dominated by scattering rather than absorption, and at same time small enough to minimize significant plasmonic oscillation damping due to radiation<sup>35</sup>. The center-to-center spacing of the nanoparticles in the square array is 360nm, which generates a photonic mode at a wavelength of approximately 540 nm in SiO<sub>2</sub>. This is in close proximity to the 560nm plasmonic resonance wavelength of individual Au nanoparticles, which gives a photonic-plasmonic hybrid mode that enhances the resonance over that of a single isolated particle.

The Au nanoparticle arrays were fabricated by first spinning a double-layer electron-beam resist (Microchem PMGI and PMMA) on a cleaned fused silica wafer at a speed of 5000 RPM for 45 sec. The resist was soft-baked by heating the PMGI layer to 190°C for 5min and the PMMA layer at 180°C for 3min. The features were defined by exposing the resist at a dose of 150μC/cm<sup>2</sup> (spot size 30nm and beam current 30nA) using a Vistec EBPG5200 Direct-Write Electron Beam Lithography System (DWEBL). Following electron-beam exposure, the resist layer was developed in MIBK: IPA=1:3 for 2min and 101A developer for 1min. The metal was deposited by electron-

beam evaporation of Ti/Au (3 nm/90 nm). The array was completed by lifting off the metal film by dissolving the resist in Microposit Remover 1165 (Microchem). Top-view and cross-sectional field emission scanning electron microscope (FESEM) images of the fabricated structure are shown in Figure 2-1 (a) – (c).

The asymmetry of the fabricated structure, with an air half space on the top and a fused silica half space on the bottom, results in decoherence of the collectively scattered waves during optical characterization<sup>36</sup>. This degrades both the intensity and bandwidth of the resonant features in comparison to simulation, which assumes that the particle array is embedded in a homogeneous SiO<sub>2</sub> medium. To reproduce the conditions used in the simulation, the nanofabricated structure was capped with a second used silica substrate, and index matching oil ( $n=1.51$ ) was introduced in the space between the two substrates. Normal incidence specular transmission spectra were measured using a UV-VIS spectrometer (PerkinElmer Lambda 9500 UV-VIS-NIR Spectrophotometer) with a standard detector accessory. Unpolarized broadband white light illuminated the sample through a 2×2 mm<sup>2</sup> circular aperture. The absolute transmission was determined by normalizing the measured transmittance of the nanoparticle array to that of the blank substrate.

By comparing the measured transmission spectrum of the fabricated Au nanoparticle array with full-wave electromagnetic simulations using periodic boundary conditions, it is possible to determine the Au metal model that most accurately matches experiment. Figure 2-1(d) shows strong agreement between experiment and theory when the measured optical properties of the evaporated Au, which were determined by spectroscopic ellipsometry of a thin film witness sample deposited under the same conditions as the nanoparticle (see Appendix A3), are used in the model. Replacing the measured thin film values with the published Johnson-Christy (JC) crystalline Au properties<sup>37</sup> caused the position of the transmission minimum to shift from 640nm to 670nm and the bandwidth to broaden from 50nm to 84nm ((Lorentz function curve fit). The red shift is caused by the smaller refractive index values,  $n$ , of the deposited Au compared to the crystalline

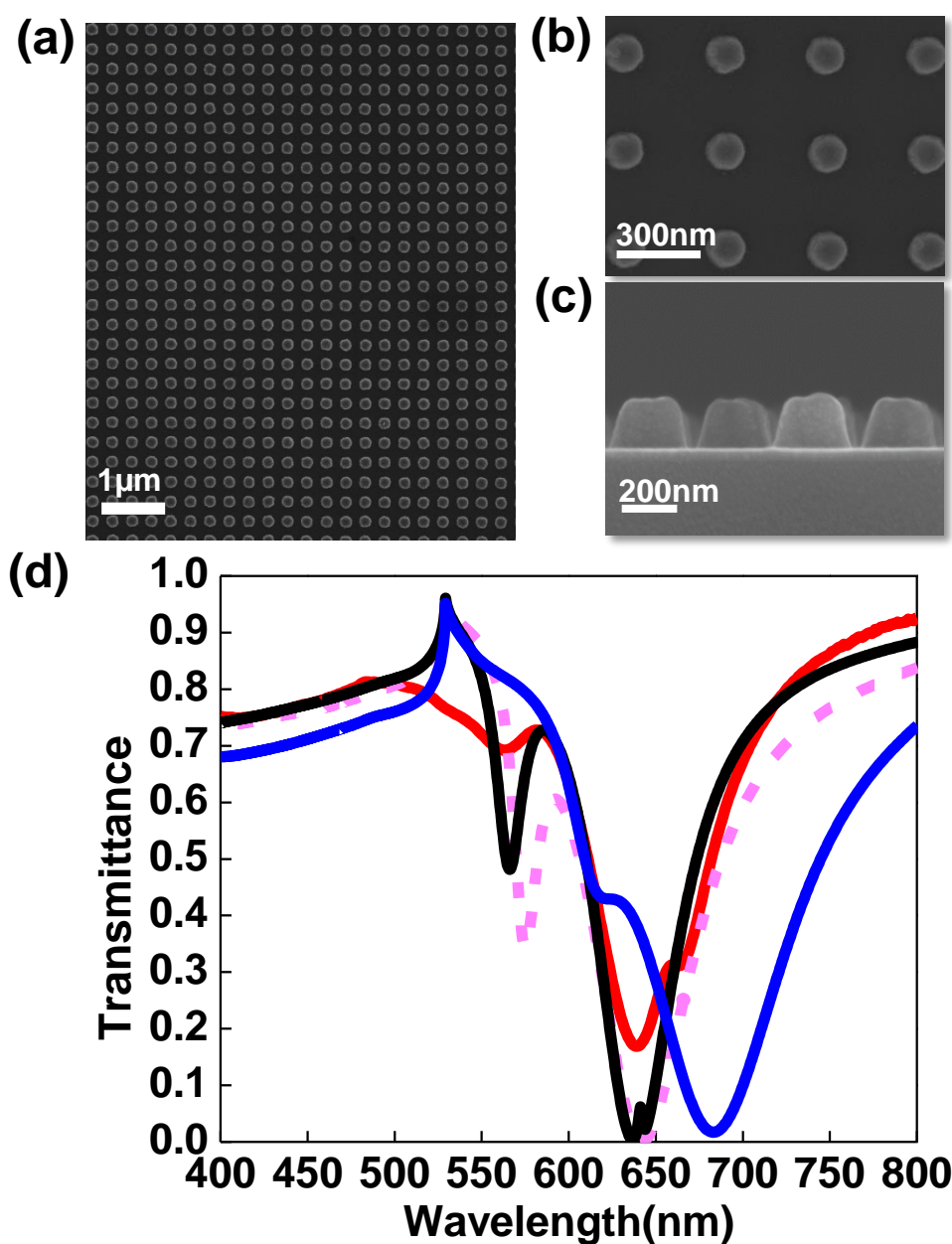


Figure 2-1. (a) FESEM image of fabricated periodic cylindrical nanoparticle arrays with 135nm diameter, 90nm height, and 360nm interparticle spacing; (b) top view and (c) cross sectional view of the array; (d) Measured (red) and simulated (black, blue, pink) transmission spectra of the periodic cylindrical nanoparticle arrays. Black: corrected cylindrical shape from SEM with measured Au properties; Blue: vertical sidewall with crystalline JC Au properties; Pink: vertical sidewall with measured Au properties.



JC values. The peak width broadening is due to the differences in coupling between the plasmonic and photonic modes. Specifically, the plasmonic peak for the thin-film deposited Au cylinders is at 560nm, while that of bulk crystalline Au particles would be at 620nm. Because both plasmonic modes are found at a longer wavelength than the photonic mode around 540nm, the photonic mode is evanescent, and very little radiative coupling can occur<sup>38</sup>. The plasmonic peak for deposited Au nanoparticles is closer to the photonic peak, which results in a sharper resonance in this case.

As illustrated in Figure 2-1(c), the nanofabricated cylindrical nanoparticles also had tilted sidewalls that varied from 74° to 81° around the periphery of the particle. Comparing the simulated optical response of the ideal cylindrical particle with vertical sidewalls to the response of a particle array with asymmetric tilted sidewalls in Figure 2-1(d) shows that the dominant plasmonic resonance is transformed into a superposition of resonances that are slightly offset from one another. For this sample, the plasmonic resonance is a superposition of two primary resonances centered at approximately 640nm and 670nm. Further broadening of the spectrum can be explained by variations in the diameter and sidewall angles across the large-area Au nanoparticle array.

This result demonstrates that the peak position and bandwidth is sensitively dependent on the Au properties and particle geometry. This dependence can cause large variations in the optical response of Au nanoparticle arrays deposited with different tools or even in different deposition runs. Thus, care must be taken to develop robust and reproducible fabrication processes to minimize fabrication induced non-idealities.

### **2.3 Simulation Methods**

Simulation of the quasicrystal plasmonic nanoparticle arrays without translation invariance requires significant computational resources because periodic boundary conditions cannot be applied. To facilitate a quantitative comparison between GMT simulation and measurements of a

nanofabricated sample, an incident beam having a finite beam width smaller than the array area was employed to eliminate diffraction by spheres at the edges of the lattice. The finite beam-width was obtained by placing a circular aperture in front of a plane wave, which is representative of the realistic experimental conditions. The modified GMT approach<sup>28</sup>, which is summarized in this section, was developed by Dr. Frank Namin under the guidance of Prof. Douglas H. Werner in the Electrical Engineering Department at Penn State University.

Using far-field expressions for the scattered fields, generalized transmission and reflection coefficients can be determined based on the total far-field energy fluxes. The expression for the fields diffracted by the circular aperture of radius  $a$  placed in front of a linearly polarized monochromatic wave with angular frequency  $\omega$  and  $e^{-i\omega t}$  time dependence can be obtained using the Kirchhoff integral<sup>39</sup>. For an incident electric field  $xe^{ikz}$ , where  $k = 2\pi/\lambda$ , in the  $z < 0$  region, and a circular aperture of radius  $a$  in the  $xy$ -plane ( $z = 0$ ), the diffracted field in the  $z > 0$  region is

$\mathbf{E}_{\text{inc}} = E_\theta \hat{\boldsymbol{\theta}} + E_\phi \hat{\boldsymbol{\phi}}$  with  $E_\theta$  and  $E_\phi$  given by:

$$\begin{aligned} E_\theta &= \frac{iakJ_1(ka \sin \theta) \cos \phi [j_1(\rho) + ij_2(\rho)]}{\sin \theta} \\ E_\phi &= \frac{-iakJ_1(ka \sin \theta) \sin \phi \cos \theta [j_1(\rho) + ij_2(\rho)]}{\sin \theta} \end{aligned} \quad (1)$$

where  $\rho = kr$ ,  $J_1$  is the Bessel function of the first kind of order 1 and  $j_1$  and  $j_2$  denote the spherical Bessel functions of the first kind of orders 1 and 2, respectively. To use the GMT method, the fields in Eq. (1) must be expanded in terms of vector spherical wave functions (VSWFs)  $\mathbf{N}_{mn}^{(1)}$  and  $\mathbf{M}_{mn}^{(1)}$  as:

$$\mathbf{E}_{\text{inc}} = -\sum_{n=1}^{\infty} \sum_{m=-n}^n iE_{mn} [p_{mn} \mathbf{N}_{mn}^{(1)} + q_{mn} \mathbf{M}_{mn}^{(1)}] \quad (2)$$

where  $p_{mn}$  and  $q_{mn}$  are the expansion coefficients. Closed-form expressions for  $p_{mn}$  and  $q_{mn}$  were derived by Namin *et al*<sup>28</sup>.

One more distinction between having an incident plane wave and an incident wave with a finite beam-width must be considered. The standard GMT method for a system of  $N$  spheres defines the  $N$  local coordinate systems by sphere centers. The modified GMT requires that the primary expansion coefficients  $p_{mn}$  and  $q_{mn}$ , which correspond to the global coordinate system with its origin at  $(0, 0, 0)$ , are expressed in terms of VSWFs of the local coordinate systems. It can be shown that if  $p_{mn}$  and  $q_{mn}$  denote the expansion coefficients in the  $j^{\text{th}}$  system with its origin at  $(X^j, Y^j, Z^j)$ , they only differ from primary expansion coefficients by a constant phase term<sup>31</sup> for an incident plane wave with infinite beam width. However, this is not valid for an incident field of the form shown in Eq (1). In this case, local expansion coefficients  $p_{mn}$  and  $q_{mn}$  must be evaluated by applying vector translational addition theorems<sup>40</sup>.

By imposing the electromagnetic boundary conditions for the tangential components of the electric and magnetic fields, the expansion coefficients for the internal and scattered fields can be determined for all of the particles in the array. The expansion coefficients for scattered fields associated with the  $j^{\text{th}}$  sphere are denoted by  $a_{mn}^j$  and  $b_{mn}^j$ , and the scattered electric field by the  $j^{\text{th}}$  sphere is given by:

$$\mathbf{E}_s^j = \sum_{n=1}^{\infty} \sum_{m=-n}^n iE_{mn} [a_{mn}^j \mathbf{N}_{mn}^{(3)} + b_{mn}^j \mathbf{M}_{mn}^{(3)}] \quad (3)$$

The total scattered field in the primary coordinate system can be obtained by applying vector translational addition theorems<sup>41,42</sup> to sum all of the individual scattered fields. In the far-field, much simpler asymptotic expressions for the total scattering coefficients were derived by Xu<sup>43</sup> *et al.* by expanding the total scattered electric field as:

$$\mathbf{E}_s(\rho, \theta, \phi) = \sum_{n=1}^{\infty} \sum_{m=-n}^n iE_{mn} [a_{mn} \mathbf{N}_{mn}^{(3)} + b_{mn} \mathbf{M}_{mn}^{(3)}] \quad (4)$$

Xu derived asymptotic expressions for the total scattering coefficient as<sup>43</sup>:

$$\begin{aligned}
a_{mn} &= \sum_{j=1}^L \exp(-ik\Delta^j) a_{mn}^j \\
b_{mn} &= \sum_{j=1}^L \exp(-ik\Delta^j) b_{mn}^j
\end{aligned} \tag{5}$$

where  $\Delta^j = X^j \sin \theta \cos \phi + Y^j \sin \theta \sin \phi + Z^j \cos \theta$  and  $(X^j, Y^j, Z^j)$  denotes the center of the  $j^{\text{th}}$  sphere. It can be shown that for  $\theta = 0$ , the scattered far-field has the form:

$$\mathbf{E}_s(\rho, 0, 0) = \frac{ie^{i\rho}}{\rho} \sum_{n=1}^{\infty} \sqrt{2n+1} [a_{1n} + b_{1n}] \hat{\boldsymbol{\theta}} \tag{6}$$

Also from Eq. (1) it follows that the incident field for  $\theta = 0$  is:

$$\mathbf{E}_{\text{inc}}(\rho, 0, 0) = -i \frac{(ak)^2 e^{i\rho}}{2\rho} \hat{\boldsymbol{\theta}} \tag{7}$$

Hence, the total far-field for  $\theta = 0$  can be expressed as the sum of incident and scattered fields, and is given by:

$$\mathbf{E}_{\text{Total}}(\rho, 0, 0) = \frac{ie^{i\rho}}{\rho} \left( \frac{-(ak)^2}{2} + \sum_{n=1}^{\infty} \sqrt{2n+1} [a_{1n} + b_{1n}] \right) \hat{\boldsymbol{\theta}} \tag{8}$$

The generalized transmission coefficient ( $T$ ) can be defined in terms of the total far-field energy flux relative to that of the incident field energy flux for  $\theta = 0$  as:

$$T = \left| \frac{\mathbf{E}_{\text{Total}}(\rho, 0, 0)}{\mathbf{E}_{\text{inc}}(\rho, 0, 0)} \right|^2 \tag{9}$$

After simplifying, the transmission coefficient can be expressed as:

$$T = \left| 1 - \frac{2}{(ak)^2} \sum_{n=1}^{\infty} \sqrt{2n+1} [a_{1n} + b_{1n}] \right|^2 \tag{10}$$

The expression in Eq. (10) can be used to calculate the specular transmittance of finite-sized array of spheres that can be directly compared to the experimental measurement results.

## 2.4 Cylindrical Ammann-Beenker Au Nanoparticle Arrays

Ammann-Beenker aperiodic arrays can be created by combining a set of square and rhombohedral prototiles with vertex angles of  $\pi/4$  and  $3\pi/4$  as was first done by Ammann<sup>44</sup> in the 1970s, or by the cut-and-project method as done by Beenker in 1982<sup>45</sup>. Figure 2-2(a) shows an example of an Ammann-Beenker quasicrystal constructed from prototiles with equal side length  $a$  via inflation rules. Plasmonic arrays are created by positioning noble metal nanoparticles at the vertices of the arrays, as illustrated in Figure 2-2 (b). Due to the aperiodicity, the tilings lack translational symmetry, but exhibit self-similarity properties. Diffractograms of Ammann-Beenker tilings reveal their eight-fold rotational symmetry and long-range order (see Section 2.7). In contrast to periodic crystals, which are defined by a primitive set of reciprocal vectors, the diffraction pattern of this quasicrystal is filled with reciprocal vectors of high intensity. This makes this tiling a promising candidate for realizing a broadband optical response.

In this thesis research, an Ammann-Beenker Au nanoparticle array was fabricated using the process flow and characterization procedure described in Section 2.2. The array is composed of cylindrical Au nanoparticles that are 160nm diameter and 60nm tall. A prototile side length  $a$  of 392nm was selected to obtain a broadband plasmonic response. A FESEM image of the fabricated Ammann-Beenker plasmonic quasicrystal is shown in Figure 2-2(c).

Figure 2-2 (d) compares the experimentally measured specular transmission spectrum (red) to the spectrum determined by GMT simulation using the measured thin-film Au properties. In contrast to the periodic structure that was simulated using the actual cylindrical nanoparticles, in this case, neither the position of the transmission minimum nor the bandwidth of the measured spectrum agrees with theory. In the simulation, the spectrum is composed of a primary resonance at a wavelength of 626nm with three weaker satellite resonances at 570nm, 682nm and 810nm. The three satellite resonances merge with the primary resonance to give a broadband response. In

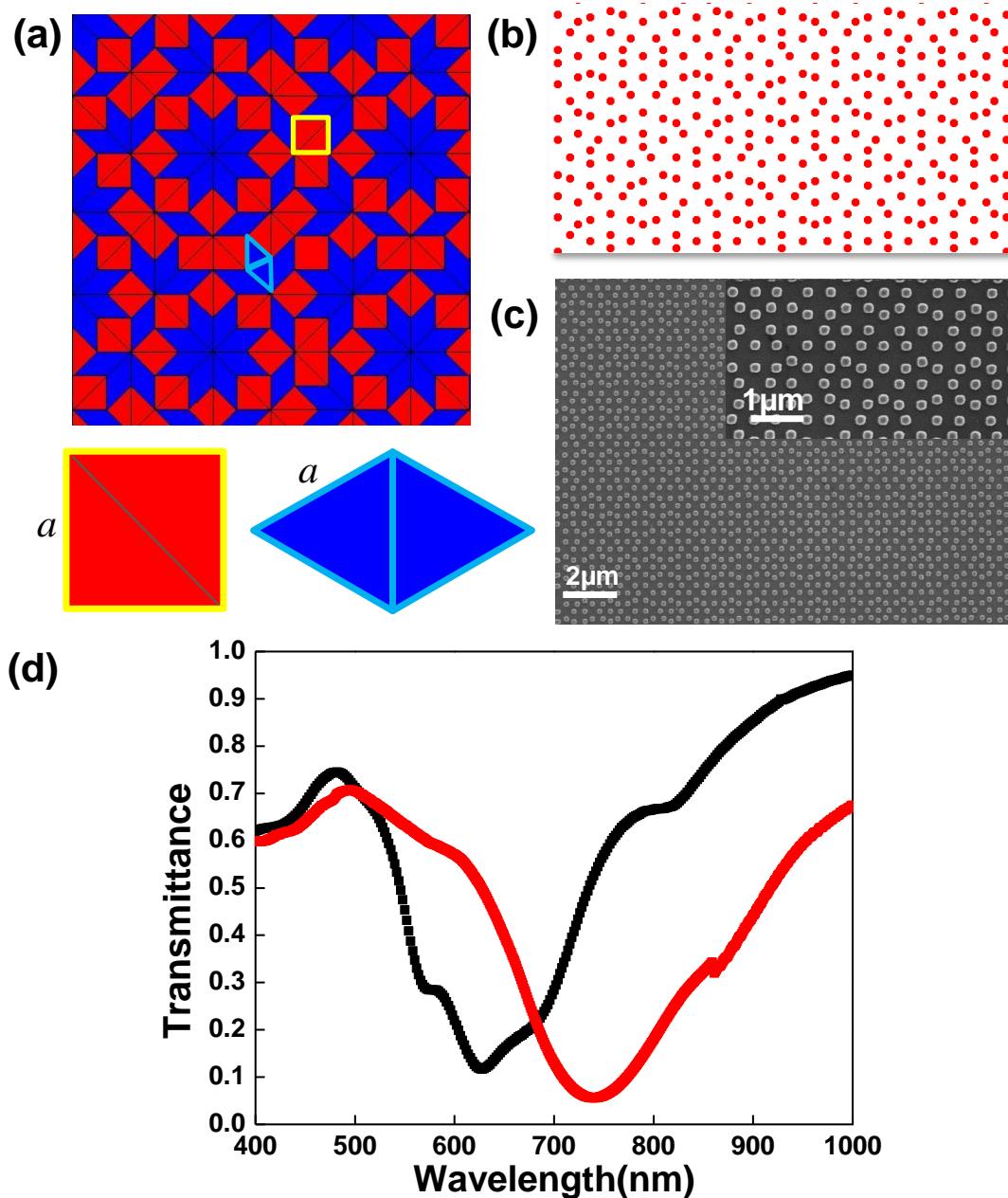


Figure 2-2. (a) Quasicrystal Ammann-Beenker tiling showing the square and rhombohedral prototiles in yellow and blue; (b) The designed Ammann-Beenker quasicrystal with a prototile side length  $a$  of 392nm; (c) FESEM image of a fabricated cylindrical Ammann-Beenker quasicrystal with nanoparticles that are 160nm in diameter and 60nm tall; Inset: Enlarged view of the Ammann-Beenker array; (d) Measured (red) and simulated (black) transmission spectra of the Ammann-Beenker cylindrical nanoparticle arrays. The simulation was performed using the measured thin-film Au properties and a spherical nanoparticle geometry.

contrast, the experimental curve resolves a primary resonance at 740nm with additional weaker resonances at 600nm and 950nm.

The optical response of the periodic cylindrical nanoparticle arrays presented in Section 2.2 agrees well with theory when the measured Au thin film properties and the correct nanoparticle shape are used in the model. This suggests that the discrepancy in optical response of the Ammann-Beenker quasicrystal array is due to the difference between the cylindrically shaped nanoparticles in the fabricated sample and the spherically shaped particles in the simulation. The red-shift in the transmission spectrum of the quasicrystal is also consistent with the shape-dependent resonance shift of isolated metal nanoparticles because of the weaker restoring force in cylindrical nanoparticles as compared to spherical nanoparticles<sup>46</sup>.

## 2.5 Nanofabrication of Spherical Nanoparticle Arrays by Au Enhanced Oxidation

This section describes a new hybrid nanofabrication technique that was developed to create plasmonic arrays with nearly ideal spherical Au nanoparticles. In this approach, a lithographically defined array of cylindrical nanoparticles composed of a stack of thin amorphous-Si (*a*-Si) and Au layers is converted into crystalline, spherical Au nanoparticles surrounded by a SiO<sub>2</sub> shell through Au enhanced oxidation. The Au enhanced oxidation process was first reported on a planar Si substrate by Hiraki<sup>47,48</sup> *et al.* in 1971. This method was later extended to create non-uniformly spaced Au nanoparticle arrays along VLS-grown Si nanowires capped with an Au catalyst tip<sup>49,50</sup>.

In the Au-enhanced oxidation process, Au must be in direct contact with Si with no interfacial barrier such as SiO<sub>2</sub>. When the Au-Si structure is heated to a temperature higher than the Au-Si eutectic temperature of ~365°C (from the equilibrium phase diagram), the Si will first dissolve in the Au droplet that is formed at elevated temperatures, and then the Si atoms will diffuse to the surface of the droplet. If the heated Au-Si droplet is exposed to O<sub>2</sub> at the same time, the Si

atoms that reach the surface of the droplet will be thermally oxidized to form  $\text{SiO}_2$ . It was shown by Westwater *et al.*<sup>51</sup> that Si atoms are extracted from the Au-Si droplet to form  $\text{SiO}_2$  at a much higher rate than direct thermal oxidation of crystalline Si without Au, resulting in the so-called Au-enhanced oxidation of Si. In previous work, Au was deposited on the tip of a long Si nanowire, which provides a nearly unlimited source of Si for oxidation. In these cases, the oxidation-induced depletion of Si causes additional Si to dissolve in the Au-Si droplet, which allows for the continued growth of  $\text{SiO}_2$  with increasing oxidation time. For long Au-tipped Si nanowires, the hemispherical Au-Si droplet recedes down the wire as the Si nanowire is consumed to form a  $\text{SiO}_2$  wire with a 44% volume increase with respect to the starting wire dimensions<sup>50</sup>.

The research in this thesis adapted the Au-enhanced oxidation process to fabricate 2D periodic and quasicrystal Au nanoparticle arrays on planar substrates of arbitrary material. This approach overcomes limitations of earlier methods to provide all of the essential features needed for high-quality plasmonic nanoparticle array devices, including: (1) the formation of spherical Au nanoparticles with optical properties equivalent to bulk crystalline Au (JC values); and (2) the direct integration of Au nanoparticles with well-controlled particle size and placement on alternative substrates.

Figure 2-3 illustrates the process flow used to create Au nanoparticle arrays on optically transparent fused silica substrates. First, cylindrical nanoparticles composed of a stack of electron-beam evaporated *a*-Si and Au layers are defined by electron-beam lithography and lift-off. The particle positions are determined by top-down lithographic patterning, and the particle diameter is specified by the total volume of the evaporated Au layer. The two-layer *a*-Si/Au stack is deposited sequentially without breaking vacuum, which ensures that the interface between the *a*-Si and Au layer is abrupt and free of interfacial oxides. Next, the structure is heated above the Au-Si eutectic temperature in a tube furnace with flowing dry  $\text{O}_2$ . In contrast to large area Au thin films that



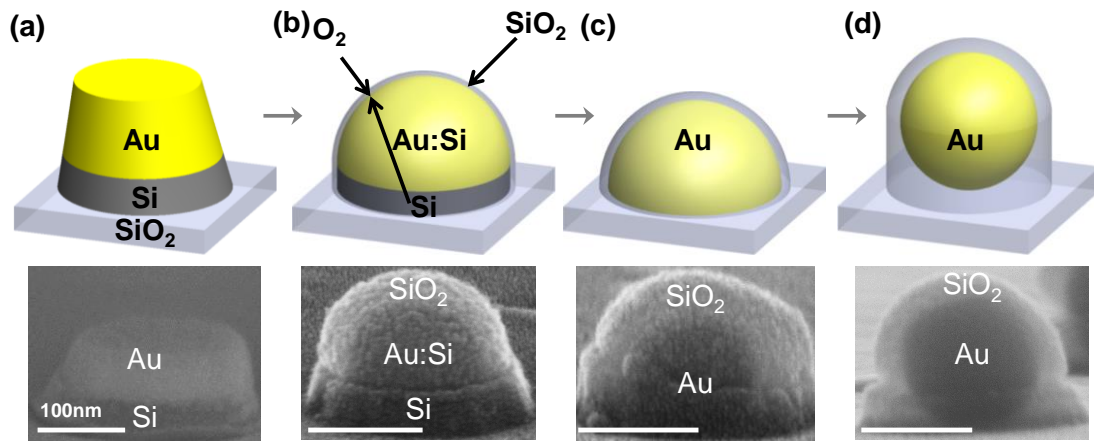


Figure 2-3. Schematic diagrams and FESEM images showing the evolution of the Au: (a) evaporated Au is in direct contact with Si at  $t=0\text{min}$ ; (b) Au hemisphere is encapsulated in  $\text{SiO}_2$  and there is Si left for oxidation at  $t=5\text{min}$ ; (c) Au hemisphere is in direct contact with the substrate and no more Si can be provided for the oxidation at  $t=30\text{min}$ ; (d) formation of Au spherical nanoparticle to reduce the surface energy at  $t=60\text{min}$ .

segregate into different particle sizes with heating, the predefined nm-scale Au features remain homogeneous in size, which is key to achieving the desired spherical nanoparticle array. As described previously, the patterned *a*-Si is dissolved in the lithographic Au features, and is converted into a  $\text{SiO}_2$  shell by Au-enhanced oxidation. Upon further thermal treatment, the thermodynamically unstable hemispherical Au nanoparticles are transformed into a stable spherical geometry that minimizes the surface free energy at the Au- $\text{SiO}_2$  interface<sup>52,53</sup>.

To elucidate the evolution of the Au nanoparticle morphology during the Au-enhanced oxidation process, periodic arrays composed of 200nm diameter features having 28nm and 60nm thick *a*-Si and Au layers were defined using top-down fabrication. Separate pieces of the same patterned sample were thermally treated in a 15-in diameter isothermal tube furnace held at  $850^\circ\text{C}$  in 90sccm flow of  $\text{O}_2$  at times of 5min, 30min, 60min and 120min. FESEM images of a single particle within the array following different thermal treatment times are shown in Figure 2-3. Prior to thermal treatment, the *a*-Si and Au layers are well defined with a sharp interface between the

two. The patterned cylindrical features have a sidewall angle of  $\sim 78^\circ$ , which gives an average diameter of 190nm. Sidewall taper is present in features formed by metal lift-off due to the angular spread in the metal flux during evaporation. After the initial 5min thermal treatment, the planar Au layer is transformed into a hemisphere, and approximately 27nm of  $\text{SiO}_2$  is formed by oxidation of the underlying *a*-Si. The transformation is caused by surface atomic migration. Specifically, because the Au atoms along the periphery of the cylindrical feature have fewer neighboring atoms and the surface tension there is also the highest due to the smaller curvature of the radius<sup>54</sup>, the Au atoms migrate away from top edge causing the sharp corner to become rounded. After the initial treatment, the base of the Au segment remains flat and in direct contact with the unoxidized *a*-Si layer. Following the longer 30min anneal, the same hemispherically shaped Au particle is present, but with a thicker 40nm  $\text{SiO}_2$  shell encapsulating the particle. At this point in the process, the *a*-Si layer is fully consumed, and further oxidation is halted. If the sample is left at elevated temperatures for longer times, the high interfacial free energy between the flat base of the Au particle and the fused silica substrates promotes dewetting at the interface<sup>54-58</sup>, thereby causing the hemispherical Au particle to transform into a thermodynamically stable sphere. After the 60min thermal treatment, the initially rough  $\text{SiO}_2$  shell surface becomes smooth because of the  $\text{SiO}_2$  viscous flow near the glass transition temperature. No change in the Au- $\text{SiO}_2$  core-shell nanoparticle size, shape, or array spacing was observed at the longer 120min thermal treatment. This indicates that the stable equilibrium shape of the core-shell particle is achieved after the 60 min thermal treatment. Notably, the sidewall taper and asymmetry present in the starting features is removed by the Au-enhanced oxidation process.

Plasmonic nanoparticle arrays require tight control over the Au nanoparticle dimensions as well as their position on the substrate. Thus, a simple model was derived to determine the relationship between the starting *a*-Si/Au stack properties (diameter and layer thicknesses) and final

spherical Au nanoparticle diameter. From mass conservation, the diameter of the final Au nanoparticle,  $d$ , is related to the starting Au thickness and feature diameter by:

$$d = 2 \times \sqrt[3]{\frac{3 \times t_{Au} d_{Au}^2}{16}} \quad (11)$$

where  $t_{Au}$  is the thickness and  $d_{Au}$  is the average diameter of the evaporated Au feature. Similarly, the SiO<sub>2</sub> shell thickness,  $t_{SiO_2}$ , can also be determined from the starting diameter and thickness of the  $\alpha$ -Si feature. Figure 2-3 (d) shows that the Au particle is located in the center of the core-shell particle, and the final SiO<sub>2</sub> feature can be approximated as a hemisphere plus a cylinder. Substrate clamping prevents growth in the radial direction. Thus, the 44% volume expansion only occurs in the axial direction. Under these assumptions, the SiO<sub>2</sub> shell thickness can be related to the final Au nanoparticle and the starting  $\alpha$ -Si feature dimensions by:

$$\frac{2}{3} \pi \left( t_{SiO_2} + \frac{d}{2} \right)^3 + \pi r \left( t_{SiO_2} + \frac{d}{2} \right)^2 - \frac{4}{3} \pi \left( \frac{d}{2} \right)^3 = 2.25 \pi \left( \frac{d_{Si}}{2} \right)^2 t_{Si} \quad (12)$$

where  $t_{Si}$  is the thickness and  $d_{Si}$  is the average diameter of the evaporated  $\alpha$ -Si feature.

Figure 2-3 (a) and (d) shows that a 136nm diameter spherical Au particle encapsulated within a 35nm thick SiO<sub>2</sub> shell is formed following Au-enhanced oxidation of a 190nm average diameter feature composed of a stack of  $\alpha$ -Si and Au layers that are 28nm and 60nm thick, respectively. The measured Au particle diameter of 136nm closely matches the theoretical prediction of 140nm, and the measured SiO<sub>2</sub> shell thickness of 26nm is also close to the theoretical prediction of 22nm, thereby confirming that the dimensions of the spherical particles are controlled by the tight tolerances that can be achieved by the top-down fabrication processes.

## 2.6 Periodic Spherical Au Nanoparticle Array

Simulation results show that nearly identical optical spectra are expected for both cylindrical and spherical periodic Au nanoparticle arrays at normal incidence. Therefore, a periodic array of spherical Au nanoparticles with same interparticle spacing was fabricated using the Au-enhanced oxidation process. This control sample was used to verify that this new process can be used to create uniform arrays of Au nanoparticles with high optical quality (low loss). Figure 2-4 shows FESEM images of the completed arrays with Au nanoparticle diameter of  $135\text{nm} \pm 2\text{nm}$  and interparticle spacing of  $360\text{nm} \pm 4\text{nm}$ .

The transmission spectrum of the fabricated periodic spherical Au nanoparticle array measured using unpolarized light at normal incidence is superimposed on the simulated spectra computed using thin-film Au and JC Au properties in Figure 2-5. The spherical nanoparticle array has a transmission spectrum with an asymmetric Fano-like shape. The two resonances at 630nm and 550nm correspond to the coupled plasmonic dipolar and quadrupolar modes of the Au nanoparticles, respectively<sup>59</sup>. The transmission maximum at 530nm corresponds to the cut-off wavelength where the first-order diffraction mode changes from evanescent to propagating<sup>60</sup>, given by:

$$\lambda_{(i,j)} = \frac{d \times n}{(i^2 + j^2)^{1/2}} \quad (13)$$

where  $n$  is the refractive index of the dielectric environment,  $d$  is the grating constant, and  $(i,j)$  denotes the diffraction order of the grating. In contrast to the periodic cylindrical nanoparticle arrays in Figure 2-1(d), the spherical arrays had a single dipole plasmonic peak near 630nm with a FWHM of 53.8nm. This confirms the isotropic optical properties of the spherical Au nanoparticles formed by the Au enhanced oxidation process. The results in Figure 2-5 (a) show that the measured transmission spectrum is in strong agreement with the spectrum simulated using the bulk JC Au

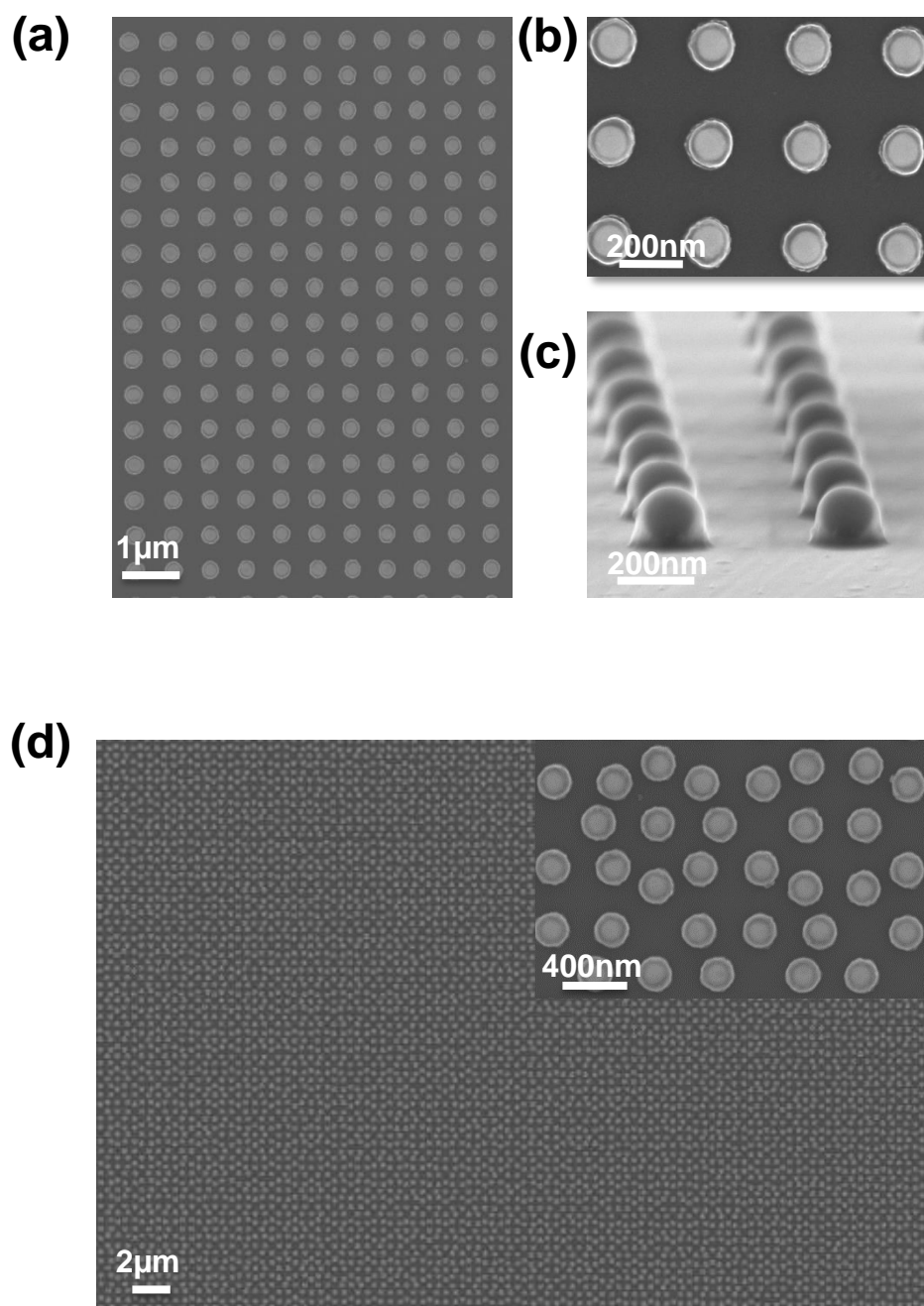


Figure 2-4. (a) FESEM image of fabricated periodic arrays with spherical Au nanoparticles that are 135 nm in diameter and have an interparticle spacing of 360 nm; (b) top view and (c) cross sectional view of the array; (d) FESEM image of the fabricated spherical Ammann-Beenker nanoparticle arrays of 135 nm in diameter and 392 nm prototile side length; Inset: Enlarged view of the Ammann-Beenker array.

model. This demonstrates that the Au-enhanced oxidation process converts the initially polycrystalline Au cylinders into crystalline Au spheres with lower optical loss, which provides advantages for plasmonic devices.

The plasmonic scattering response of the arrays was further confirmed by collecting dark-field scattering maps using an upright microscope (Nikon TE 200U). The array was covered with index matching oil and illuminated with unpolarized white light from tungsten-halogen lamp using a dark-field condenser (NA=1.2-1.43) in transmission mode. The light scattered from the arrays was collected with a 100× objective lens and imaged with a digital CCD camera. Figure 2-5 (b) shows the scattered light images for the periodic arrays, which exhibit a uniform red color that agrees with the resonance wavelength of transmission spectrum.

To understand the origin of the resonance, a rigorous theoretical diffraction analysis from Meier *et al.*<sup>60</sup> was used to analyze the transmission spectra of the periodic arrays (and later extended to analyze the quasicrystal arrays). According to this theory, critical grating constants can be assigned to each diffraction mode for a periodic lattice with lattice constant  $\Delta$ .<sup>60</sup>

$$\Delta_{C,m} = \frac{m\lambda_0}{\sqrt{\epsilon_m}} \quad (14)$$

At a given wavelength ( $\lambda_0$ ), for lattice constants  $\Delta \leq \Delta_{C,m}$ , the  $m$ -th diffraction mode is evanescent, and for  $\Delta \geq \Delta_{C,m}$  it is propagating<sup>61</sup>. At the boundary where  $\Delta = \Delta_{C,m}$ , the diffraction order becomes radiating, and it only radiates in the plane of the array (at the grazing angle). This is of particular importance when the critical grating constant coincides with the localized surface plasmon wavelength of the Au nanoparticles. When this occurs, the plasmonic fields radiate at the grazing angle in the plane of the array, causing stronger coupling between particles. This leads to a redshift of the localized surface plasmon resonance wavelength<sup>60</sup>. The result is the excitation of

very sharp, so-called “hybrid photonic-plasmonic resonances”<sup>19</sup> which were experimentally confirmed by Félidj *et al.*<sup>38</sup>.

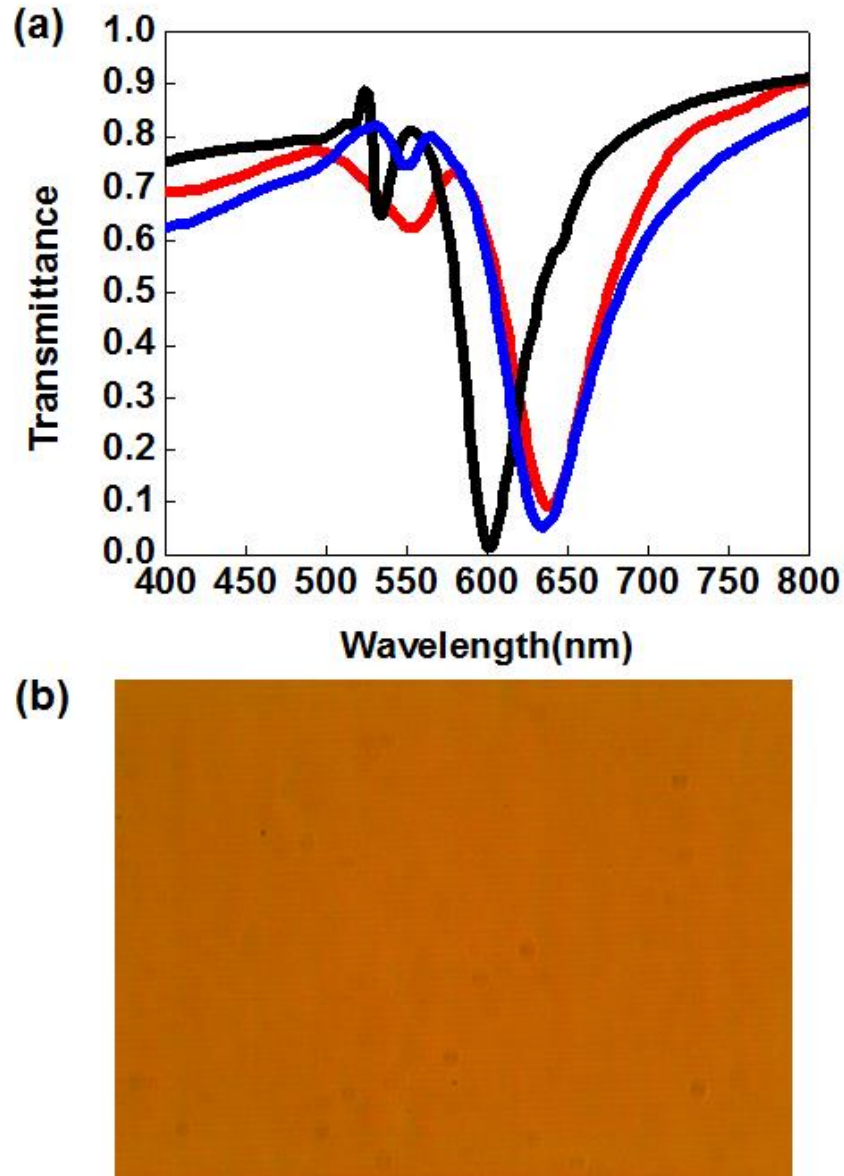


Figure 2-5. (a) Measured (red) and simulated (blue and black) transmission spectra of periodic arrays with spherical Au nanoparticles that are 135nm in diameter and interparticle spacing of 360nm; Blue: crystalline JC Au property; Black: measured Au property ; (b) Far-field scattering map of the periodic spherical arrays, which have a uniform red color.

For periodic arrays, only the first grating mode can be coupled with localized surface plasmon waves. Higher-order modes cannot form hybrid photonic-plasmonic resonances because the resonance wavelength changes by a factor of two, where the nanoparticles can no longer support a localized surface plasmon. The periodic array studied in this work was designed such that the first-order, in-plane photonic resonance wavelength (540nm) is near the localized surface plasmon (LSP) of the Au nanoparticle (560nm). Therefore, a hybrid plasmonic-photonic mode is excited in the sample plane. This hybrid mode enhances the optical resonance and causes a red-shift<sup>16</sup> in the resonance wavelength to 630nm as compared to the LSP of individual Au nanoparticles.

## 2.7 Ammann-Beenker Spherical Au Nanoparticle Array

The Ammann-Beenker plasmonic quasicrystal presented in Section 2.7 was fabricated using the Au-enhanced oxidation process to create a structure with spherical Au nanoparticles rather than cylindrical particles. Figure 2-4 shows FESEM images of the fabricated array. These images confirm that the average diameter of fabricated Au nanoparticles is  $135\text{nm} \pm 2\text{nm}$ . The mean of the minimum interparticle spacing  $d_{\min}$  is  $300\text{nm} \pm 4\text{nm}$ , which is related to the prototile side length  $a$  by  $d_{\min} = 2a \cos(3\pi/8)$ . The designed prototile side length of  $a = 392\text{nm}$  gives a minimum interparticle spacing of 300nm, which closely matches the fabricated structure.

The transmission spectrum measured using unpolarized light at normal incidence is plotted together with the simulated spectrum in Figure 2-6 (a). Based on the results from the periodic array, the bulk JC Au property values were used in this simulation. In contrast to the top-down fabricated cylindrical Ammann-Beenker array, the measured optical properties of this structure made using the new Au-enhanced oxidation were in strong agreement with theory. In particular, both the resonance wavelengths and intensities matched the simulated values. These results indicate that the optical properties of quasicrystal arrays are more sensitive to the specific geometry of the Au



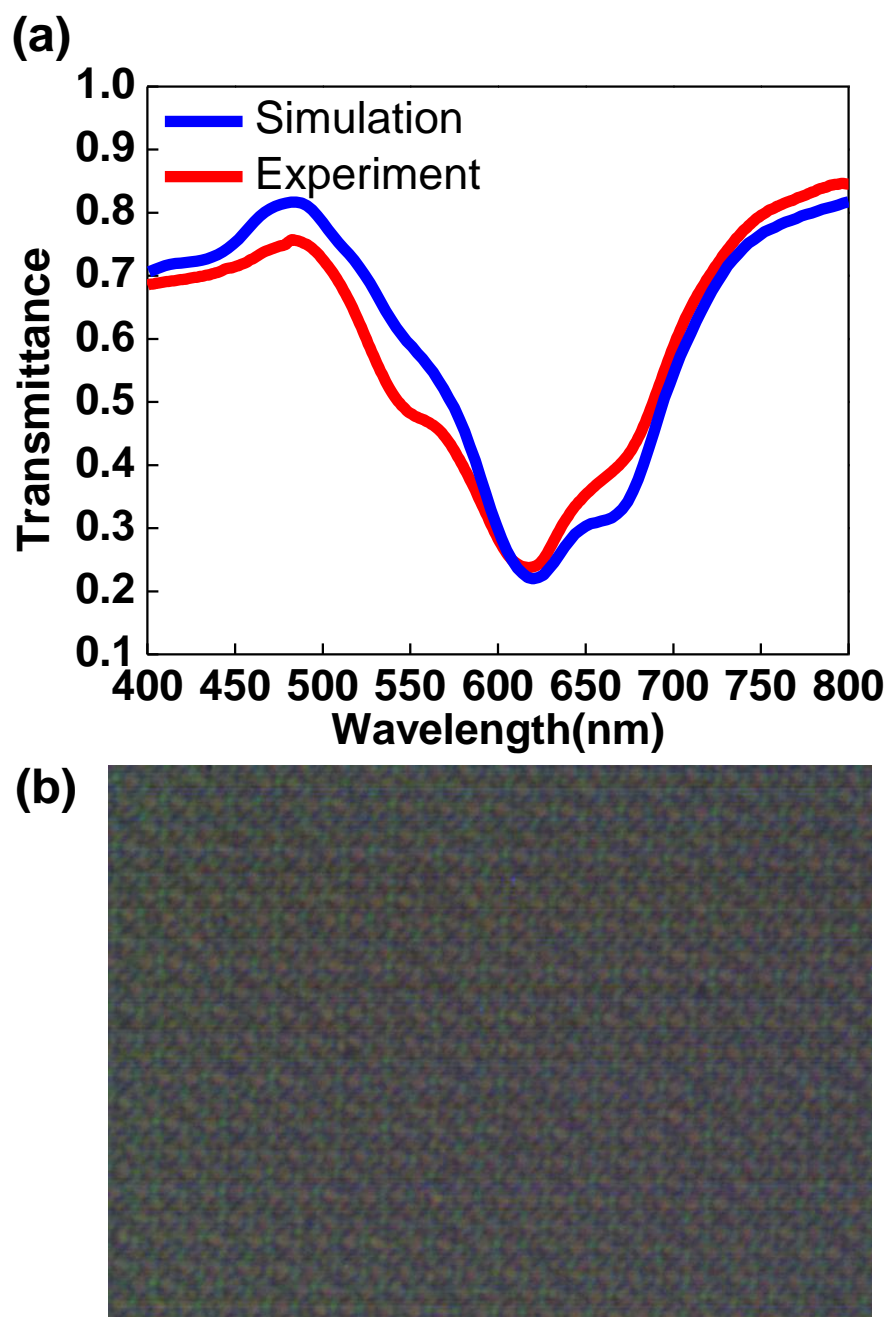


Figure 2-6. (a) Measured (red) and simulated (blue) transmission spectra of Ammann-Beenker spherical Au nanoparticle arrays with 135nm diameter and 392nm prototile side length. The simulation was performed using the bulk JC Au properties and spherical nanoparticle shape; (b) Far-field scattering map of the Ammann-Beenker spherical Au nanoparticle arrays, which show an inhomogeneous light distribution.

nanoparticles than the periodic arrays. This may be due to the fact that multiple photonic modes in quasicrystals can interact with the single plasmonic peak, leading to stronger interactions compared to the periodic case where only the first photonic mode interacts with the plasmonic mode. The hybrid plasmonic-photonic concept introduced in Section 2.6 can be used to explain the origin of the features in the transmission spectrum. The Fourier diffraction pattern can be used to identify the multiple photonic modes and relate them to the real space distances in the array. The intense peaks in the diffraction pattern of quasicrystal arrays are associated with vectors in reciprocal space<sup>23,42,62</sup>. It has been shown that if these reciprocal vectors are indexed according to their magnitude, they can be directly associated with real-space distances in the quasicrystals<sup>23,63</sup>. Specifically, the reciprocal vectors are inversely proportional to half of the specific distances in the structure. Unlike their periodic counterparts, reciprocal vectors for quasicrystals fill the entire reciprocal space, and thus it is not possible to define a basis set of primitive reciprocal vectors. However, a pseudo basis set can be constructed by omitting the spot intensities below a predefined threshold value<sup>64</sup>.

Figure 2-7(a) shows the normalized Fourier diffraction pattern (logarithmic scale) of an Ammann-Beenker array generated from a tiling with a prototile side length of  $a$ . Three corresponding real space distance are marked in Figure 2-7(b), denoted by  $d_1$ ,  $d_2$  and  $d_3$ . These real space distances are indexed according to their length  $d_1 > d_2 > d_3$  with  $d_1$  corresponding to the distance between two adjacent square prototiles,  $d_2$  corresponding to the diagonals of the rhombus prototiles, and  $d_3$  corresponding to diagonals of the square prototiles, respectively. These corresponding real space distances can be expressed with respect to the prototile side length  $a$  by:

$$\begin{aligned} d_1 &= a\sqrt{2(2+\sqrt{2})} \\ d_2 &= a\sqrt{2+\sqrt{2}} \\ d_3 &= a\sqrt{2} \end{aligned} \tag{15}$$

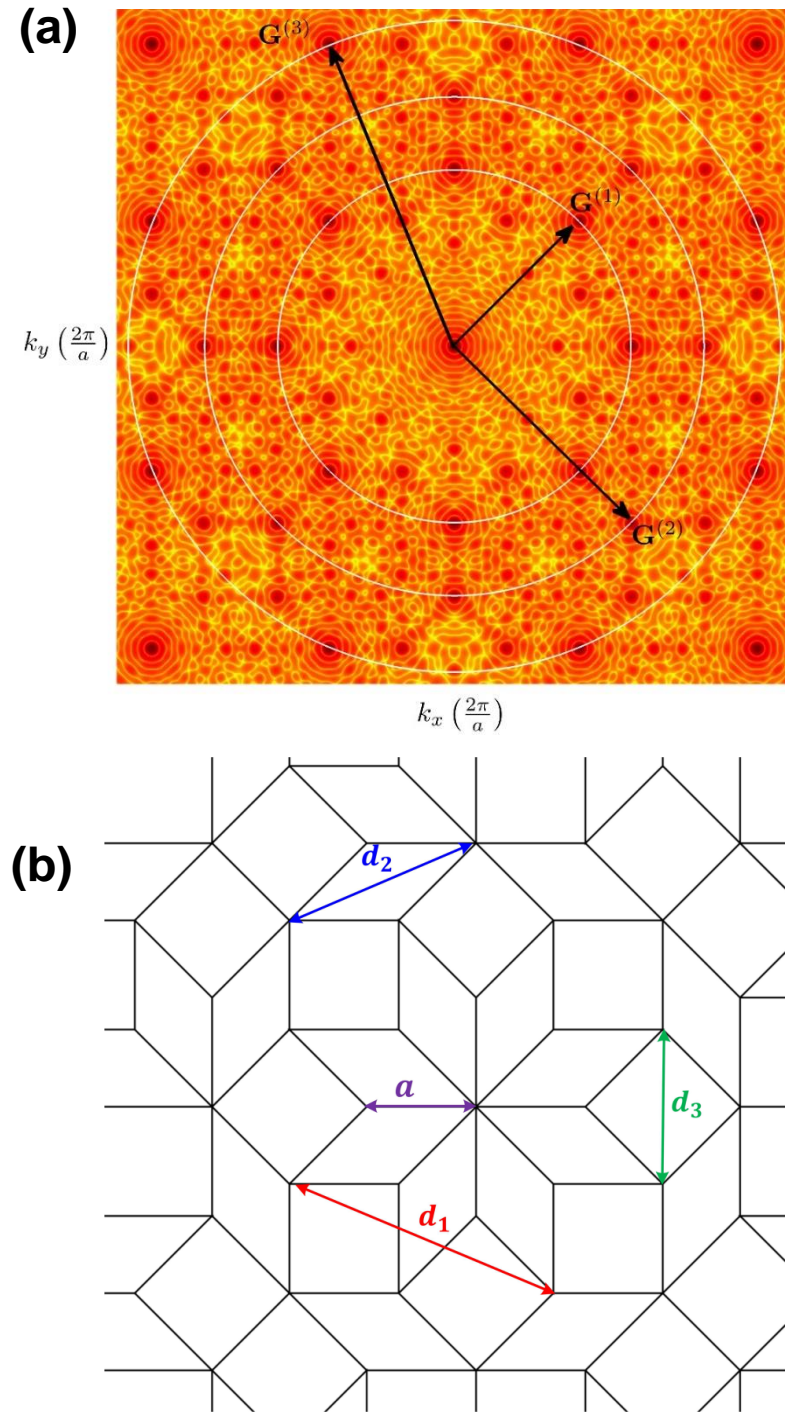


Figure 2-7. (a) Fourier transform image of the Ammann-Beenker arrays (log scale); (b) The corresponding real space distances are marked in the Ammann-Beenker array,  $a$  is the prototile side length of the tiling,  $d_1$  is the distance between two adjacent square prototiles,  $d_2$  is the diagonal of the rhombus prototile and  $d_3$  is the diagonal of the square prototile.

The three circles drawn in Figure 2-7(a) have radii of  $2/d_1$ ,  $2/d_2$ , and  $2/d_3$ , and they coincide with the first three Bragg resonances of the Ammann-Beenker lattices labeled as  $\mathbf{G}^{(1)}$ ,  $\mathbf{G}^{(2)}$  and  $\mathbf{G}^{(3)}$  reciprocal lattice vectors.

Because the surrounding medium for the spherical Au nanoparticles is  $\text{SiO}_2$ , which has a relative dielectric constant of  $\epsilon_m = 2.16$ , the corresponding free-space wavelengths for the first three photonic resonances are:

$$\begin{aligned}\lambda_1 &= \frac{d_1}{2} \sqrt{2.16} = 753 \text{ nm} \\ \lambda_2 &= \frac{d_2}{2} \sqrt{2.16} = 532 \text{ nm} \\ \lambda_3 &= \frac{d_3}{2} \sqrt{2.16} = 407 \text{ nm}\end{aligned}\tag{16}$$

The primary resonance in the transmission spectrum of the Ammann-Beenker quasicrystal shown in Figure 2-6 (a) has a center wavelength of 618nm. This is caused by the interaction of the photonic mode at  $\lambda_2$  with the plasmonic mode, which shifts the plasmonic resonance at 560nm to a wavelength longer than  $\lambda_2$ . The broadband response is induced by hybrid plasmonic-photonic modes, and can be explained from the diffraction pattern of the Ammann-Beenker quasicrystal. Although only the reciprocal vectors with the highest intensity were considered in the preceding analysis, the reciprocal vectors of quasicrystals densely fill the entire reciprocal space<sup>65</sup>. Figure 2-8 shows an enlarged image of the first quadrant of the diffraction pattern of the Ammann-Beenker structures with the reciprocal vectors  $\mathbf{G}^{(1)}$  and  $\mathbf{G}^{(2)}$  marked. The region between  $\mathbf{G}^{(1)}$  and  $\mathbf{G}^{(2)}$  is densely filled with distinct areas of high intensity. Because the corresponding real-space distance of these spots fall between  $d_1$  and  $d_2$ , the photonic modes that correspond to these reciprocal vectors are in the wavelength range between  $\lambda_1$  and  $\lambda_2$ . Therefore, all of these photonic modes couple to the surface plasmon modes, and collectively form hybrid photonic-plasmonic resonances. This also led to formation of the satellite resonance centered at 668nm. The numerous photonic modes between  $\mathbf{G}^{(2)}$  and  $\mathbf{G}^{(3)}$  are responsible for the satellite resonance centered at 551nm. The interaction between

the photonic mode at  $\lambda_3$  and the plasmonic mode results in a weak hybrid plasmonic-photonic resonance at 520nm. The hybrid mode caused by  $\lambda_3$ , the two satellite resonances at 551nm and 668nm, and the hybrid modes resulting from photonic modes between  $\mathbf{G}^{(1)}$  and  $\mathbf{G}^{(2)}$ ,  $\mathbf{G}^{(2)}$  and  $\mathbf{G}^{(3)}$  merge together with the primary resonance to create the broadband optical response.

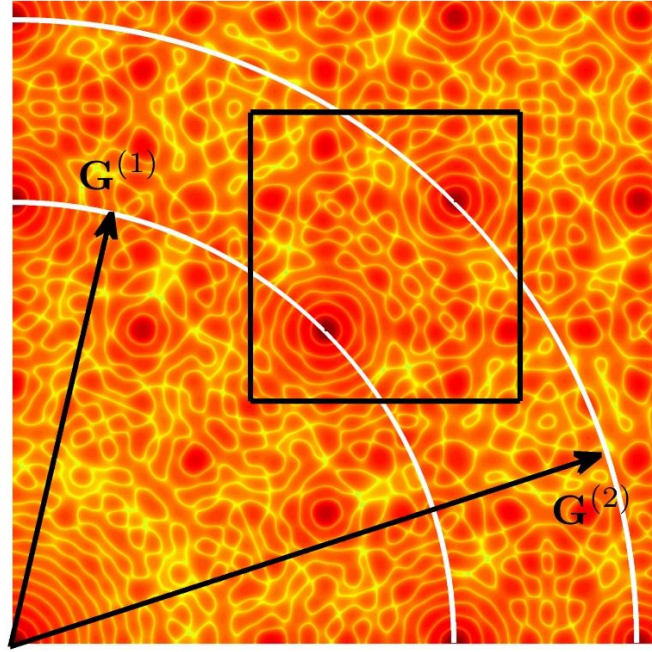


Figure 2-8. Enlarged view of the Fourier transform image of the Ammann-Beenker arrays between the first and second circles (log scale).

The scattering map of fabricated Ammann-Beenker plasmonic array was collected using the method described in Section 2.6, and is shown in Figure 2-6 (b). The map exhibits an inhomogeneous spatial light distribution of different light components. The green, orange and red colors in the scattering maps agree with the measured broadband transmission spectrum, which had a broadband response from 500nm to 700nm. The inhomogeneous light distribution results from the different plasmonic interactions that the nanoparticles experience with their neighbors. Because

the resonance wavelengths depend on these interactions, different colors appear at different locations in the fabricated array.

## 2.8 Penrose Spherical Au Nanoparticle Array

A second common quasicrystal is based on a Penrose tiling, which was introduced by Penrose<sup>44,66</sup> in the 1970s. Figure 2-9(a) shows an example of a Penrose array that is constructed from narrow (vertex angles  $\pi/5$  and  $4\pi/5$ ) and wide (vertex angles  $2\pi/5$  and  $3\pi/5$ ) rhombohedral prototiles with equal side length  $s$ . Penrose plasmonic arrays are created by positioning Au nanoparticles at the vertices of the arrays, as illustrated in Figure 2-9 (b). The Penrose tiling exhibits local five-fold symmetry in real space, whereas the structure factor reveals ten-fold rotational symmetry. In the Penrose tiling, the ratio between different lattice reciprocal vectors are related by the golden ratio<sup>20</sup>  $\tau = (1 + \sqrt{5}) / 2$ . In contrast to broadband Ammann-Beenker quasicrystals, Penrose structures can produce very sharp diffraction peaks<sup>67</sup> because the well-separated photonic modes can interact independently with the plasmonic mode. This results in a multiband optical response.

The Penrose array fabricated in this thesis research is composed of individual spherical Au nanoparticles that are 135nm in diameter with a prototile side length of 485nm. This ensures coupling between the multiple photonic modes and the broad plasmonic mode. The Penrose quasicrystal arrays were fabricated using the Au enhanced oxidation process described in Section 2.5 to create a structure with spherical Au nanoparticles. Figure 2-9 (d) shows the FESEM images of the fabricated array, confirming that the average diameter of fabricated Au nanoparticle is 135nm  $\pm$  2nm. The mean of minimum interparticle spacing  $d_{\min}$  is 300nm  $\pm$  4nm, where  $d_{\min} = s / \tau$ . The

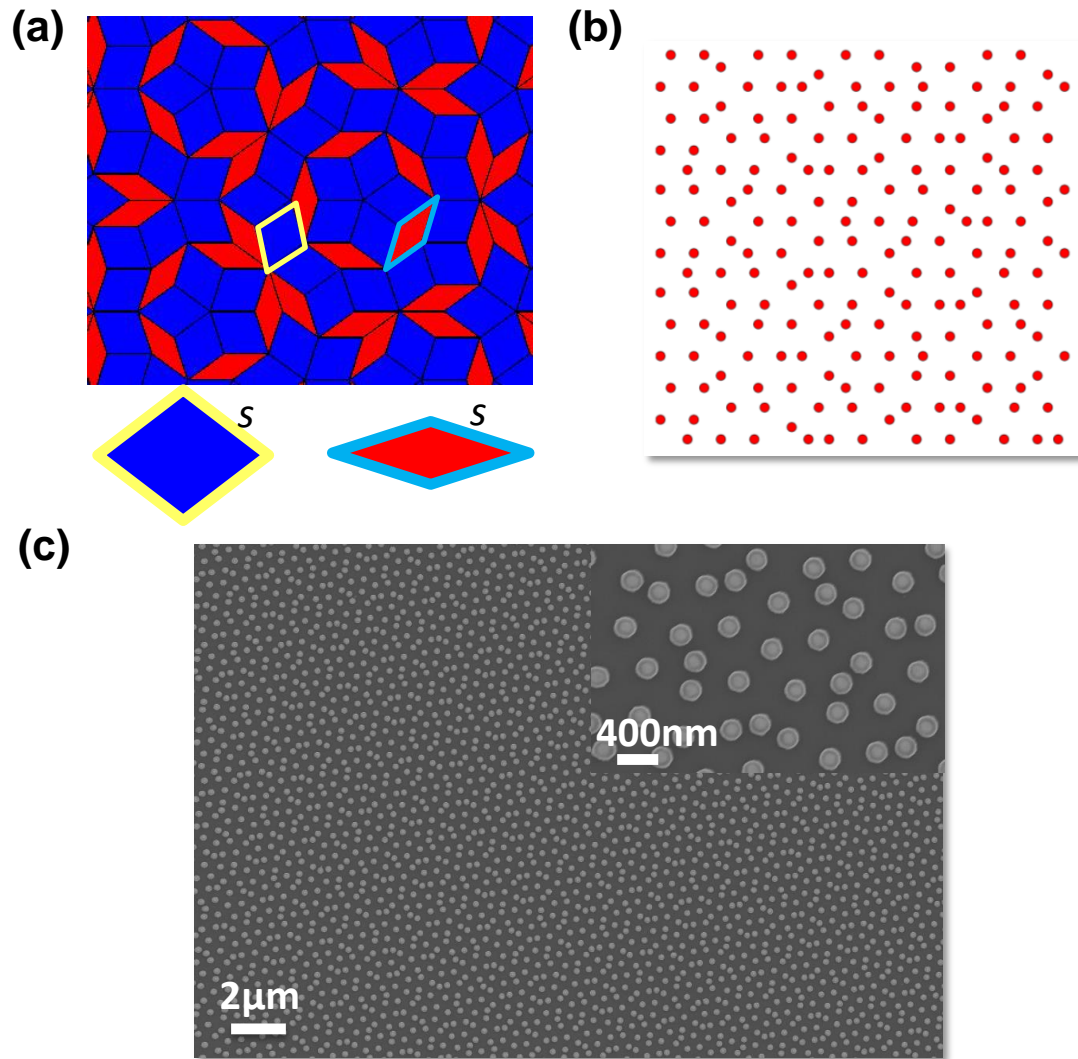


Figure 2-9. (a) The quasicrystal Penrose tiling that highlights two rhombohedral prototiles in yellow and blue; (b) The designed Penrose nanoparticle arrays with prototile side length  $s$  of 485 nm; (c) FESEM image of the fabricated Penrose quasicrystal arrays with spherical Au nanoparticles that are 135 nm in diameter; Inset: Enlarged view of the Penrose array.

designed prototile side length of  $s = 485$  nm gives a minimum interparticle spacing of 300 nm, which closely matches the fabricated structure.

The measured transmission spectrum for unpolarized light at normal incidence is plotted together with simulated spectrum in Figure 2-10 (a). Based on the results from the periodic array



fabricated using the same process, the bulk JC Au property values were used in this simulation. The measured curves recovered all the spectral features of the simulated curves, including the resonances at 535nm, 638nm and 730nm. In addition to the agreement in the resonance positions, the intensity and bandwidth also agreed well with simulation.

Figure 2-11 shows the normalized Fourier diffraction pattern (logarithmic scale) of a Penrose quasicrystal generated from a tiling with a tile side length of  $s$ . The three corresponding real space distances, denoted by  $d_1$ ,  $d_2$  and  $d_3$ , are included in the figure. These corresponding real space distances were indexed according to their length  $d_1 > d_2 > d_3$ , with  $d_1$  corresponding to the long diagonal of the narrow rhombus prototile, and  $d_2$  and  $d_3$  corresponding to the long and short diagonals of the wide rhombus prototile, respectively. Applying the golden-ratio relation between the lattice constants and tile side  $s$ , gives:

$$\begin{aligned} d_1 &= s\sqrt{4-\tau^{-2}} \\ d_2 &= s\tau \\ d_3 &= s\sqrt{2-\tau^{-1}} \end{aligned} \tag{17}$$

and,

$$d_1 : d_2 : d_3 \approx 1 : 0.86 : 0.62 \tag{18}$$

The three circles superimposed on Figure 2-11 (a) have radii of  $2/d_1$ ,  $2/d_2$ , and  $2/d_3$ , which coincide with the first three Bragg diffraction peaks of the Penrose quasicrystal labeled as  $\mathbf{G}^{(1)}$ ,  $\mathbf{G}^{(2)}$  and  $\mathbf{G}^{(3)}$ . Prior work has shown that a pseudo-basis can be constructed from the internal series of reciprocal vectors with the same length as  $\mathbf{G}^{(1)}$ <sup>42</sup>. Because the diffraction pattern of the Penrose quasicrystal possesses 5-fold rotational symmetry, a pseudo-basis set of five vectors  $\mathbf{F}_1, \mathbf{F}_2 \dots \mathbf{F}_5$  can be defined as:

$$\mathbf{F}_i = \frac{2}{d_1} \left( \cos \frac{(i-1)\pi}{5}, \sin \frac{(i-1)\pi}{5} \right) \quad i = 1, 2, \dots, 5 \tag{19}$$



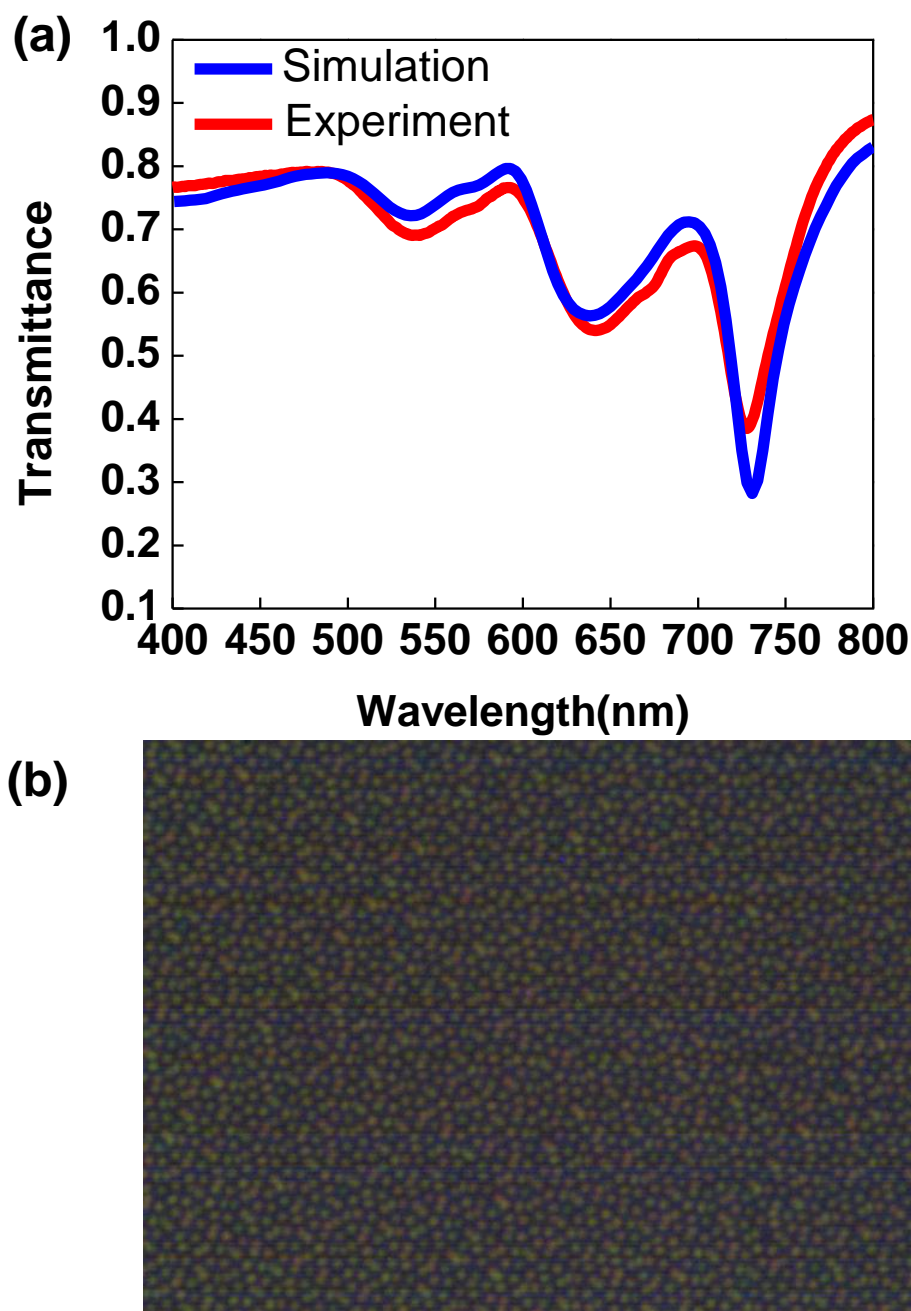


Figure 2-10. (a) Measured (red) and simulated (blue) transmission spectra of Penrose quasicrystals with spherical Au nanoparticle that are 135nm in diameter and a prototile side length of 485nm; the simulation was performed using the bulk Au properties and a spherical nanoparticle shape; (b) Far-field scattering map of the fabricated Penrose arrays shows an inhomogeneous light distribution dominated by three colors.

As noted in Section 2.7, the reciprocal vectors of quasicrystals densely fill the entire reciprocal space, preventing a primitive basis set as in periodic lattices. Subjecting the reciprocal space to a threshold, the basis set in Eq. (19) can be used to construct the reciprocal space<sup>64</sup>. For example,  $\mathbf{G}^{(2)}$  in Figure 2-11(a) can be expressed as  $\mathbf{G}^{(2)} = [0, -1, 0, 0, -1]$ , where the vector notation is given by:

$$[a_1, a_2, a_3, a_4, a_5] \equiv a_1 \mathbf{F}_1 + a_2 \mathbf{F}_2 + a_3 \mathbf{F}_3 + a_4 \mathbf{F}_4 + a_5 \mathbf{F}_5 \quad (20)$$

Similarly,  $\mathbf{G}^{(3)}$  shown in Figure 2-11 (a) can be expressed as  $\mathbf{G}^{(3)} = [-1, 0, -1, 0, 0]$ . This shows that:

$$|\mathbf{G}^{(3)}| : |\mathbf{G}^{(2)}| : |\mathbf{G}^{(1)}| = \frac{2}{d_3} : \frac{2}{d_2} : \frac{2}{d_1} \quad (21)$$

which further confirms the relationship between Bragg peaks and lattice constants. Associating the Bragg peaks in the diffraction pattern with real space distances in the quasicrystal allows the photonic resonances to be determined. The corresponding values for  $d_1/2$ ,  $d_2/2$ , and  $d_3/2$  are:

$$\begin{aligned} \frac{d_1}{2} &= \frac{s}{2} \sqrt{4 - \tau^{-2}} \approx 460 \text{ nm} \\ \frac{d_2}{2} &= \frac{s\tau}{2} \approx 391 \text{ nm} \\ \frac{d_3}{2} &= \frac{s\sqrt{2 - \tau^{-1}}}{2} \approx 284 \text{ nm} \end{aligned} \quad (22)$$

Accounting for the relative dielectric constant of the surrounding  $\text{SiO}_2$  medium, the corresponding free-space wavelengths for the first three photonic resonances are:

$$\begin{aligned} \lambda_1 &= n \frac{d_1}{2} = 676 \text{ nm} \\ \lambda_2 &= n \frac{d_2}{2} = 575 \text{ nm} \\ \lambda_3 &= n \frac{d_3}{2} = 418 \text{ nm} \end{aligned} \quad (23)$$

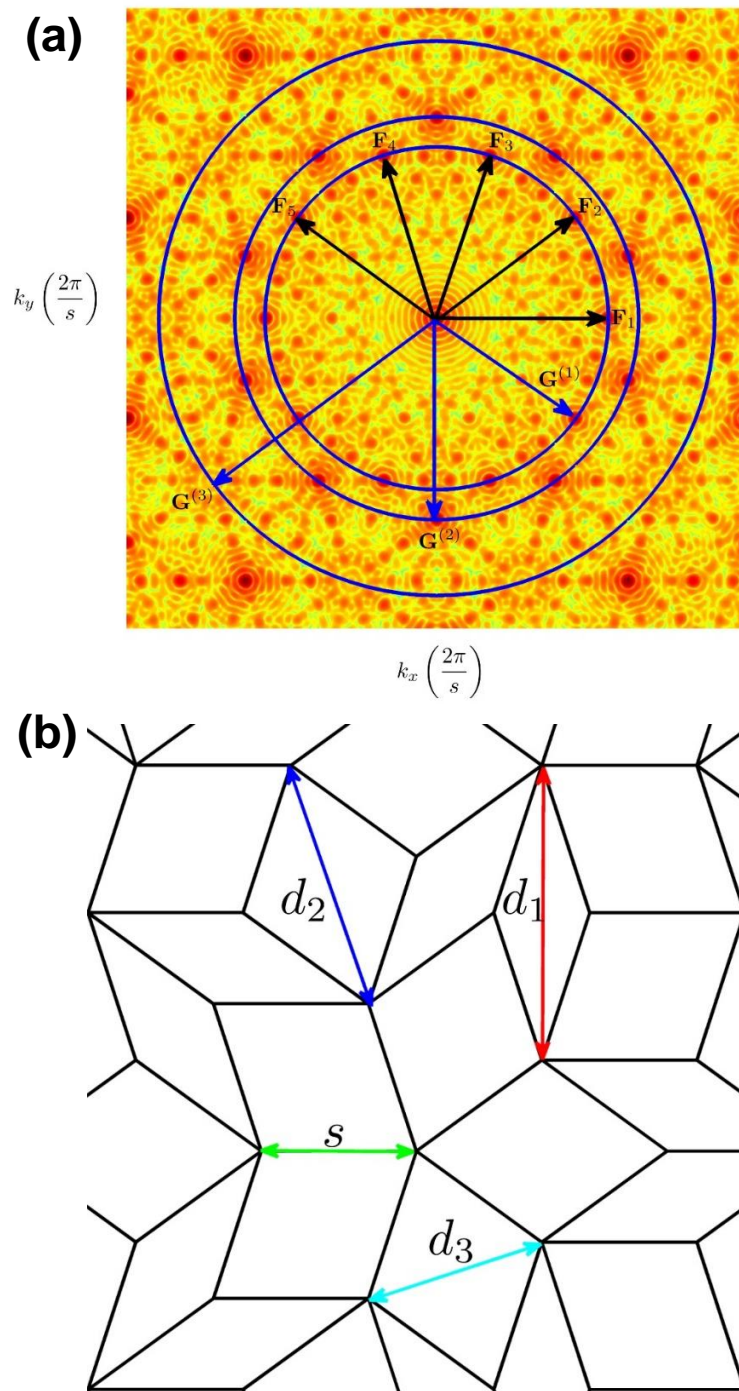


Figure 2-11. (a) The Fourier transform image of the Penrose array (log scale); (b) The corresponding real space distances are marked in the Penrose arrays, where  $s$  is the prototile side length,  $d_1$  is the diagonal of the narrower rhombus prototile,  $d_2$  is long diagonal of the wide rhombus prototile and  $d_3$  is short diagonal of the wide rhombus prototile.

In contrast to the broadband Ammann-Beenker quasicrystal, the transmission spectra of the Penrose nanoparticle array shown Figure 2-10 (a) exhibits three distinct and well-separated resonances at approximately 730nm, 630nm and 520nm. This is caused by that the discrete nature of the photonic modes as there are not many local maxima among  $\mathbf{G}^{(1)}$ ,  $\mathbf{G}^{(2)}$  and  $\mathbf{G}^{(3)}$ . In addition, the ratio of these resonances in the transmission spectra is approximately 1: 0.86: 0.7, which is consistent with the ratio of  $d_1$ :  $d_2$ :  $d_3$  given in Eq (18). The measured resonance wavelengths are higher than the corresponding  $\lambda_1$ ,  $\lambda_2$  and  $\lambda_3$  determined from Eq (23). This is expected because the maximum transmission occurs on the longer wavelength side of each resonant band<sup>23</sup> as the coupling between the plasmonic and photonic modes reduces the energy needed for resonance.

In the case of the periodic lattice, only the first photonic resonance mode is coupled to the surface plasmon resonance. This is due to the fact that different grating orders are separated by large intervals, and thus only one grating order is in the plasmonic resonance of the nanoparticle. In quasicrystals, multiple photonic modes can be positioned within the plasmonic resonance regime. The results in Eq (23) for the structure studied in this work show that the first three photonic modes are in much closer proximity to one another than the first three photonic resonances of a periodic lattice. This property results in the formation of multiple hybrid photonic-plasmonic resonances. In the Penrose quasicrystal, the two resonances at 730nm and 630nm are both hybrid plasmonic-photonic modes.

The scattering map of the nanofabricated Penrose quasicrystal was collected using the method described in Section 2.6, and shown in Figure 2-10 (b). In this case, the map shows an inhomogeneous spatial light distribution with three dominate red, green and orange colors. The individual nanoparticles are visible because their scattering cross is much larger than their physical dimension owing to the long-range plasmonic interaction, which can be more than a million times larger than that for absorption or emission<sup>68</sup>. Because each nanoparticle in the Penrose quasicrystal can experience different plasmonic interactions with its neighbors, and its resonance wavelength

(thus color of scattering light) is dependent on this interaction, different colors appear at different locations in the structure. The color difference can be distinguished for each nanoparticle as the three hybrid resonances are distinct and well separated in the Penrose array.

## 2.9 Summary

In summary, quasicrystal nanoparticle arrays that possess enhanced scattering and broadband optical properties were investigated. A modified GMT modeling approach was used to quantitatively compare the transmission spectra obtained from simulation and experiment. Ammann-Beenker quasicrystal nanoparticle arrays were first fabricated using a conventional electron-beam lithography patterning and metal lift-off process. This resulted in cylindrical Au nanoparticles, which were not consistent with the spherical Au nanoparticle shape used in the simulation. Discrepancies in the resonance position, intensity, and bandwidth were observed between the measured and simulated spectra. To investigate the origin of this difference, periodic arrays of cylindrical Au nanoparticles were fabricated using the same procedure. By incorporating the fabrication imperfections, the polycrystalline nature of measured thin-film properties, and the cylindrical-shape nanoparticle with measured Au properties into the simulation, strong agreement between simulation and experiment was obtained. This suggested that the discrepancy observed in the transmission spectra of the quasicrystal was mainly caused by the difference in the nanoparticle geometry.

To bridge the gap between simulation and experiment, a new Au-enhanced oxidation fabrication process was developed to form spherical Au nanoparticle arrays. This technique combined the merits of lithographic patterning with laser heating, and enabled control of individual sphere placement, diameter and spacing down to the nanometer scale. In this process, the cylindrical Au particles defined by a conventional top-down process were transformed into

spheres during a high-temperature thermal treatment in O<sub>2</sub>. The final spherical Au nanoparticle diameter and particle spacing were determined entirely by the starting lithographic pattern and the evaporated Au volume. Periodic arrays together with Ammann-Beenker and Penrose quasicrystals were fabricated using the Au-enhanced oxidation process. Strong agreement was found between the transmission spectrum generated using the modified GMT simulation method and experimentally measured results. The inhomogeneous light distribution in the Ammann-Beenker and Penrose arrays, compared to the red color for periodic arrays in the far-field scattering map, confirmed the broadband and multiband behavior of the corresponding quasicrystal Au nanoparticle arrays. The transmission properties of the quasicrystals were also studied by understanding the interaction of the photonic and plasmonic resonances of the Au nanoparticles and arrays, and the dominant spectral features were associated with a specific particle spacing in the array. These results provide guidance for designing quasicrystals with customized broadband or multiband properties.

## 2.10 References

- 1 Yanik, A. A. *et al.* Seeing protein monolayers with naked eye through plasmonic Fano resonances. *P Natl Acad Sci USA* **108**, 11784-11789 (2011).
- 2 Liu, N., Mesch, M., Weiss, T., Hentschel, M. & Giessen, H. Infrared Perfect Absorber and Its Application As Plasmonic Sensor. *Nano Lett* **10**, 2342-2348 (2010).
- 3 Kadakia, N. Nanoparticle Scattering, Absorption, and Interface Effects for Surface Plasmon Enhanced Thin Silicon Solar Cells: Theory, Past Findings, and Future Directions. *Handbook of Research on Solar Energy Systems and Technologies*, 210-230 (2013).
- 4 Beck, F. J., Mokkaṡati, S. & Catchpole, K. R. Plasmonic light-trapping for Si solar cells using self-assembled, Ag nanoparticles. *Prog Photovoltaics* **18**, 500-504 (2010).
- 5 Wang, E. C., Mokkaṡati, S., Soderstrom, T., Varlamov, S. & Catchpole, K. R. Effect of Nanoparticle Size Distribution on the Performance of Plasmonic Thin-Film Solar Cells: Monodisperse Versus Multidisperse Arrays. *Ieee J Photovolt* **3**, 267-270 (2013).
- 6 Bauer, C. & Giessen, H. Light harvesting enhancement in solar cells with quasicrystalline plasmonic structures. *Opt Express* **21**, A363-A371 (2013).
- 7 Nakayama, K., Tanabe, K. & Atwater, H. A. Plasmonic nanoparticle enhanced light absorption in GaAs solar cells. *Appl Phys Lett* **93** (2008).

- 8 Pryce, I. M., Koleske, D. D., Fischer, A. J. & Atwater, H. A. Plasmonic nanoparticle enhanced photocurrent in GaN/InGaN/GaN quantum well solar cells. *Appl Phys Lett* **96** (2010).
- 9 Maier, S. A. *et al.* Local detection of electromagnetic energy transport below the diffraction limit in metal nanoparticle plasmon waveguides. *Nat Mater* **2**, 229-232 (2003).
- 10 Maier, S. A., Kik, P. G. & Atwater, H. A. Observation of coupled plasmon-polariton modes in Au nanoparticle chain waveguides of different lengths: Estimation of waveguide loss. *Appl Phys Lett* **81**, 1714-1716 (2002).
- 11 Solis, D., Jr. *et al.* Turning the Corner: Efficient Energy Transfer in Bent Plasmonic Nanoparticle Chain Waveguides. *Nano Lett* (2013).
- 12 de Waele, R., Koenderink, A. F. & Polman, A. Tunable nanoscale localization of energy on plasmon particle arrays. *Nano Lett* **7**, 2004-2008 (2007).
- 13 Dintinger, J., Mühlig, S., Rockstuhl, C. & Scharf, T. A bottom-up approach to fabricate optical metamaterials by self-assembled metallic nanoparticles. *Opt Mater Express* **2**, 269-278 (2012).
- 14 Henzie, J., Lee, M. H. & Odom, T. W. Multiscale patterning of plasmonic metamaterials. *Nat Nanotechnol* **2**, 549-554 (2007).
- 15 Grigorenko, A. N. *et al.* Nanofabricated media with negative permeability at visible frequencies. *Nature* **438**, 335-338 (2005).
- 16 Zou, S. & Schatz, G. C. Narrow plasmonic/photonic extinction and scattering line shapes for one and two dimensional silver nanoparticle arrays. *The Journal of Chemical Physics* **121**, 12606-12612 (2004).
- 17 Shahmansouri, A. & Rashidian, B. Behavior of plasmonic nanoparticle array in near- and far-field coupling regimes for transverse electric and transverse magnetic polarizations. *J Opt Soc Am B* **30**, 2286-2291 (2013).
- 18 Auguie, B. & Barnes, W. L. Collective resonances in gold nanoparticle arrays. *Phys Rev Lett* **101** (2008).
- 19 Gopinath, A., Boriskina, S. V., Feng, N. N., Reinhard, B. M. & Dal Negro, L. Photonic-plasmonic scattering resonances in deterministic aperiodic structures. *Nano Lett* **8**, 2423-2431 (2008).
- 20 Vardeny, Z. V., Nahata, A. & Agrawal, A. Optics of photonic quasicrystals. *Nat Photonics* **7**, 177-187 (2013).
- 21 Bauer, C., Kobiela, G. & Giessen, H. 2D quasiperiodic plasmonic crystals. *Sci Rep-Uk* **2** (2012).
- 22 Gopinath, A., Boriskina, S. V., Reinhard, B. M. & Dal Negro, L. Deterministic aperiodic arrays of metal nanoparticles for surface-enhanced Raman scattering (SERS). *Opt Express* **17**, 3741-3753 (2009).
- 23 Matsui, T., Agrawal, A., Nahata, A. & Vardeny, Z. V. Transmission resonances through aperiodic arrays of subwavelength apertures. *Nature* **446**, 517-521 (2007).
- 24 Spence, T. G. & Werner, D. H. Design of Broadband Planar Arrays Based on the Optimization of Aperiodic Tilings. *Antennas and Propagation, IEEE Transactions on* **56**, 76-86 (2008).
- 25 Namin, F., Petko, J. S. & Werner, D. H. Analysis and Design Optimization of Robust Aperiodic Micro-UAV Swarm-Based Antenna Arrays. *Ieee T Antenn Propag* **60**, 2295-2308 (2012).
- 26 Della Villa, A. *et al.* A comparative study of representative categories of EBG dielectric quasi-crystals. *Ieee Antenn Wirel Pr* **5**, 331-334 (2006).

- 27 Pantoja, M. F., Bray, M. G., Werner, D. H., Werner, P. L. & Bretones, A. R. A Computationally Efficient Method for Simulating Metal-Nanowire Dipole Antennas at Infrared and Longer Visible Wavelengths. *Ieee T Nanotechnol* **11**, 239-246 (2012).
- 28 Namin, F. A., Wang, X. & Werner, D. H. Reflection and transmission coefficients for finite-sized aperiodic aggregates of spheres. *J. Opt. Soc. Am. B* **30**, 1008-1016 (2013).
- 29 Della Villa, A. *et al.* Band gap formation and multiple scattering in photonic quasicrystals with a Penrose-type lattice. *Phys Rev Lett* **94** (2005).
- 30 Bauer, C. & Giessen, H. Light harvesting enhancement in solar cells with quasicrystalline plasmonic structures. *Opt Express* **21**, A363-A371 (2013).
- 31 Xu, Y. L. Electromagnetic scattering by an aggregate of spheres (vol 34, pg 4573, 1995). *Appl Optics* **37**, 6494-6494 (1998).
- 32 Xu, Y. L. & Wang, R. T. Electromagnetic scattering by an aggregate of spheres: Theoretical and experimental study of the amplitude scattering matrix. *Phys Rev E* **58**, 3931-3948 (1998).
- 33 Xu, Y. L. Efficient evaluation of vector translation coefficients in multiparticle light-scattering theories. *J Comput Phys* **139**, 137-165 (1998).
- 34 Hicks, E. M. *et al.* Controlling plasmon line shapes through diffractive coupling in linear arrays of cylindrical nanoparticles fabricated by electron beam lithography. *Nano Lett* **5**, 1065-1070 (2005).
- 35 Henson, J., DiMaria, J. & Paiella, R. Influence of nanoparticle height on plasmonic resonance wavelength and electromagnetic field enhancement in two-dimensional arrays. *Journal of Applied Physics* **106**, 093111 (2009).
- 36 Nikitin, A. G., Nguyen, T. & Dallaporta, H. Narrow plasmon resonances in diffractive arrays of gold nanoparticles in asymmetric environment: Experimental studies. *Appl Phys Lett* **102** (2013).
- 37 Johnson, P. B. & Christy, R. W. Optical Constants of the Noble Metals. *Phys Rev B* **6**, 4370-4379 (1972).
- 38 Felidj, N. *et al.* Grating-induced plasmon mode in gold nanoparticle arrays. *J Chem Phys* **123** (2005).
- 39 Jackson, J. D. *Classical electrodynamics*. 2d edn, (Wiley, 1975).
- 40 Stein, S. Additional Theorems for Spherical Wave Functions. (DTIC Document, 1959).
- 41 Steurer, W. & Deloudi, S. Crystallography of Quasicrystals: Concepts, Methods and Structures. *Springer Ser Mater S* **126**, 1-384 (2009).
- 42 Kaliteevski, M. A. *et al.* Two-dimensional Penrose-tiled photonic quasicrystals: from diffraction pattern to band structure. *Nanotechnology* **11**, 274-280 (2000).
- 43 Xu, Y. L. Electromagnetic scattering by an aggregate of spheres: far field. *Appl Optics* **36**, 9496-9508 (1997).
- 44 Grünbaum, B. & Shephard, G. C. *Tilings and patterns*. (Freeman, 1987).
- 45 Beenker, F. *Algebraic theory of non-periodic tilings of the plane by two simple building blocks: a square and a rhombus*. (Department of Mathematics and Computing Science, Eindhoven University of Technology, 1982).
- 46 Bohren, C. F. & Huffman, D. R. *Absorption and scattering of light by small particles*. (John Wiley & Sons, 2008).
- 47 Narusawa, T., Hiraki, A. & Komiya, S. Auger Spectroscopic Observation of Si-Au Mixed-Phase Formation at Low-Temperatures. *Appl Phys Lett* **21**, 272-& (1972).
- 48 Nakashima, K., Iwami, M. & Hiraki, A. Low-Temperature Diffusion of Au into Si in Si(Substrate)-Au(Film) System. *Thin Solid Films* **25**, 423-430 (1975).
- 49 Xie, T., Schmidt, V., Pippel, E., Senz, S. & Gosele, U. Gold-enhanced low-temperature oxidation of silicon nanowires. *Small* **4**, 64-68 (2008).



- 50 Buttner, C. C., Zakharov, N. D., Pippel, E., Gosele, U. & Werner, P. Gold-enhanced oxidation of MBE-grown silicon nanowires. *Semicond Sci Tech* **23** (2008).
- 51 Westwater, J. *et al.* The characteristics and oxidation of Vapor-Liquid-Solid grown Si nanowires. *Mater Res Soc Symp P* **452**, 237-242 (1997).
- 52 Hu, W. C. *et al.* Lithography-Free Synthesis of Freestanding Gold Nanoparticle Arrays Encapsulated Within Dielectric Nanowires. *Proc Spie* **7610** (2010).
- 53 Charnvanichborikarn, S., Wong-Leung, J. & Williams, J. S. Self-assembled Au nanoparticles in SiO<sub>2</sub> by ion implantation and wet oxidation. *Journal of Applied Physics* **106** (2009).
- 54 Habenicht, A., Olapinski, M., Burmeister, F., Leiderer, P. & Boneberg, J. Jumping, nanodroplets. *Science* **309**, 2043-2045 (2005).
- 55 Inasawa, S., Sugiyama, M. & Yamaguchi, Y. Laser-induced shape transformation of gold nanoparticles below the melting point: The effect of surface melting. *J Phys Chem B* **109**, 3104-3111 (2005).
- 56 Giermann, A. L. & Thompson, C. V. Solid-state dewetting for ordered arrays of crystallographically oriented metal particles. *Appl Phys Lett* **86** (2005).
- 57 Kim, D., Giermann, A. L. & Thompson, C. V. Solid-state dewetting of patterned thin films. *Appl Phys Lett* **95** (2009).
- 58 Wang, D., Ji, R. & Schaaf, P. Formation of precise 2D Au particle arrays via thermally induced dewetting on pre-patterned substrates. *Beilstein J Nanotech* **2**, 318-326 (2011).
- 59 Burrows, C. P. & Barnes, W. L. Large spectral extinction due to overlap of dipolar and quadrupolar plasmonic modes of metallic nanoparticles in arrays. *Opt Express* **18**, 3187-3198 (2010).
- 60 Meier, M., Wokaun, A. & Liao, P. F. Enhanced Fields on Rough Surfaces - Dipolar Interactions among Particles of Sizes Exceeding the Rayleigh Limit. *J Opt Soc Am B* **2**, 931-949 (1985).
- 61 Lamprecht, B. *et al.* Metal nanoparticle gratings: Influence of dipolar particle interaction on the plasmon resonance. *Phys Rev Lett* **84**, 4721-4724 (2000).
- 62 Kaliteevski, M. A. *et al.* Diffraction and transmission of light in low-refractive index Penrose-tiled photonic quasicrystals. *J Phys-Condens Mat* **13**, 10459-10470 (2001).
- 63 Agrawal, A., Matsui, T., Vardeny, Z. V. & Nahata, A. Terahertz transmission properties of quasiperiodic and aperiodic aperture arrays. *J Opt Soc Am B* **24**, 2545-2555 (2007).
- 64 Janssen, T. Aperiodic Crystals - a Contradictio in Terminis. *Phys Rep* **168**, 55-113 (1988).
- 65 Janot, C. & Dubois, J. M. Quasicrystals. *J Phys F Met Phys* **18**, 2303-2343 (1988).
- 66 De Bruijn, N. in *Indagationes Mathematicae (Proceedings)*. 39-52 (Elsevier).
- 67 Mackay, A. L. Crystallography and the Penrose pattern. *Physica A: Statistical Mechanics and its Applications* **114**, 609-613 (1982).
- 68 Alivisatos, P. The use of nanocrystals in biological detection. *Nature biotechnology* **22**, 47-52 (2003).

## **Chapter 3**

### **Self-Organized Freestanding 1D Au Nanoparticle Arrays**

In this chapter, one-dimensional (1D) gold (Au) nanoparticle arrays encapsulated within freestanding silicon dioxide ( $\text{SiO}_2$ ) nanowires are fabricated by thermal oxidation of Au-coated nanowires with predefined surface modulation. This technique leads to a versatile platform for creating 1D Au nanoparticle arrays with highly controllable particle diameter and interparticle spacing. Specifically, the resultant Au nanoparticle diameter is determined by the starting diameter of the Si nanowire and Au film thickness, while the interparticle spacing is controlled by the modulation of starting Si nanowire. The optical absorption of a randomly oriented ensemble of wires exhibited a strong plasmonic response at a wavelength of approximately 550nm. Scanning transmission electron microscopy electron energy loss spectrum (STEM-EELS) of individual 1D nanoparticle arrays confirmed the same plasmonic response with a resonance energy at 2.25eV (552nm). A uniform “halo” was observed around each nanoparticle in the array at the resonance energy of the individual nanoparticle, which demonstrates the high uniformity in the size and optical properties of the Au nanoparticles in the array. Energy filtered transmission electron microscopy (EFTEM) measurements of single wires reveal the presence of interparticle coupling between particles at the resonant energy of the structure.

The Au nanoparticle array fabrication process was developed in collaboration with Dr. Wenchong Hu. The STEM and EFTEM measurements were performed by Dr. Mahalingam Krishnamurthy at the Air Force Research Laboratory, Dayton OH.

### 3.1 Background and Motivation

Localized surface plasmonic properties of noble metal nanoparticles and their assemblies have recently attracted intense interest because they hold promise for a broad range of applications, including biodetection<sup>1</sup>, surface enhanced Raman spectroscopy<sup>2</sup>, optical waveguides<sup>3-5</sup>, nanoantenna<sup>6,7</sup> and negative refractive index materials<sup>8,9</sup>. These applications are based on the strong electromagnetic field enhancement at the surface of the metal nanoparticle, and their behavior can be modified by manipulating intrinsic (particle shapes, sizes, dimensions, arrangement, materials) and extrinsic properties (the dielectric constant of the surrounding media, the incident wave polarization and wavevector direction). Among all of the possible nanoparticle assemblies, 1D nanoparticle arrays demonstrate a variety of unique properties. When they have a small interparticle spacing within the near-field coupling regime, their electromagnetic energy propagation can be guided below the diffraction limit and through a 90° bend without significant information loss<sup>3,4,10,11</sup>, which makes them ideal for waveguides. When they are configured with large interparticle spacing, sharp plasmonic peaks<sup>12,13</sup> can be achieved through far-field diffractive coupling between the nanoparticles, which offers high sensitivity for sensors. All of these applications, however, strongly rely on accurately controlling the nanoparticle dimensions, interparticle spacing, and placement in the array.

To meet the needs of different applications, extensive efforts have been invested in optimizing fabrication processes to produce nanoparticle arrays with a range of geometries. The traditional method for fabricating the arrays on planar substrates uses direct write electron-beam lithography, metal evaporation, and liftoff<sup>12,14</sup>. In this case, the nanoparticle size, interparticle spacing and placement are defined through the patterning and deposition process. Unfortunately, this process is not scalable or cost-effective and it is not suitable for mass production. Solution-based assembly of nanoparticles through DNA<sup>15</sup> or other linker molecules<sup>16</sup> greatly reduces the cost

and enables large-scale fabrication, but at the expense of full controllability in the spacing (pre-determined by the length of the molecular and DNA) and uniformity of the particles. Laser heating<sup>17-19</sup> and in-fiber fabrication<sup>20,21</sup> enable a cost-effective and high-throughput method with better engineering flexibility, but interparticle spacing has been limited to the micro-meter scale. Alternative methods, such as annealing of thin films<sup>22</sup> or patterned<sup>23</sup> Au-coated Si substrates produce nanoparticle arrays with poor controllability in both diameter and inter-particle spacing. Au nanoparticle arrays formed by oxidation and annealing of Au-coated, vapor-liquid-solid (VLS) grown Si nanowires<sup>24,25</sup> provide better engineering strategies in manipulating diameter and interparticle spacing. However, the linear dependence of spacing on nanoparticle diameter, which is dictated by the Rayleigh instability<sup>26</sup>, limits the ability to engineer the spacing between particles. In addition, the non-uniformity in the starting nanowire diameters also causes variations in the final particle dimensions, which widens the resulting plasmonic peak width.

This thesis research developed a simple yet effective method to synthesize the self-organized 1D Au nanoparticle arrays, encapsulated within freestanding SiO<sub>2</sub> nanowires, with independent and precise control of nanoparticle diameter and spacing. This is achieved by thermal oxidation of Au-coated Si nanowires with controllable starting diameters and predefined surface modulation, formed via deep reactive ion etching (DRIE) processing. The surface modulation introduces an additional degree of freedom to optimize the properties of the 1D nanoparticle arrays, which allows their optical properties to be engineered for a specific application.

To evaluate the process, nanowires with four different surface modulation wavelengths of 130nm to 630nm were fabricated and coated with Au thin films that varied in thickness from 5nm to 20nm. The diameter of the resultant Au nanoparticles in the array is determined by the volume of the deposited Au, and their interparticle spacing is defined by the surface modulation wavelength of the wire. Optical characterization and spectroscopic analysis of 1D arrays with 80nm diameter Au nanoparticles spaced by 230nm demonstrated the plasmonic response of the structure. An

intense plasmonic peak at 550nm was identified from optical absorption measurements of an ensemble of randomly oriented wires. The uniformity in the Au nanoparticle properties was confirmed by EELS and STEM measurements of individual wire arrays. Additional EFTEM analysis showed weak optical coupling between adjacent Au nanoparticles within the same array.

The results in this thesis demonstrate that this fabrication method provides a cost-effective and scalable approach to create freestanding 1D nanoparticle array building blocks with increased flexibility for future plasmonic devices. Once synthesized, these arrays can be assembled into higher dimensional arrays to construct structures with increased complexity and optical functionality.

### 3.2 Rayleigh Instability

Rayleigh instability theory was first developed by Rayleigh to describe the instability of jets of fluid and then extended by Nicholas and Mullins<sup>27,28</sup> to solids. It describes the thermodynamic instability of an infinite cylindrical wire due to capillary-induced surface tension, which favors fragmentation into a chain of smaller, separated particles under small heating-induced sinusoidal longitudinal perturbations. A constant ratio, which is related to the perturbations and largely depends on the specific system<sup>29-31</sup>, dictates the linear relationship between the final particle diameter and interparticle spacing.

This instability was observed during the thermal oxidation of Au-coated Si nanowires with smooth surfaces in Figure 3-1(a). After depositing a thin-film Au, the nanowires were thermally treated at high temperature under flowing oxygen (O<sub>2</sub>). During dry oxidation, the presence of Au weakens the covalent bond between Si atoms and increases the extraction and oxidation rate of Si at the Si-Au interface. This promotes the movement of Au towards the core of nanowires to reduce the surface and interfacial free energy. The Si nanowires are rapidly oxidized into SiO<sub>2</sub>. When the Si is completely consumed, the oxidation stops, and the evaporated Au film forms crystalline Au

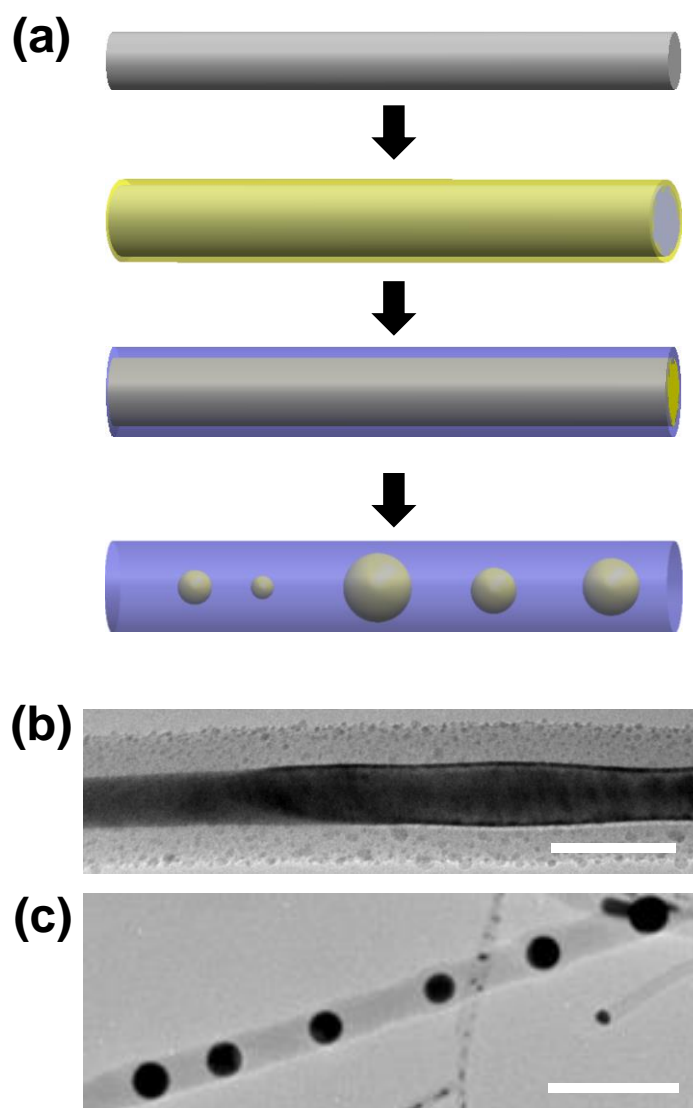


Figure 3-1. (a) Schematic process for Au nanoparticle chain formed on smooth wire; (b) TEM image of the Au wire formed within the SiO<sub>2</sub> shell. Scale bar, 50nm; (c) TEM image of the Au nanoparticle chain formed within the SiO<sub>2</sub> shell after further thermal treatment. Scale bar, 50nm.

nanowires encapsulated in SiO<sub>2</sub> matrix, as shown in Figure 3-1(b). Due to the small sinusoidal perturbations, the Au wires then fragment into smaller particles to reduce the interfacial energy between the Au and SiO<sub>2</sub>, as shown in Figure 3-1(c). The perturbation wavelength is not controlled, which leads to a large distribution in nanoparticle size and interparticle spacing within the same

array. The diameter and interparticle spacing of the nanoparticles formed from the same batch of Si nanowires varied from 10nm to 54nm and from 27nm to 170nm, respectively<sup>24</sup>. The inability to control the perturbation limits the usefulness of this process for structures that require homogeneous and reproducible optical properties.

The research in this thesis describes a strategy to control the perturbation wavelength along the Si nanowire, and thereby achieve Au nanoparticle arrays with predefined nanoparticle diameter and interparticle spacing. The process flow is illustrated in Figure 3-2 (a). In the first step, DRIE is used to create Si nanowires with a well-controlled and reproducible surface modulation. The etched wires are cleaned and coated with a conformal Au layer, and then they are thermally treated at elevated temperature in a flow of oxygen ( $O_2$ ). The Au-enhanced oxidation process described in Chapter 2 results in the formation of a 1D array of individual Au nanoparticles with diameter and interparticle spacing determined by the geometry of the starting Si nanowire and Au layer thickness. Notably, the surface profile introduces a controlled perturbation in the Rayleigh instability. The concave region in the modulated wires corresponds to the trough in the undulation. The Au atoms in the concave region migrate to the convex region, triggering the fragmentation of the Au wire to form isolated Au nanoparticles.

Field emission scanning electron microscope (FESEM) images showing the evolution of the process for one particular type of wire are presented in Figure 3-2 (b) and (c). The starting wire has a 200nm maximum diameter (convex region), an 80nm minimum diameter (concave region), and 630nm modulation wavelength. The starting nanowire diameter and 20nm thickness of the deposited Au layer determine the total volume of Au, and thus the diameter of the final Au particles. The FESEM images show that the thermal treatment causes the Au to migrate to the center and form a continuous Au wire with a diameter that follows the surface modulation of the starting Si wire. With increased thermal treatment time, the continuous Au wire breaks into discrete segments, which are subsequently converted into spherical Au nanoparticles. In this wire, the diameter of the

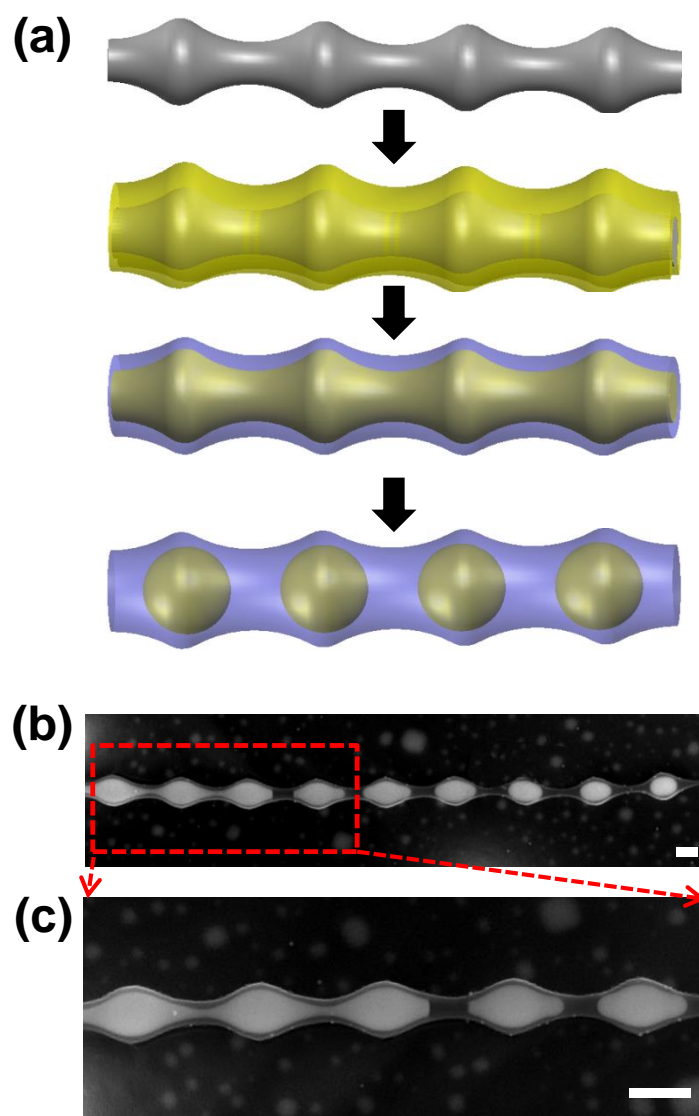


Figure 3-2 (a) Schematic illustration of process for 1D Au nanoparticle array formed using wires with controlled surface undulations; (b) and (c) Evolution of Au nanoparticle array formation inside the SiO<sub>2</sub> wire. Scale bar, 200nm.

Au nanoparticles are  $200\text{nm} \pm 10\text{nm}$  and their interparticle spacing is  $622\text{nm} \pm 17\text{nm}$ . This example confirms that this fabrication approach relaxes the linear relationship between the diameter and interparticle spacing imposed by the Rayleigh instability<sup>24,26</sup>.



### 3.3 Synthesis Process

This improved control in particle uniformity and interparticle spacing that this process affords over arrays formed by the Raleigh instability is studied in this section. Silicon nanowires with smooth surfaces were prepared by VLS growth, and wires with controlled surface undulations were fabricated by DRIE. The surface structure was created by properly adjusting the etching ( $\text{SF}_6$ ) and the polymer deposition ( $\text{C}_4\text{F}_8$ ) time during each cycle in the Bosch DRIE process. Table 3.1 summarizes etching conditions for the four types of nanowires studied in this research. Figure 3-3 (a) plots the distribution in diameter and interparticle spacing for Au nanoparticle arrays fabricated with different modulation length, nanowire diameter, and Au layer thickness.

#### 3.3.1 Smooth Nanowire Template Results

Free-standing Au nanoparticle arrays formed by oxidizing Au-coated Si nanowires with smooth surfaces can be used as a baseline for comparison to wires having surface modulation. The smooth-surface nanowires were grown by VLS method using Au as a catalyst<sup>32</sup>. The diameters of the starting as-grown nanowires in each batch varied from 20nm to 50nm, which contributes to a wide distribution in the final nanoparticle size. Prior to Au-enhanced oxidation, the catalyst metal was removed from the wire tips by selective wet chemical etching. The wires were removed from the substrate by sonication, dispersed onto a sacrificial  $\text{Si}_3\text{N}_4$ -coated Si substrate, and then coated with a uniform layer of 10nm thick Au metal along the entire length of the wire. To ensure that an intimate contact was made between the deposited Au layer and the Si wire, the nanowires were exposed to a brief buffer oxide etchant (JT Baker BOE 10:1) dip for 30sec to remove the native oxide before loading into the evaporator. After Au metal deposition, the nanowires were then

thermally treated in a 15in-diameter tube furnace at a temperature of 850° under O<sub>2</sub> with a flow rate of 0.8L/min for 2 hours.

As shown by the gray symbols in the plot of interparticle spacing versus diameter in Figure 3-3(a), the diameters of the resultant Au nanoparticles formed using the smooth-surface nanowire varied from 9nm to 60nm, while the corresponding interparticle spacing ranged from 27nm to 170nm. The arrays formed using these wires followed a linear relationship between the average Au nanoparticle diameter and the spacing with a diameter-to-spacing ratio of three, as illustrated by the slope of the dashed gray line in Figure 3-3(a). This ratio falls within the type range of values observed for the Rayleigh instability, which is between 2.3 and 4.5<sup>26</sup>. This confirms that the Rayleigh instability is the primary mechanism that promotes nanoparticle formation in these wires. The linear relationship between particle diameter and interparticle spacing limits the flexibility to independently tune the nanoparticle diameter and the interparticle spacing.

### 3.3.2 Surface-Modulated Nanowire Template Result

Surface-modulated Si nanowires were fabricated to study the effect of the starting wire diameter, modulation length, and Au layer thickness on the final particle diameter and interparticle spacing. Uniform diameter nanowires with three different modulation wavelengths of 230 nm, 460 nm, and 630 nm were fabricated using a modified DRIE process. The fabrication process began by forming a dense array of 6μm long, vertically oriented Si wires with a nominal diameter of 1.2 μm diameter and a center-to-center pitch of 3μm on a 3-inch diameter  $n^{++}$  Si substrate (resistivity <0.005 Ω.cm). The wire array features were patterned using project photolithography (GCA 8000 i-line stepper), and the pattern was transferred into the Si substrate using a modified DRIE (Alcatel Speeder 1000) process. During DRIE, the alternating etching and polymer deposition cycles were

adjusted to controllably create the desired surface modulation (concave and convex segment regions) along the length of the wire, as illustrated in Figure 3-1(a).

Table 3-1 summarizes the cycle times of the  $\text{SF}_6$  etching step and the  $\text{C}_4\text{F}_8/\text{O}_2$  step used to create each type of wire. The same flow rate of 200sccm  $\text{SF}_6$ , 150sccm  $\text{C}_4\text{F}_8$ , and 100sccm  $\text{O}_2$  was used to fabricate all of the wires. An additional  $\text{O}_2$  step was added after each cycle to remove the Teflon like polymer at the base of the structure that is generated during the  $\text{C}_4\text{F}_8$  cycle. This was required to produce wires with uniform diameter along their entire length. Following DRIE, the wire arrays with the 430nm and the 630nm surface modulation wavelengths were subjected to two iterations of wet oxidation at  $1000^\circ\text{C}$  for 90min to form an oxide shell and subsequent oxide removal in 5% hydrofluoric acid to reduce the wire diameter. Approximately  $1\mu\text{m}$  of Si was removed during each cycle, resulting in nanowires with a final diameter of 195nm maximum/80nm minimum for the 430nm modulation wavelength and 290nm maximum/80nm minimum for the 630nm surface modulation wavelength. For the 230nm surface modulation wavelength, a third dry oxidation step was performed at  $1000^\circ\text{C}$  for 120min to further reduce the diameter to 90nm maximum/65 nm minimum. Similar to the smooth-surface wires, these etched wires were removed

Table 3-1. Summary of etching conditions for the four types of surface modulated Si nanowires used to create the 1D Au nanoparticle arrays.

<b>Surface Modulation (nm)</b>	<b><math>\text{SF}_6</math> etching</b>		<b><math>\text{C}_4\text{F}_8</math> Polymer</b>		<b><math>\text{O}_2</math> cleaning</b>		<b>Total etching time (s)</b>
	<b>Time (s)</b>	<b>Flow (sccm)</b>	<b>Time (s)</b>	<b>Flow (sccm)</b>	<b>Time (s)</b>	<b>Flow (sccm)</b>	
<i>130nm (taper)</i>	2	200	1	150	0	0	2
<i>230nm(uniform)</i>	3	300	1.5	300	1	100	2
<i>430nm(uniform)</i>	7	300	3.5	300	2.3	100	2
<i>630nm(uniform)</i>	10	300	5	300	3.3	100	2

from the Si substrate and dispersed onto a nitride-coated Si wafer for deposition of Au films with thicknesses of 5nm, 10nm and 20nm. Following metal deposition, Au-enhanced thermal oxidation was performed in O<sub>2</sub> with flow rate of 0.8L/min at 850°C for 2 hours. This produced a set of 1D nanoparticle arrays with systematic variations in the Au particle diameter and interparticle spacing.

Figure 3-3 shows that 1D nanoparticle arrays with constant spacing and different diameters can be achieved by varying the Au coating thickness on nanowires with the same surface modulation wavelength. Taking the nanowires with 630nm surface modulation as an example, the nanoparticle diameter is  $88\text{nm} \pm 6\text{nm}$ ,  $118\text{nm} \pm 6\text{nm}$  and  $200\text{nm} \pm 10\text{nm}$  for Au coating thicknesses of 5nm, 10nm and 20nm, respectively. In these arrays, the interparticle spacing was tightly

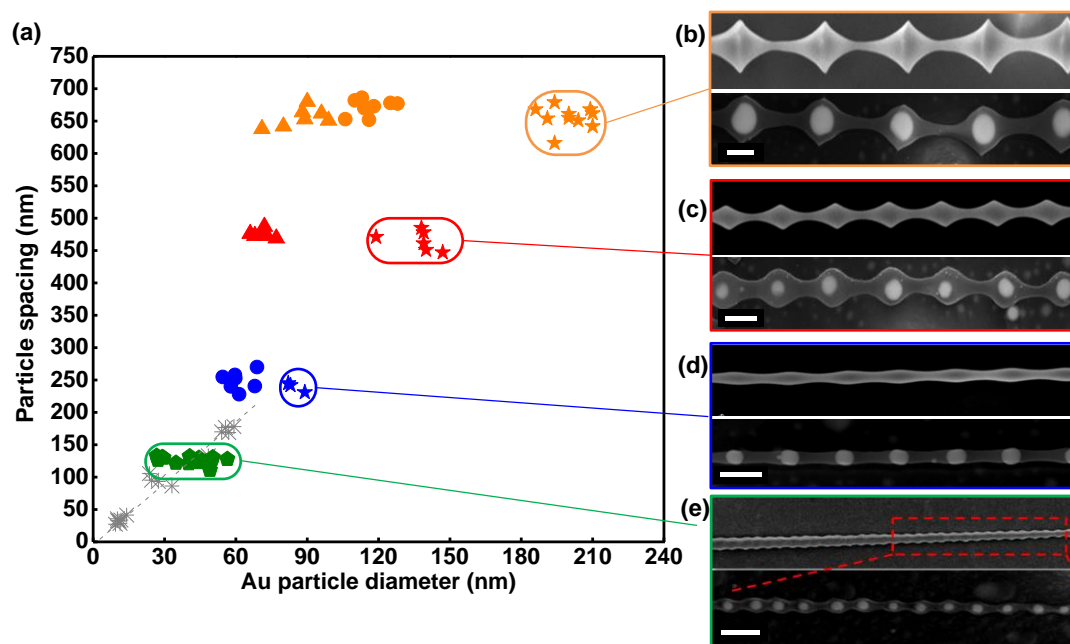


Figure 3-3. (a) Distribution of Au nanoparticle arrays with controlled interparticle spacing and diameter formed by the same thermal treatment at 800 °C for 2 hours; (b), (c), (d) and (e) corresponding FESEM images: the top image in each colored box was taken at an accelerating voltage of 5kV, and the bottom image was taken at an accelerating voltage of 20kV. All scale bars, 200nm. The symbol represents the Au coating thickness/the modulation wavelength; ★ 20nm/630nm; ● 10nm/630nm; ▲ 5nm/230nm; ★ 20nm/430nm; ▲ 5nm/430nm; ● 10nm/230nm; ★ 20nm/230nm; ◆ Tapered wires with 10nm Au coating; ✱ smooth wires with 10nm Au coating.

constrained around the 630nm modulation length of the starting wire. This indicates that the surface modulation determines the final interparticle spacing and the Au thickness determines the nanoparticle diameter. Comparing this result with the nanoparticle arrays formed via the Rayleigh instability, the linear relationship between the diameter and interparticle spacing is relaxed.

Arrays with the same nanoparticle diameter but different spacing can be realized by simultaneously tuning the Au coating thickness and modulation length. For example, as shown in Figure 3-3 (a), Au nanoparticles with an 80nm diameter can be achieved by either coating a 5nm thick layer of Au on the wires with a 630nm surface modulation wavelength, or by coating a 20nm Au layer on the wires with a 230nm modulation. In this case, the interparticle spacing between the nanoparticles is independently varied without changing the particle diameter.

Nanoparticle arrays with different particle diameter and interparticle spacing can be made by varying the modulation wavelength and keeping the Au coating thickness constant, as shown by the FESEM images in Figure 3-3 (b), (c) and (d). The top images were taken at a 5kV accelerating voltage to show the surface morphology, and the bottom images were taken at 20kV to show the embedded spherical nanoparticle chains. The interparticle spacing in arrays fabricated by depositing 20 nm of Au on wires with modulation wavelengths of 230nm, 430nm and 630nm are  $238\text{nm} \pm 21\text{nm}$ ,  $435\text{nm} \pm 38\text{nm}$  and  $622\text{nm} \pm 17\text{nm}$ , respectively. The final Au nanoparticle diameters are  $80\text{nm} \pm 10\text{nm}$ ,  $120\text{nm} \pm 19\text{nm}$  and  $190\text{nm} \pm 10\text{nm}$ , respectively. This shows that, for a constant Au thickness, the particle diameter depends on the diameter of the starting wire, and thus the total volume of Au coated on the nanowires.

These results demonstrate that combining surface modulation with Au enhanced oxidation can be used to overcome the dependence of the Au nanoparticle diameter and interparticle spacing due to the Rayleigh instability in wires with smooth surfaces.

### 3.3.3 Variable Diameter Surface Modulated Nanowire Template Results

The nanoparticle diameter can be varied along the length of the 1D array while a constant interparticle spacing is maintained. Changing the diameter of a Si nanowire with constant surface modulation wavelength results in different Au volumes, and hence different particle diameters, in each wire segment. Tapered nanowires were fabricated by removing O<sub>2</sub> polymer clean step from the DRIE process. The detailed etching conditions can be found in Table 3-1.

A FESEM image of a Si nanowire with a 130nm surface modulation wavelength and a diameter that increases from 65nm at the top to 125nm at the bottom of the wire is shown in Figure 3-3 (e). The resulting Au nanoparticle array formed by Au-enhanced oxidation of the same wire with a 10nm Au coating is shown in the bottom image of the same figure. The diameter of the Au nanoparticles along the array increased monotonically from 37nm for the second particle from the top to 47nm for the second particle from the bottom of the wire. Notably, the interparticle spacing was maintained at 130nm, following the modulation wavelength of the starting wire, independent of the nanoparticle diameter. This example demonstrates the flexibility of the approach to tailor the nanoparticle diameter along the length of the array while maintaining a fixed interparticle spacing. More sophisticated arrays that vary both the particle diameter and interparticle spacing in a more arbitrary fashion can be realized by properly engineering the diameter and modulation wavelength of each segment along the starting Si nanowire.

## 3.4 Optical Characterization of Freestanding 1D Nanoparticle Arrays

The plasmonic properties of the 1D Au nanoparticle arrays were determined by measuring their extinction spectra. A randomly oriented ensemble of 6 $\mu$ m long arrays composed of 80nm diameter nanoparticles with a 230nm interparticle spacing and a 100nm thick SiO<sub>2</sub> shell was

produced by dispersing the freestanding wires in a solution of isopropanol. The optical properties of the 80nm diameter Au nanoparticles are due to scattering rather than absorption<sup>33</sup>. Figure 3-4 (b) shows the extinction spectrum collected from a randomly oriented ensemble of 1D nanoparticle arrays using a UV-VIS spectrometer (PerkinElmer Lambda 9500) with unpolarized light. The transmitted beam energy was measured and referenced to the incident beam energy to extract the extinction energy. The measured spectrum shows an intense extinction peak at a wavelength of 550nm.

For comparison to theory, a finite difference time domain (FDTD) electromagnetic simulation was performed on an 1D nanoparticle array composed of five 80nm diameter spherical Au nanoparticles encapsulated in a 100nm diameter SiO<sub>2</sub> nanowire ( $n=1.47$ ) and spaced at center-to-center distance of 230nm. The surrounding medium was isopropanol ( $n=1.38$ ) and the crystalline Au Johnson-Christy Au dispersive properties were used for the nanoparticles. The incident electric field was swept from parallel to vertical respective to the long axis of the wire and the average response is plotted in Figure 3-4 (b). The peak position in the simulated spectrum is 558nm, which is red-shifted compared to the measurement. There are two possible reasons that could contribute to this difference: (1) the 12 % variation in the nanoparticle diameter and interparticle spacing could contribute to the shift that is observed; and (2) the nanowires are randomly oriented during measurement, which can be viewed as disorder in the perfect 1D array. As demonstrated by previously<sup>13,34</sup>, disorder partially cancels the interaction between particles in the array, causing a blue-shift of the plasmon peak.

The plasmonic resonance at 558nm corresponds to the coupled plasmonic dipolar modes of the Au nanoparticles. Because the particle size in the array is larger than 50nm, the particle can support the quadrupolar mode<sup>35</sup>. To efficiently couple incident light to the quadrupolar mode, the phase of the incident light must change significantly across the particle<sup>35</sup>. The rapid spatial phase change occurs more easily at higher frequency. Thus, the higher scattering intensity at short

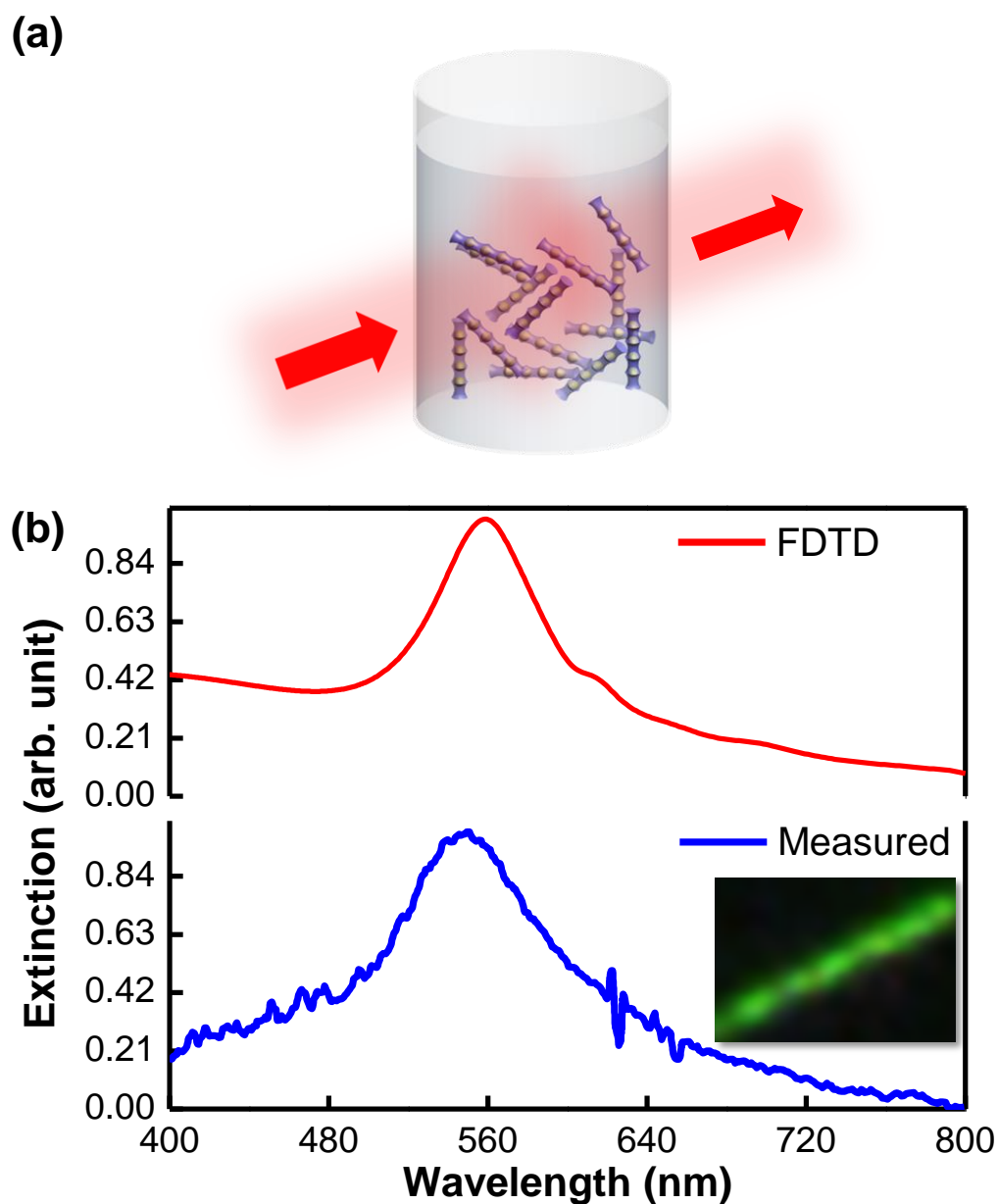


Figure 3-4. (a) Illustration of optical extinction measurement of freestanding 1D Au nanoparticle arrays chain ensemble in isopropanol solution; (b) Calculated (top) extinction spectrum of individual Au nanoparticle chain in IPA solution, measured (bottom) extinction spectrum of the 1D Au nanoparticle chain ensemble in IPA solution; Inset: the dark field microscopy images of the individual 1D Au nanoparticle array; the green color agrees well with the plasmonic peak.



wavelengths is due to the excitation of the quadrupolar mode<sup>36</sup>. This phenomenon was observed in both the experiment and simulation. In addition, the transition between optical bands also contributes to the strong extinction at shorter wavelengths.

Applying a Lorentzian fit to both the experimental and the simulated resonant response gives a full-width at half maximum (FWHM) of 76nm for the nanofabricated arrays and 60nm for the simulated array. This discrepancy could be explained, in part, by the smaller number of particles included in the simulation as compared to experiment. Schatz *et.al.*<sup>37</sup> showed theoretically that the peak width first narrows as the number of particles in the array increases beyond two, and then broadens when the number of particles in the array exceeds 100. An array of five Au nanoparticles was used in the FDTD simulation. However, the 1D arrays present in the ensemble optical measurement contained as few as 3 to as high as 30 nanoparticles. This is because the starting 6 $\mu$ m long wires break during sample preparation and manipulation.

The optical properties of individual 1D Au nanoparticle arrays was characterized by collecting dark-field scattering images using an upright microscope (Nikon TE 200U). For this measurement, the nanowires were dropped onto a glass slide at a density low enough to isolate a single wire in the beam path. The array is illuminated with unpolarized white light from tungsten-halogen lamp using an oil dark-field condenser (NA=1.2-1.43) in transmission mode. The light scattered from the arrays is collected with a 100 $\times$  objective lens and imaged with a digital CCD camera. As shown in the inset of Figure 3-4(b), the scattering images display a uniform green color, which is within the wavelength range of 520nm to 570nm. This is consistent with the position of the extinction peak in the ensemble measurement, and further confirms the plasmonic response of the freestanding 1D Au nanoparticle arrays fabricated by Au enhanced oxidation.

### 3.5 Transmission Electron Microscopy Characterization

Scanning transmission electron microscopy (STEM)<sup>38,39</sup> is used to characterize the plasmonic response of individual particles in the freestanding 1D array, while EFTEM<sup>40</sup> is capable of studying interparticle interactions along the array with much higher spatial resolution than conventional optical techniques. By scanning the electron beam probe with a spot size of only 1nm in the STEM, it is possible to excite and collect the energy loss spectrum of individual particles in the array. The raw electron energy loss spectrum<sup>41</sup> (EELS) along with the corresponding dark-field STEM of the same nanoparticle array is shown in Figure 3-5 (a). This data was collected from the same batch of wires as those used for optical extinction measurements in Section 3.4. The EELS spectrum has a large peak at 2.25eV, which corresponds to a wavelength of 552nm. Using the dynamic resonance condition for individual spherical nanoparticles<sup>42</sup>, the localized surface plasmon (LSP) resonance of an individual 80nm diameter nanoparticle encapsulated in SiO<sub>2</sub> is calculated to be 540nm, which is consistent with the EELS measurement result.

The energy map of the same nanoparticle array was collected to spatially resolve the energy distribution around each particle, as shown in Figure 3-5(b). In the 2.25eV energy map that is collected with an energy window width of 0.5eV, a uniform “halo” of bright contrast extends away from the surface of each particle in the array. This is caused by the excitation of the surface plasmon at the resonant energy. In the 3.25eV energy map, which is at an energy outside the resonant plasmonic mode, the intensity of collected electrons is uniform across each particle. This indicates that there is no coupling between the incident electrons and the Au nanoparticles at this energy.

The nanoparticles in the array can be simultaneously excited by EFTEM with a parallel incident electron beam. Figure 3-6 (a-c) shows raw EFTEM images collected for series of energy loss values centered at 1.6eV, 2.2eV and 3.2eV with a predefined energy width of 0.2eV. These measurements further confirm that the resonance condition occurs at 2.2eV, which corresponds to

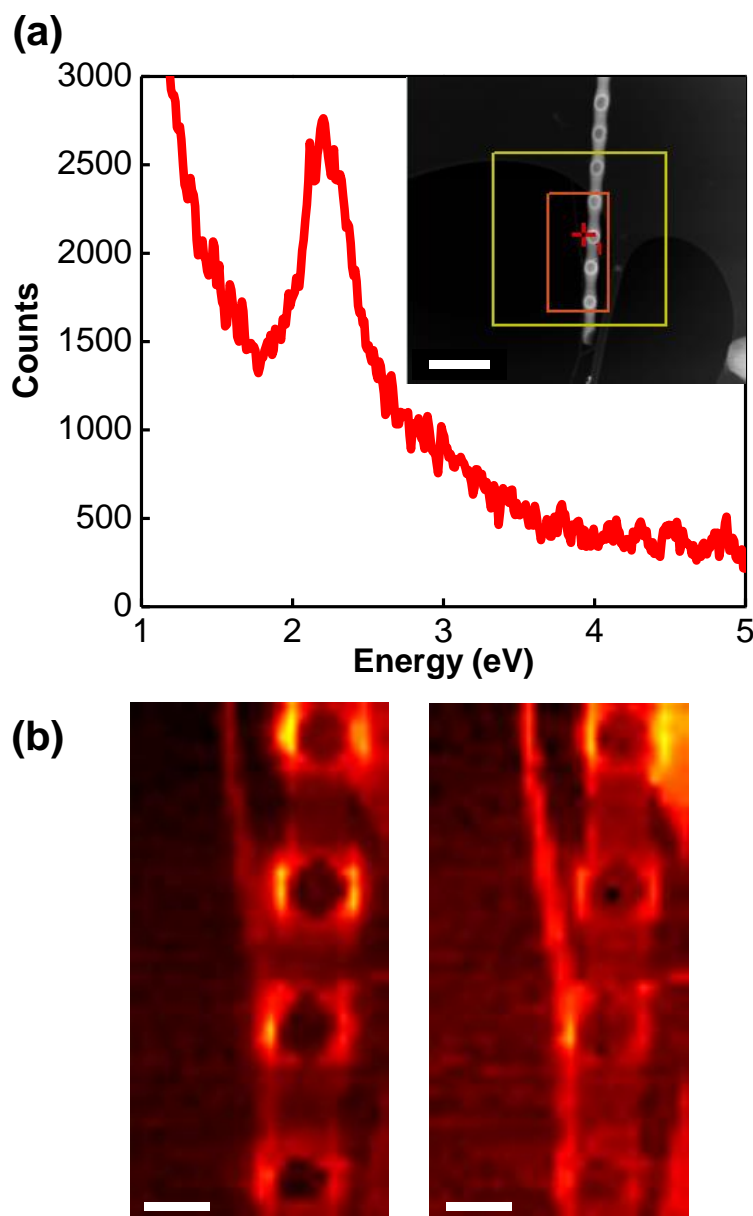


Figure 3-5. (a) Electron energy loss spectrum of the individual 1D Au nanoparticle array. The surface plasmon peak is at 2.25 eV. Scale bar: 500 nm. The inset shows the STEM image of the measured Au nanoparticle array, the red box is the region from which the spectrum image is taken, the beam is positioned at the red cross outside the particle and the yellow box is the area that was used for drift correction during experiment; (b) Energy map of the individual 1D nanoparticle array at beam energy of  $2.25 \text{ eV} \pm 0.25 \text{ eV}$  (left) and  $3.25 \text{ eV} \pm 0.25 \text{ eV}$ . Scale bar: 100 nm. The maps are extracted from the spectrum image data with a window of width 0.5 eV. The energy intensity around the particle is enhanced at the resonance energy. Note: The “halo” only occurs along the axial direction because the thick 100 nm oxide in the radial direction prevents electrons from being collected.

a wavelength of 560nm. This value agrees with the optical extinction spectrum collected for the wire ensemble, demonstrating that the plasmonic response of this structure is not sensitive to the surrounding environment (isopropanol versus vacuum). This is confirmed through electromagnetic simulations of the same structure. The agreement in the peak position between the EFTEM of individual nanoparticle arrays and the optical measurements of the ensemble verifies the uniformity of the Au nanoparticles formed using this fabrication approach.

At the plasmonic resonance of 2.2eV, a bright contrast is present both around and between the particles. This indicates the presence of electromagnetic coupling when multiple particles along the array are excited simultaneously. This bright contrast is not observed when the array is excited at 1.6eV or 3.2eV. To interpret the coupling and to correlate the optical plasmon mode<sup>43</sup> to the spatial distribution of the energy loss probability, electrodynamic simulations were performed on the individual 1D nanoparticle arrays (COMSOL Multiphysics 4.2a, RF Module). In the simulation, the Au nanoparticles were modeled as 80nm diameter spherical particles with JC optical properties. The surface modulation was modeled as a two 115nm tall cones mirrored about the center plane of the nanoparticle, where the diameter at the base of the cone is 100nm and the diameter at the top of the cone is 60nm. The surrounding environment is vacuum with  $n=1$ .

Figure 3-6 plots the distribution of the total electric field intensity  $|E|^2$  at the center Au nanoparticles for incident energies of 1.6eV, 2.2eV and 3.2eV, with the incident electric field parallel (d-f) or perpendicular (g-i) to the long-axis of the nanoparticle array. A strong qualitative agreement is observed between the simulated electromagnetic field distribution and the experimentally measured electron energy loss probability. The electron loss probability is related to the photonic local density of states (LDOS)<sup>44</sup>, and  $|E|^2$  represents the scanning near field optical microscopy intensity<sup>45</sup> that is given by the LDOS<sup>46</sup>. At the resonant energy of 2.2eV, the highest field intensity occurs around particles, and the field gradually decreases between adjacent particles in the array. In contrast, the field intensities around and between the nanoparticles are both weak

when the incident energy is lower or higher than the resonance energy (1.6eV and 3.2eV). This demonstrates that the electromagnetic coupling between the nanoparticles only occurs near the resonant energy of an individual array.

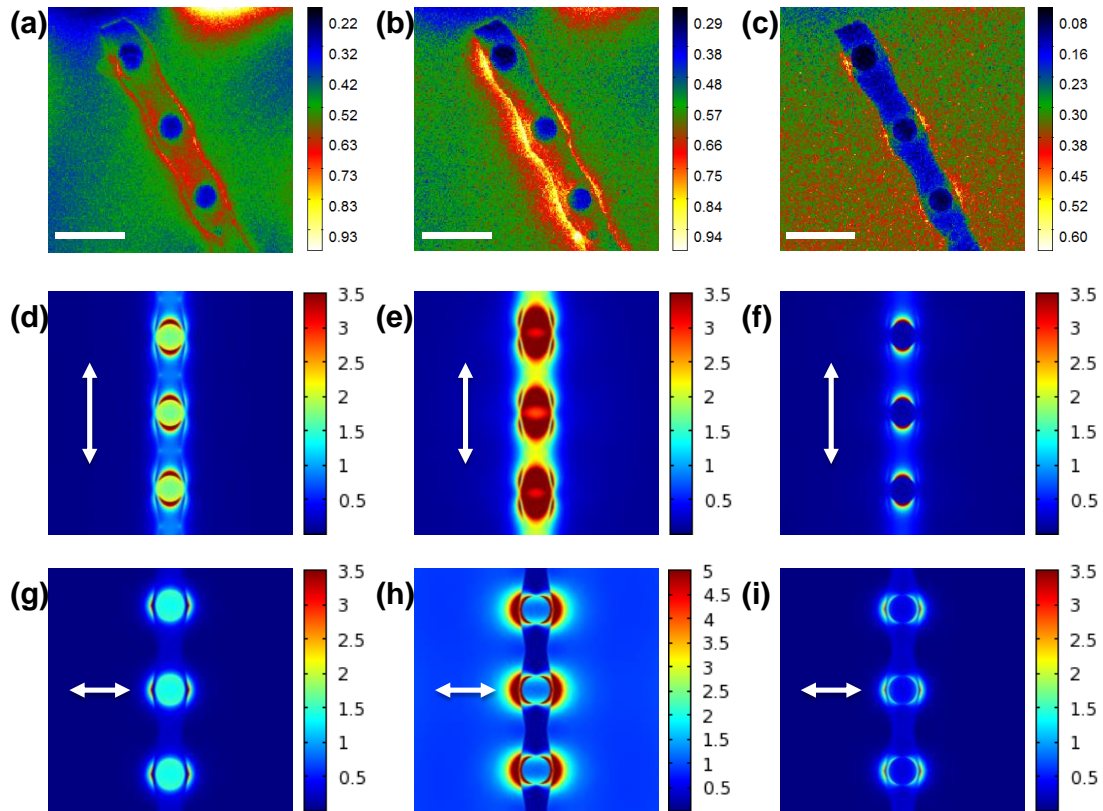


Figure 3-6. EFTEM images at (a) 1.6 eV (b) 2.2 eV (c) 3.2 eV of an individual Au nanoparticle chain, scale bar :200 nm; theoretical distribution of the electromagnetic field intensity  $|E|^2$  at (d) 1.6 eV (e) 2.2 eV (f) 3.2 eV of the chain with surface modulation when the light is incident along the chain; theoretical distribution of the electromagnetic field intensity  $|E|^2$  at (g) 1.6 eV (h) 2.2 eV (i) 3.2 eV of the chain with surface modulation when the light is incident perpendicular to the chain direction; the electric field is greatly enhanced around the plasmonic resonance energy both from the simulation and experiment result. Beyond or below the resonant energy, the electric field is not as strong as at the resonance energy. The arrow in the figures indicates the polarization direction.

### 3.6 Summary

In this chapter, a new fabrication approach was developed to synthesize self-organized 1D Au nanoparticle arrays encapsulated within freestanding SiO<sub>2</sub> nanowires by Au-enhanced oxidation of Au-coated surface-modulated Si nanowires. This technique leads to a versatile platform for creating Au nanoparticle arrays with highly tailorable and controllable particle diameters and interparticle spacings. Specifically, the final Au nanoparticle diameter is determined by the starting diameter of the Si nanowire and Au film thickness, while the interparticle spacing is controlled by the modulation wavelength of starting Si nanowire.

The plasmonic properties of the fabricated arrays with 80nm diameter particles and 230nm interparticle spacing was confirmed from optical extinction measurements of a randomly oriented ensemble of wires. A strong plasmonic peak was observed at a wavelength of 550 nm, which agrees well the spectrum obtained by FDTD simulation. This corresponds to the uniform green color in the far-field scattering images of individual 1D nanoparticle arrays. EELS and STEM confirmed the plasmonic response of the individual nanoparticles in the array, while EFTEM measurements showed weak coupling between nanoparticles along the array.

### 3.7 References

- 1 Kim, D. K. *et al.* Plasmonic Properties of the Multispot Copper-Capped Nanoparticle Array Chip and Its Application to Optical Biosensors for Pathogen Detection of Multiplex DNAs. *Anal Chem* **83**, 6215-6222 (2011).
- 2 Osberg, K. D. *et al.* Dispersible Gold Nanorod Dimers with Sub-5 nm Gaps as Local Amplifiers for Surface-Enhanced Raman Scattering. *Nano Lett* **12**, 3828-3832 (2012).
- 3 Maier, S. A., Kik, P. G. & Atwater, H. A. Optical pulse propagation in metal nanoparticle chain waveguides. *Phys Rev B* **67** (2003).
- 4 Maier, S. A., Kik, P. G. & Atwater, H. A. Observation of coupled plasmon-polariton modes in Au nanoparticle chain waveguides of different lengths: Estimation of waveguide loss. *Appl Phys Lett* **81**, 1714-1716 (2002).

- 5     Otte, M. A., Estevez, M. C., Regatos, D., Lechuga, L. M. & Sepulveda, B. Guiding Light in Monolayers of Sparse and Random Plasmonic Meta-atoms. *Acs Nano* **5**, 9179-9186 (2011).
- 6     Mayshev, A. V., Malyshev, V. A. & Knoester, J. Frequency-controlled localization of optical signals in graded plasmonic chains. *Nano Lett* **8**, 2369-2372 (2008).
- 7     Pavlov, R. S., Curto, A. G. & van Hulst, N. F. Log-periodic optical antennas with broadband directivity. *Opt Commun* **285**, 3334-3340 (2012).
- 8     Dintinger, J., Muhlig, S., Rockstuhl, C. & Scharf, T. A bottom-up approach to fabricate optical metamaterials by self-assembled metallic nanoparticles. *Opt Mater Express* **2**, 269-278 (2012).
- 9     Dintinger, J. & Scharf, T. Plasmonic nanoparticles for a bottom-up approach to fabricate optical metamaterials. *Photonic and Phononic Properties of Engineered Nanostructures Ii* **8269** (2012).
- 10    Maier, S. A., Brongersma, M. L., Kik, P. G. & Atwater, H. A. Observation of near-field coupling in metal nanoparticle chains using far-field polarization spectroscopy. *Phys Rev B* **65** (2002).
- 11    Solis, D. *et al.* Turning the Corner: Efficient Energy Transfer in Bent Plasmonic Nanoparticle Chain Waveguides. *Nano Lett* **13**, 4779-4784 (2013).
- 12    Zou, S. L., Janel, N. & Schatz, G. C. Silver nanoparticle array structures that produce remarkably narrow plasmon lineshapes. *J Chem Phys* **120**, 10871-10875 (2004).
- 13    Zou, S. L. & Schatz, G. C. Narrow plasmonic/photonic extinction and scattering line shapes for one and two dimensional silver nanoparticle arrays. *J Chem Phys* **121**, 12606-12612 (2004).
- 14    Huang, T., Cao, W., Elsayed-Ali, H. E. & Xu, X. H. N. High-throughput ultrasensitive characterization of chemical, structural and plasmonic properties of EBL-fabricated single silver nanoparticles. *Nanoscale* **4**, 380-385 (2012).
- 15    Yang, Y., Matsubara, S., Nogami, M., Shi, J. L. & Huang, W. M. One-dimensional self-assembly of gold nanoparticles for tunable surface plasmon resonance properties. *Nanotechnology* **17**, 2821-2827 (2006).
- 16    Kumar, A. *et al.* Benzene- and anthracene-mediated assembly of gold nanoparticles at the liquid-liquid interface. *Langmuir* **18**, 6478-6483 (2002).
- 17    Banks, D. P., Grivas, C., Mills, J. D., Eason, R. W. & Zergioti, I. Nanodroplets deposited in microarrays by femtosecond Ti : sapphire laser-induced forward transfer. *Appl Phys Lett* **89** (2006).
- 18    Kuznetsov, A. I. *et al.* Laser Fabrication of Large-Scale Nanoparticle Arrays for Sensing Applications. *Acs Nano* **5**, 4843-4849 (2011).
- 19    Kuznetsov, A. I. *et al.* Laser-induced transfer of metallic nanodroplets for plasmonics and metamaterial applications. *J Opt Soc Am B* **26**, B130-B138 (2009).
- 20    Deng, D. S., Nave, J. C., Liang, X., Johnson, S. G. & Fink, Y. Exploration of in-fiber nanostructures from capillary instability. *Opt Express* **19**, 16273-16290 (2011).
- 21    Gumennik, A. *et al.* Silicon-in-silica spheres via axial thermal gradient in-fibre capillary instabilities. *Nat Commun* **4** (2013).
- 22    Wang, D., Ji, R. & Schaaf, P. Formation of precise 2D Au particle arrays via thermally induced dewetting on pre-patterned substrates. *Beilstein J Nanotech* **2**, 318-326 (2011).
- 23    Lin, C. H. *et al.* A method to fabricate 2D nanoparticle arrays. *Appl Phys a-Mater* **98**, 855-860 (2010).
- 24    Hu, W. C. *et al.* Lithography-Free Synthesis of Freestanding Gold Nanoparticle Arrays Encapsulated Within Dielectric Nanowires. *Proc Spie* **7610** (2010).

- 25 Kolb, F. M. *et al.* Periodic chains of gold nanoparticles and the role of oxygen during the growth of silicon nanowires. *Appl Phys Lett* **89** (2006).
- 26 Karim, S. *et al.* Morphological evolution of Au nanowires controlled by Rayleigh instability. *Nanotechnology* **17**, 5954-5959 (2006).
- 27 Nichols, F. A. & Mullins, W. W. Morphological Changes of a Surface of Revolution Due to Capillarity-Induced Surface Diffusion. *Journal of Applied Physics* **36**, 1826-& (1965).
- 28 Nichols, F. A. & Mullins, W. W. Surface- (Interface-) and Volume-Diffusion Contributions to Morphological Changes Driven by Capillarity. *T Metall Soc Aime* **233**, 1840-& (1965).
- 29 Karim, S. *et al.* Influence of crystallinity on the Rayleigh instability of gold nanowires. *J Phys D Appl Phys* **40**, 3767-3770 (2007).
- 30 Powers, J. D. & Glaeser, A. M. Orientation effects on the high-temperature morphological evolution of pore channels in sapphire. *J Am Ceram Soc* **83**, 2297-2304 (2000).
- 31 Wang, Y. T., Teitel, S. & Dellago, C. Effect of surface structure on shape transformations of gold nanorods. *J Comput Theor Nanos* **4**, 282-290 (2007).
- 32 Wagner, R. S. & Ellis, W. C. Vapor-Liquid-Solid Mechanism of Single Crystal Growth ( New Method Growth Catalysis from Impurity Whisker Epitaxial + Large Crystals Si E ). *Appl Phys Lett* **4**, 89-& (1964).
- 33 Henson, J., DiMaria, J. & Paiella, R. Influence of nanoparticle height on plasmonic resonance wavelength and electromagnetic field enhancement in two-dimensional arrays. *Journal of Applied Physics* **106**, 093111 (2009).
- 34 Auguié, B. & Barnes, W. L. Diffractive coupling in gold nanoparticle arrays and the effect of disorder. *Opt Lett* **34**, 401-403 (2009).
- 35 Burrows, C. P. & Barnes, W. L. Large spectral extinction due to overlap of dipolar and quadrupolar plasmonic modes of metallic nanoparticles in arrays. *Opt Express* **18**, 3187-3198 (2010).
- 36 Rodríguez-Fernández, J., Pérez-Juste, J., García de Abajo, F. J. & Liz-Marzán, L. M. Seeded growth of submicron Au colloids with quadrupole plasmon resonance modes. *Langmuir* **22**, 7007-7010 (2006).
- 37 Zou, S. L. & Schatz, G. C. Theoretical studies of plasmon resonances in one-dimensional nanoparticle chains: narrow lineshapes with tunable widths. *Nanotechnology* **17**, 2813-2820 (2006).
- 38 Schaffer, B., Grogger, W., Kothleitner, G. & Hofer, F. Comparison of EFTEM and STEM EELS plasmon imaging of gold nanoparticles in a monochromated TEM. *Ultramicroscopy* **110**, 1087-1093 (2010).
- 39 Chu, M. W. *et al.* Probing Bright and Dark Surface-Plasmon Modes in Individual and Coupled Noble Metal Nanoparticles Using an Electron Beam. *Nano Lett* **9**, 399-404 (2009).
- 40 Schaffer, B., Hohenester, U., Trugler, A. & Hofer, F. High-resolution surface plasmon imaging of gold nanoparticles by energy-filtered transmission electron microscopy. *Phys Rev B* **79** (2009).
- 41 Koh, A. L., Fernandez-Dominguez, A. I., McComb, D. W., Maier, S. A. & Yang, J. K. W. High-Resolution Mapping of Electron-Beam-Excited Plasmon Modes in Lithographically Defined Gold Nanostructures. *Nano Lett* **11**, 1323-1330 (2011).
- 42 Bohren, C. F. & Huffman, D. R. *Absorption and scattering of light by small particles*. (John Wiley & Sons, 2008).
- 43 Guiton, B. S. *et al.* Correlated Optical Measurements and Plasmon Mapping of Silver Nanorods. *Nano Lett* **11**, 3482-3488 (2011).



- 44 de Abajo, F. J. G. Optical excitations in electron microscopy. *Rev Mod Phys* **82**, 209-275 (2010).
- 45 Babayan, Y. *et al.* Confining standing waves in optical corrals. *Acs Nano* **3**, 615-620 (2009).
- 46 Girard, C. Near fields in nanostructures. *Rep Prog Phys* **68**, 1883 (2005).

## **Chapter 4**

### **Dual-band Optical Nanoantenna with Nanoring Load**

In this chapter, a nanoring element is used to load a dimer nanoantenna for dual-band operation. Far-field scattering measurements of a nanofabricated structure show that the nanoantenna has two independent resonances within the visible regime. The origin of dual-band behavior was explored by simulating the electric field, magnetic field, and charge distribution at the center wavelength of the two resonances. The results show that the properties are induced by the independent or collective oscillatory radiation behavior of the nanoring and nanoparticle components of the antenna. The charge distribution on the antenna reveals that the long-wavelength resonances corresponds to the coupled state, while the short-wavelength resonance is due to the decoupled state.

The design optimization was conducted by Dr. Anastasios H. Panaretos under the guidance of Prof. Douglas H. Werner in the Electrical Engineering Department.

#### **4.1 Background and Motivation**

Optical nanoantennas have the potential to provide communication between nano- and micro-scale devices, and to convert light to electric power. Similar to the radio frequency (RF) antenna, which converts electromagnetic waves at RF frequency into direct current electricity<sup>1</sup>, nanoantennas can be engineered to absorb light of specific wavelengths that are comparable to their dimensions. Nanoantenna arrays of optimized geometry can efficiently absorb light with wavelengths from 0.4 $\mu\text{m}$  to 1.6 $\mu\text{m}$ , which make up 85% of the solar radiation spectrum<sup>2</sup>. They can also be used to encode information at high frequencies. This paves the way for realizing optical nanocircuits<sup>3</sup>, all-optical wireless communications<sup>4,5</sup> and optical data storage.

Similar to their RF counterparts, the ability to flexibly design nanoantennas for operation in the optical frequency domain is essential for their application in both receiving and transmission modes. The optical nanoantenna is typically realized using plasmonic structures, including nanorods/nanospheres<sup>6-9</sup>, nanoparticle/nanorod dimers<sup>10-13</sup>, bow-tie nanoantennas<sup>14,15</sup> and Yagi-Uda nanoantennas<sup>16-20</sup>. The localized surface plasmon resonance (LSPR) of these structures enables strong near-field and far-field diffractive coupling that leads to additional promising applications, including biological sensors<sup>21</sup>, photovoltaic enhancement<sup>22-24</sup>, and metamaterials<sup>25,26</sup>.

Extensive effort has been invested in developing theoretical models to describe optical nanoantennas fabricated from plasmonic structures. Lumped circuit analysis methods<sup>27-31</sup> provide a simple but useful approach to design and optimize nanoantennas by varying the input impedance loading. Coupled oscillator models<sup>32</sup> provide physical insight into the underlying physical mechanism by modeling the plasmonic resonance with a simple mass-spring model. Fabry-Perot models<sup>33,34</sup> connect optical nanoantennas to their RF counterparts by considering the Eigen modes of the plasmonic structures. The optical properties of experimental nanoantennas have been tailored by either adjusting the geometry of the nanoparticle<sup>35-38</sup> or by properly loading the lumped circuit with capacitive, inductive, or resistive plasmonic elements<sup>27-29,31</sup>. However, previous research has largely focused on studying single-band nanoantennas in the visible regime.

In this research, a dual-band optical nanoantenna is proposed and demonstrated by loading a gold (Au) nanoparticle dimer antenna with a properly designed plasmonic nanoring. The extinction spectrum of the fabricated structure exhibits two well-separated resonances in the visible wavelength regime that agree well with theoretical predictions. The two resonances correspond to states in which the two components of the nanoantenna radiate either independently or collectively. This is confirmed by simulating the electric field, magnetic field and charge distribution at the two resonant wavelengths.

## 4.2 Design Optimization

A ring-loaded dimer nanoantenna was selected to realize a dual-band nanoantenna in the visible regime because of its larger radiation efficiency and flexible design<sup>10,39,40</sup>. Theoretical calculations and experimental results on individual nanorings<sup>41</sup> have indicated that variations in the inner ring radius of a nanoring shifts the resonance peak position of the structure. Although plasmonic nanorings are traditionally described using mode hybridization models, it can be shown that rings can be modeled as homogeneous disks characterized by effective dielectric properties similar to those of a medium governed by the Maxwell-Garnett mixing rule. Therefore, nanoring loading elements can be used to adjust the nanoantenna response. This dissertation examines the design flexibility that can be achieved by ring-loading an individual optical dimer nanoantenna with large radiation efficiency.

Nanoantenna design optimization was performed by fixing the diameter and the height of the dimer nanoantenna particles (120nm/30nm), the outer diameter and height of the nanoring structure (100nm/30nm), and the air gap between the nanoring and the dimer particles (10nm), as illustrated in Figure 4-1 (a). These geometries are much smaller than the wavelength of incident light, thereby ensuring a strong interaction between the incident radiation and the nanoantenna. The inner radius of the nanoring optimized to tailor the resonance frequency of the structure. For consistency with the fabricated structure, the modeled ring-loaded nanoantenna was placed on infinitely thick fused silica substrate. The simulation included the dispersive optical properties of the deposited Au film as determined by spectroscopic ellipsometry measurements of a witness sample deposited using the same conditions as the nanoantenna structure.

Simulated scattering spectra of the ring-loaded dimer nanoantennas with inner diameter radius ranging from 10nm to 40nm are shown in Figure 4-1 (b). These simulations reveal that the nanoantenna structure has two resonance peaks in the visible wavelength regime, and that their

center wavelength and bandwidth are strongly dependent on the inner ring dimensions. Specifically, as the ring radius is increased from 10nm to 35nm, the short-wavelength resonance center wavelength shifts from 583nm to 626nm, while its bandwidth increases from 37nm to 69nm (Lorentz function curve fit). The long-wavelength resonance has a stronger dependence on the ring radius, with its center wavelength shifting from 770nm to 950nm, and its bandwidth decreasing from 213nm to 142nm.

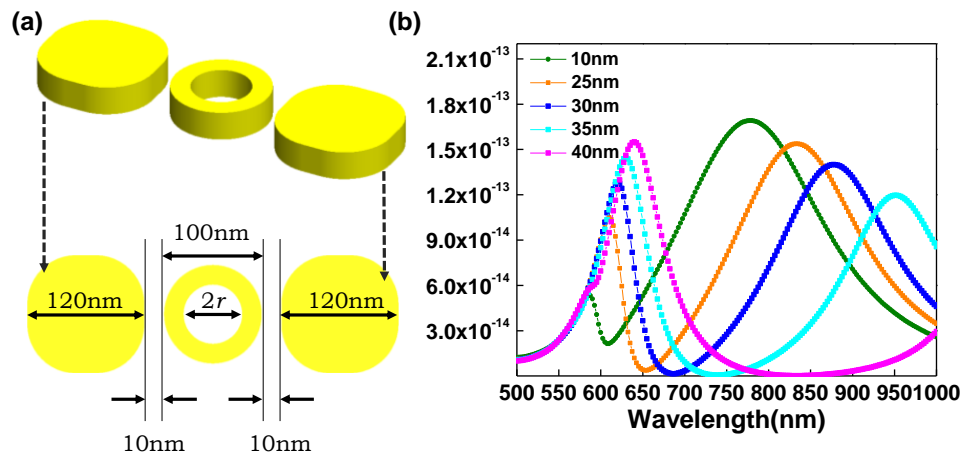


Figure 4-1. (a) Schematic illustration of the dimer nanoantenna loaded with a nanoring; (b) The simulated scattering spectrum of the nanoring-loaded nanoantenna with different inner ring radius.

The monotonic redshift in the resonance peak positions with increasing inner nanoring radius allows the dual-band properties of the nanoantenna to be optimized over a wide range by simply changing this single design parameter. The redshift of in the center-wavelength of both resonances is caused by the enhanced interaction between the nanoring load and the dimer particle nanoantenna as the wall thickness (the difference of the outer and inner ring radius) of the ring decreases. In contrast, the bandwidth of the short-wavelength resonance increases, while that of the long-wavelength resonance decreases with increasing wall thickness. This can be explained by considering the origin of the two resonances. The short-wavelength resonance corresponds to the

scattering resonance of each half of the nanoparticle dimer antenna, while the long-wavelength resonance corresponds to the case when the three particles scatter as a longer effective homogeneous particle. As the inner radius of the ring becomes smaller, the coupling between the left and right nanoparticles decreases. Therefore, the bandwidth of the short wavelength resonance is maximized in the limit when the inner radius equals the outer radius, and the ring vanishes. For the long-wavelength resonance, the bandwidth of the long-wavelength resonance is related to the effective volume of the homogenous three-particle structure. The bandwidth of this resonance decreases with decreasing effective volume, which occurs when inner radius of the ring increases.

This sensitive control over the center-wavelength and bandwidth of the two resonances makes it possible to optimize the ring-loaded dimer nanoantenna to have desired resonant properties at designated wavelengths. To experimentally demonstrate this design flexibility, nanoantennas with high scattering cross sections in the visible regime were fabricated and characterized.

### 4.3 Fabrication Process Optimization

Optimized ring-loaded and unloaded dimer nanoantennas were fabricated using a conventional top-down electron-beam lithography and metal lift-off process. First, a 150nm thick electron-beam resist layer (Nippon Zeon ZEP 520A diluted by 50% with Anisole) was spun on a cleaned fused silica wafer at a speed of 5000 revolution per minutes (RPM) for 45sec. The resist was soft-baked at 180°C for 3min, and the features were exposed at a dose of 190 $\mu$ C/cm<sup>2</sup> (Vistec EBPG 5200, spot size 7nm and beam current 1nA). The electron beam resist layer was developed at -10°C in n-Amyl Acetate for 2min and then MIBK: IPA= 8:1 for 1min. Cold development increased the contrast of the resist, which was required to reproducibly fabricate the ring-loaded nanoantenna structures with sub-10nm control over feature dimensions. After lithographic patterning, the nanoantenna structures were completed by electron-beam evaporating the Ti/Au

(1nm/30nm) metal and lifting-off the deposited metal film by dissolving the resist in Microposit Remover 1165 (Microchem).

Lithographic patterning of the nanoantennas with the designed dimensions is difficult to optimize due to backscattering of high energy electrons, and the resulting proximity effect<sup>42</sup>. To enable the required control, the exposure conditions were simulated (Layout Beamer, Genlsys) to

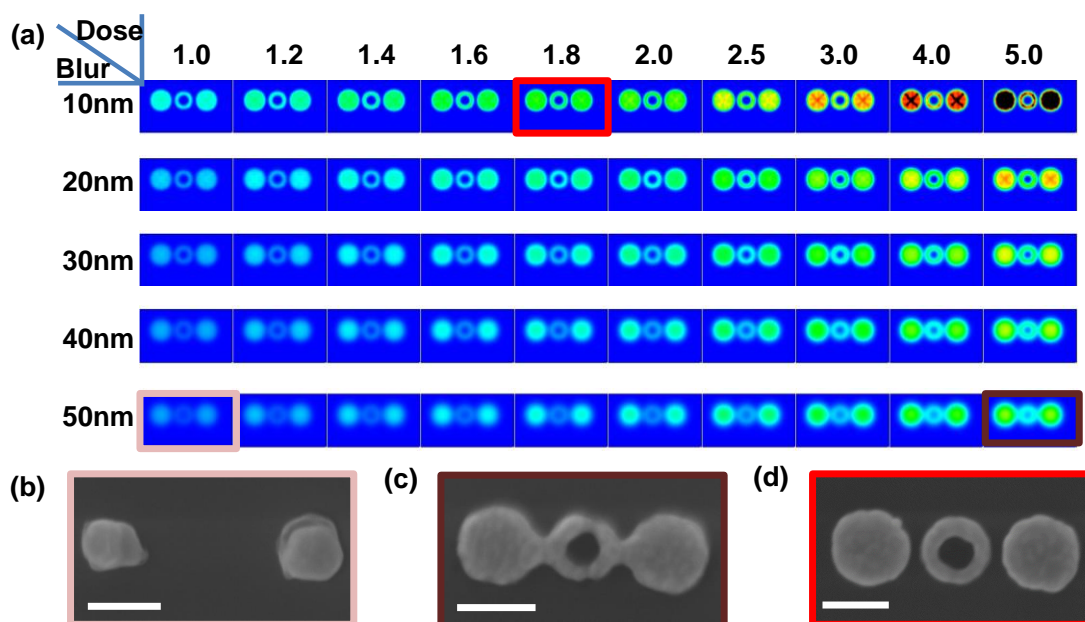


Figure 4-2. (a) Process simulation results for the nanoring-loaded dimer antenna with specific dose and process blur; FESEM images of the nanoring-loaded nanoantenna written with high process blur and low dose (b), high process blur and high dose (c) and low process blur and intermediate dose (d). Scale bar: 100nm.

correct for the proximity effects. The relative exposure dose and process blur were varied in the simulation to find optimized process conditions. Figure 5-2 (a) shows the intensity images after exposure for a relative dose that varies from 1.0 to 5.0 and a process blur between 10nm and 50nm. The simulation results show that intermediate dose and lowest blur gave the highest contrast between the exposed and unexposed regions, especially within the gap region that has the strongest

proximity effect. In contrast, the lowest dose and highest blur showed little contrast variation between the nanoring and nanoparticle regions. The highest dose and highest blur resulted in a caused the three particles to merge into a single particle without gaps.

Figure 4-2 (b) and (c) display FESEM images of the nanoantenna structures patterned with a process blur and dose of 50nm:120 $\mu\text{C}/\text{cm}^2$  and 50nm:270 $\mu\text{C}/\text{cm}^2$ , and developed at room temperature. Figure 4-2(b) shows that the nanoring load is completely missing at the highest blur of 50nm and the lowest 120  $\mu\text{C}/\text{cm}^2$  dose, which is consistent with the simulation result highlighted in pink. In contrast, Figure 4-2(c) shows that the highest process blur of 50nm and highest dose of 270 $\mu\text{C}/\text{cm}^2$  causes the gap to disappear entirely, connecting the nanoring load to the dimer nanoparticle antenna, which is highlighted in dark red. Figure 4-2(d) shows the optimized process at the lowest blur of 10nm and an intermediate dose of 190 $\mu\text{C}/\text{cm}^2$ . The pattern was developed at -10°C to increase the contrast of the resist<sup>43-45</sup> and decrease the process blur. The air gap between the nanoring and nanoparticles is resolved, and the target dimensions are achieved, which is consistent with the simulation result marked in red. This demonstrates that it is necessary to reduce the process blur and optimize the expose dose to fabricate the nanoring-loaded nanoantenna structure.

Nanoantennas with three different load configurations were fabricated to systematically study the impact of ring-load structure on the resultant optical properties, including an air load (unloaded), a solid nanoparticle load, and a nanoring load. Figure 4-3 (a-c) shows FESEM images of the nanofabricated structures. The fabricated particles are not ideal cylinders because of line edge roughness in the patterning process, the finite grain size of the deposited Au film, and the sidewall angle from the metal deposition. The dimensions used for simulations are estimated by approximating the particles geometry by ideal cylinders. For the air-loaded structure in Figure 4-3 (a), the dimer particle diameter and gap spacing are 116nm and 124nm as compared to the designed values of 120nm diameter and 120nm. The fabricated dimer and load particles in the solid



nanoparticle load structure in Figure 4-3 (b) were 120nm and 100nm in diameter as compared to the 118nm and 98nm of the designed structure. The gap in the fabricated structure is 6nm larger than the designed structure. For the ring load, the right and left nanoparticle diameters were 121nm and 123nm with particle to ring separation of 14nm and 16nm, respectively. The outer ring diameters were 10nm larger than the design target. The difference between the optimized designed values and the fabricated sample were integrated into the model that compares the experimentally measured response to theory.

#### 4.4 Far-Field Scattering Measurement and Simulation

Far-field scattering measurements were performed to evaluate the optical properties of an individual optical nanoantenna with different loading conditions. The spectra were collected using an upright microscope (Nikon TE 200U). The unpolarized white light from a tungsten-halogen lamp was passed through an oil dark-field condenser with (NA=1.2-1.43) to illuminate the optical nanoantennas in the transmission mode. The light scattered from individual nanoantennas was collected with a 100 $\times$  objective lens, and the scattered light spectrum was analyzed using an imaging spectrometer (Andor, Sharmock 303) equipped with a 150L/mm grating. The contribution from the substrate was removed by subtracting the spectrum from an adjacent unpatterned region of equal size from the nanoantenna scattering spectrum. The intensity variation of the light source was accounted for by normalizing the corrected spectrum with the spectral intensity of the light source. The spectra of the three optical nanoantennas in Figure 4-3 (a-c) measured under identical conditions, are shown in Figure 4-3 (d-f). The air-loaded nanoantenna exhibits a single intense peak around 634nm. The peak in the scattered spectrum of the solid load nanoantenna is red-shifted by 43nm relative to the air load structure, and its width is broadened by 41nm. The red-shift and peak broadening is due to the coupling between the solid load and the dimer nanoantenna. For the ring-

loaded nanoantenna, two peaks at 666nm and 884nm with bandwidths of 66nm and 190nm are observed in the spectrum, consistent with the previous numerical result for this structure.

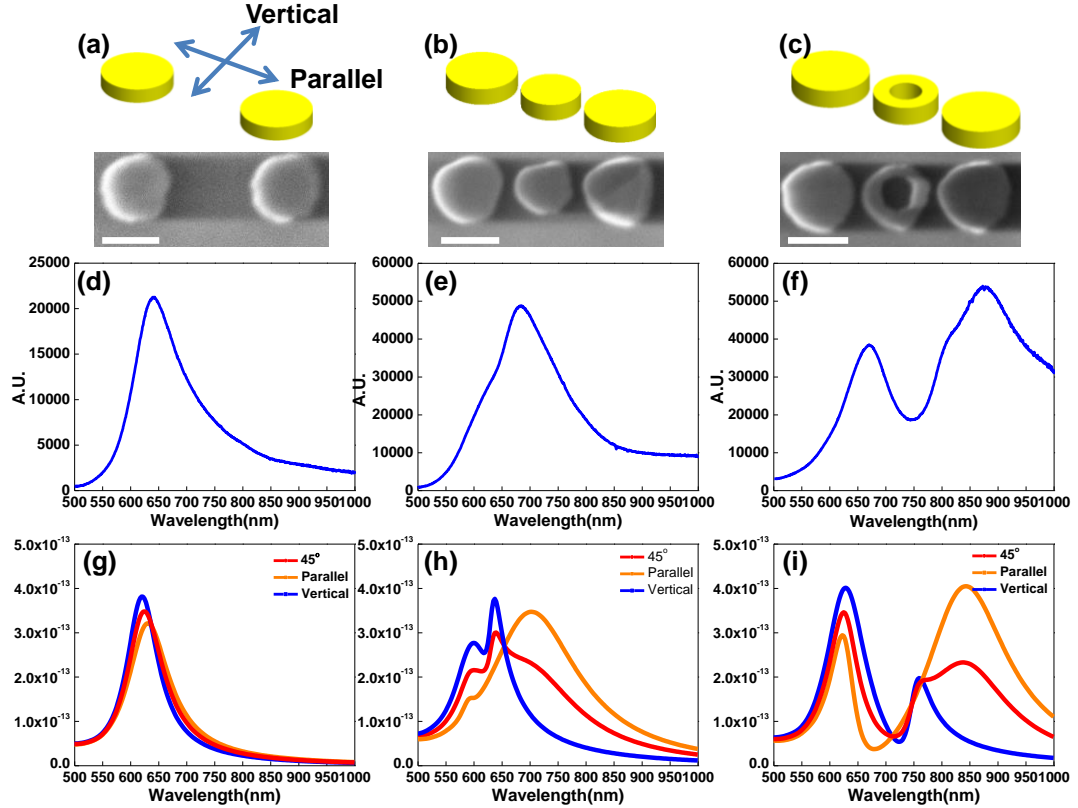


Figure 4-3. The schematic and FESEM images of the fabricated nanoantenna with air load (a), solid load (b), nanoring load (c). Scale bar: 100nm; Far-field scattering measurement result for the nanoantenna with air load (d), solid load (e), nanoring load (f) under unpolarized light excitation; Far-field scattering simulation result for the nanoantenna with air load (g), solid load (h), nanoring load (i) under 0°(Orange), 45°(red) and 90°(Blue) polarized light excitation under 0°(Orange), 45°(red) and 90°(Blue) polarized light excitation.

Electromagnetic simulations were performed to understand the physical mechanisms responsible for the different optical responses of the three nanoantennas. The actual measured dimensions of the fabricated nanoantenna structures were used in the simulation to accurately compare experiment and theory. The scattering spectra were simulated by illuminating the structure

at normal incidence with a linearly polarized plane wave at three different polarizations ( $0^\circ$ ,  $45^\circ$ ,  $90^\circ$ ) with respect to the long axis of the nanoantenna. The antenna modes are excited when the field is aligned parallel to the long axis of the nanoantenna, while the individual particle modes are excited when the field is aligned perpendicular to the long axis. Thus, the spectra measured using unpolarized light are most accurately modeled by the  $45^\circ$  polarized plane wave response.

For the air-loaded nanoantenna, a single peak is observed for all three polarizations, as shown in Figure 4-3 (g). This peak is the characteristic resonance of the dimer nanoantenna, and its position is slightly blue-shifted when the polarization is changed from parallel to perpendicular. This shift is due to the differences in electromagnetic coupling. Specifically, although the coupling is weak in both cases, the parallel polarized light provides stronger coupling between the dimer particles than the perpendicular polarization (see Section 4.5 and Section 4.6 for details). The peak position and bandwidth of the unpolarized simulated response agree well with the measured results in Figure 4-3 (d).

There is a significant difference in the optical response of the solid-load nanoantenna under the three different polarizations, as shown in Figure 4-3 (h). When the field of the illumination is parallel to the long-axis of the nanowire, there is a strong lateral coupling between the dimer particles and the load. This results in a nanoantenna that can be modeled as a homogeneous particle with longer effective electromagnetic length. This causes a redshift of 67nm in the peak position compared to the air-loaded nanoantenna. In contrast, when the nanoantenna is illuminated with the perpendicular polarization, the elements behave as if they are independent. This results in two narrow-band peaks that correspond to an interaction with the dimer particles and the solid load, as shown in Figure 4-3(h). The peak at 640nm is induced by the resonance of the individual dimer particles, which is consistent with the air-loaded nanoantenna. The peak at 594nm is caused by the resonance of the solid load nanoparticle, which has a smaller diameter and shorter resonance wavelength. The spectrum for illumination with light polarized at  $45^\circ$  shows an average of the

parallel and vertical polarizations due to the partial coupling of the elements. The experimentally measured spectrum for unpolarized light in Figure 4-3 (e) has strong qualitative agreement with the modeled results, showing a broad peak that is a convolution of the two narrow-band peaks found in the simulation. These two loading scenarios correspond to the two limiting scattering states that this structure can support. In particular, the air-load nanoantenna represents the state where the dimer particles are decoupled and scatter individually. When the solid nanoparticle load is added, the coupled state of the particles is established, and the structure exhibits a red-shifted resonance.

The scattering spectrum of the nanoring-loaded antenna is significantly different from the other two loading cases. The simulated scattering spectrum in Figure 4-3(i) shows a multi-band behavior with two separate peaks for both parallel and perpendicular excitation. For parallel excitation, the structure exhibits two distinct extinction peaks. From the resonant wavelengths and bandwidth, these peaks can be attributed to the coupled and decoupled states of the nanoantenna. The longer wavelength peak at 850nm corresponds to the coupled state of the nanoantenna, while the short wavelength peak at 650nm is induced by the decoupled state of the nanoantenna. In contrast to the solid load case, the two resonance peaks are of similar intensity and are well separated in wavelength from one another. For the perpendicular excitation, the two extinction peaks correspond to the resonances of the nanoring and dimer particles. The peak at 630nm is due to the resonance of individual dimer particles, which is consistent with the air-loaded nanoantenna. The resonance at 750nm is induced by nanoring. The strong coupling between the inner and outer wall of the nanoring reduces its resonance energy and increases its resonance wavelength compared to a solid nanoparticle. The experimentally measured spectrum for unpolarized illumination shown in Figure 4-3 (f) can be approximated as an average of the parallel and perpendicular polarizations, which includes contributions from both polarizations. The electric field, magnetic field, and charge distribution of the nanoantennas with different loads were studied to elucidate the origin of the multi-peak behavior, as discussed in Sections 4.5 and 4.6.

#### 4.5 Electric and Magnetic Field Distribution

The electric and magnetic field distribution on the nanoantennas were modeled under normal incidence illumination using finite element electromagnetic simulation (COMSOL Multiphysics 4.4, RF Module) with the field parallel to the long axis of the antenna because this is the only condition that excites the antenna modes. The normalized field quantities determined at the resonant wavelengths for all three cases are plotted in Figure 4-4.

The electric field distribution for the air-load case, which is shown in Figure 4-4 (a), is a typical distribution found for a resonating dipole, and consists of a high field intensity surrounding the pole of the particle plane. The magnetic field circulates around the two particles, and has high intensity along their periphery, as shown in Figure 4-4 (e). The field distribution is symmetric with respect to the symmetry plane of the particles, and it is maximum along the center of the long-axis of the nanoantenna. This indicates that the coupling between the particles is small, and thus they radiate independently. However, because the two particles are identical, their resonances occur at the same wavelength, and thus the optical response has a single resonance peak.

The solid nanoparticle load nanoantenna exhibits a much stronger coupling between the loading element and the dimer particles relative to the air loaded structure because of the small separation between the antenna and load elements. As shown in Figure 4-4 (b), the electric field enhancement is clearly visualized in the air gap, indicating that the solid particles and dimer nanoantenna function collectively. In this case, the magnetic field circulates around all three particles, as shown in Figure 4-4 (f). In addition, the circulation of the magnetic field around each particle is synchronized, which is equivalent to a magnetic field that circulates around an effective homogeneous particle. Due to the strong coupling between the solid load and the dimer nanoantenna, the magnetic field distribution around them is not symmetric with respect the center axis, but is instead focused near the center particle. This coupling between the nanoantenna and

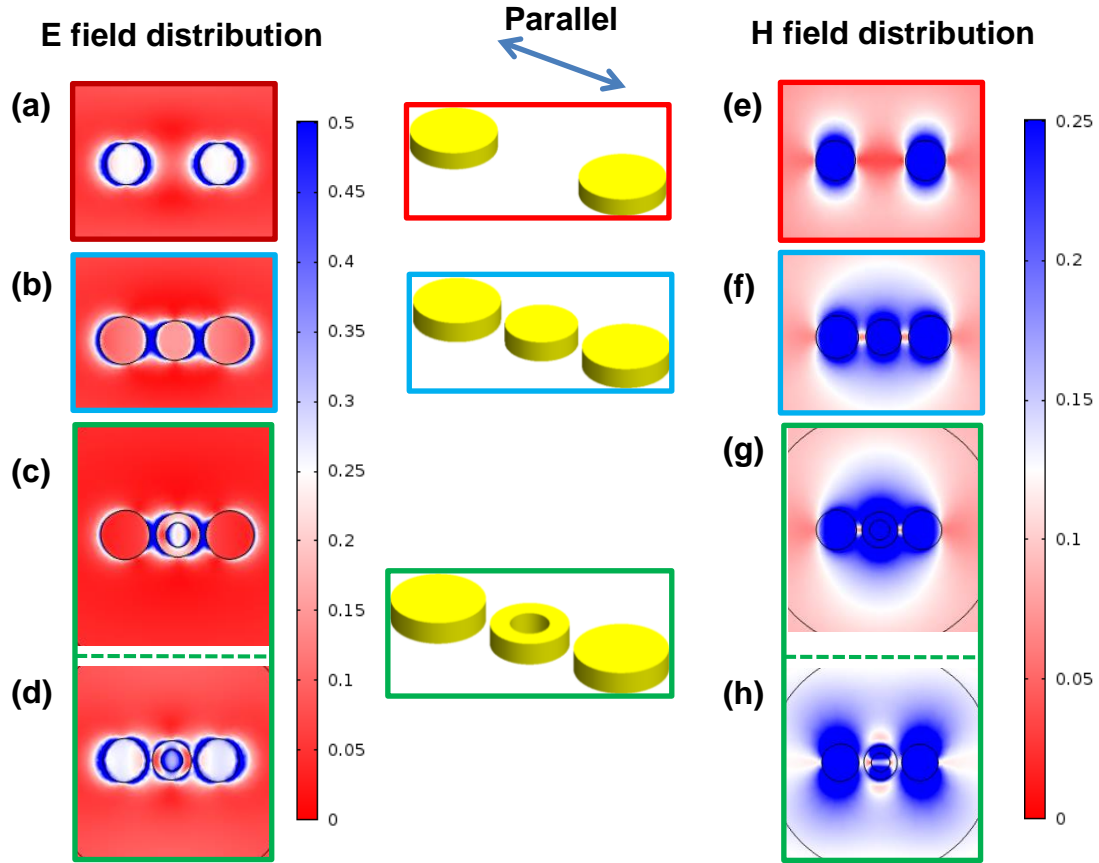


Figure 4-4. (a) The electric field and (e) magnetic field distribution of the fabricated nanoantenna with air load under parallel polarization excitation; (b) The electric field and (f) magnetic field distribution of the fabricated nanoantenna with solid load under parallel polarization excitation; (c) The electric field and (g) magnetic field distribution of the fabricated nanoantenna with nanoring load at longer wavelength peak around 850nm under parallel polarization excitation; (d) The electric field and (h) magnetic field distribution of the fabricated nanoantenna with nanoring load at short wavelength peak around 650nm under parallel polarization excitation.

load results in a collective oscillation across the three particle structure, inducing a redshift in the peak position relative to the air-load.

The field distribution for the nanoring-loaded nanoantenna was computed at the two resonant wavelengths of the nanostructure. As shown in Figure 4-4 (c), the electric field distribution for the long wavelength resonance of the nanoring loaded antenna exhibits an even stronger coupling between the nanoring and the dimer particles than the solid load structure. This indicates

that the ring and nanoantenna oscillate as an effective homogeneous particle. Figure 4-4 (g) shows that the magnetic field circulates around the outer particles and is the highest near the center ring-load particle. Similar to the solid-load case, this can be modeled as a magnetic field circulating around a homogeneous particle with a longer effective electromagnetic length. In this case, the coupling is much stronger than the solid load, and thus the resonance is red-shifted to a significantly longer wavelength than the solid load antenna.

An entirely different field distribution occurs at the short-wavelength resonance of the nanoring-loaded antenna. The electric field distribution plotted in Figure 4-4 (d) shows that the field is more concentrated around the dimer particles than the nanoring load. The electric field in the gap also has much lower intensity than the long-wavelength resonance. The magnetic field plot, which is shown in Figure 4-4 (h), demonstrates that the rotation around the nanoring is opposite to the rotation around the two outer particles. In addition, the magnetic field that circulates around the nanoring is weaker than the field around outer dimer particle elements. Therefore, the electromagnetic response of the center nanoring particle and the outer dimer nanoparticle are decoupled from one another, and the optical response of the nanoring-loaded nanoantenna is dominated by the response due to the outer dimer nanoparticles.

The electric and magnetic field distributions discussed in this section provide a physical interpretation for the characteristic properties of both the measured and the simulated scattering spectra for the three different nanoantenna loads. The analysis shows the importance of the load particle design in the coupled and decoupled state of nanoantenna elements, which can be tailored to create single-band or multi-band nanoantennas.

#### 4.6 Charge Distribution

The charge distribution on the nanoantennas when the incident field is parallel to the long axis of the antenna was studied to explore the origin of the plasmonic resonance behavior for the air-load, solid-load, and ring-loaded dimer structures. The distribution for the air-load, which is shown Figure 4-5 (a), demonstrates that the positive and negative charge is symmetrically distributed around the long axis of the nanoantenna. This is similar to the distribution found for a charge balanced dipole element, and further confirms the small degree of coupling between the dimer particles in the nanoantenna.

As shown in Figure 4-5 (b), the charge that is induced on each particle in the solid-load nanoantenna resembles the distribution found on nanoparticles with aligned dipoles, following a  $(+- +- +-)$  alignment. This lowers the resonance energy of the structure, and leads to a redshift in the scattering peak. The higher electric field intensity within the gap between the dimer and load elements also affects the charge distribution on the dimer particles. Specifically, the charge is unevenly distributed on the dimer particles, and is more concentrated near the solid load particle than at the outer periphery of the particles.

The nanoring-loaded nanoantenna has different charge distributions at the long and short wavelength resonances, as shown in Figure 4-5 (c) and (d). The aligned dipole  $(+- +- +-)$  charge distribution is similar to the solid load case, but even more concentrated near the ring load. This results in a structure with a longer effective nanoantenna length, which lowers its resonance energy with respect to the solid load structure. In this case, the increased charge imbalance on the dimer particles compared to the solid particle load is due to the stronger coupling with the nanoring load. At short wavelengths, the charge distribution on the nanoring is inverted with respect to the charge on the dimer particles, leading to a  $(+- -+ +-)$  pattern. This results in a more balanced charge distribution on dimer particles. The repulsive force decouples the dimer and nanoring particles,



thereby increasing the resonance energy of the structure. In this case, the resonance response is dominated by the dimer particles.

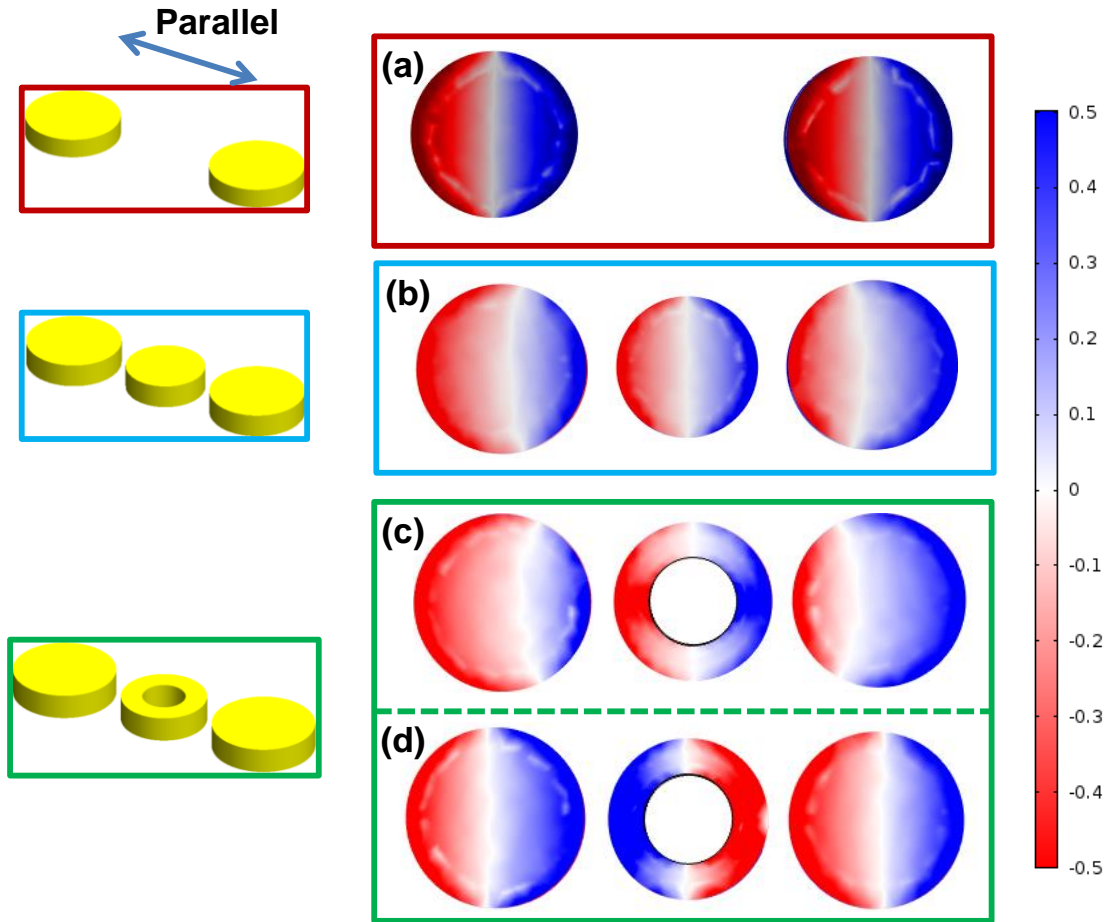


Figure 4-5. (a) The charge distribution of the fabricated nanoantenna with air load under parallel polarization excitation; (b) The charge distribution of the fabricated nanoantenna with solid load under parallel polarization excitation; (c) The charge distribution of the fabricated nanoantenna with nanoring load at longer wavelength peak around 850nm under parallel polarization excitation; (d) The charge distribution of the fabricated nanoantenna with nanoring load at short wavelength peak around 650nm under parallel polarization excitation.

#### 4.7 Summary

In this chapter, air-loaded, solid nanoparticle-loaded and nanoring-loaded dimer nanoantennas were studied to tailor the scattering properties of the structure. It was shown that the nanoring load element can be optimized to achieve a multi-band scattering response, which is not possible for the air load and solid nanoparticle load structures. The three types of nanoantennas were fabricated by electron-beam patterning followed by metal lift-off. Simulation was used to optimize the process parameters to achieve the tight dimensional tolerances on the nanoparticles and gaps with resolution down to 10 nm. The optical properties of the fabricated nanoantennas were characterized by far-field scattering measurements. The measured plasmonic response of all three structures, including the peak positions and bandwidth, exhibited strong qualitative agreement with simulation. The origin of the multi-band scattering response of the nanoring-loaded antennas was explored by comparing the simulated electric field, magnetic field and charge distribution to the air load and solid load cases. The field and charge distributions revealed that the short-wavelength resonance occurred when the three particles in the nanoring loaded array were coupled, while the long-wavelength response occurred when the particles were decoupled. This research demonstrated that the nanoantenna scattering response can be engineered by tailoring the properties of the nanoparticle load.

#### 4.8 References

- 1 Graf, R. F. *Modern dictionary of electronics*. 7th edn, (Newnes, 1999).
- 2 Berland, B. Photovoltaic Technologies Beyond the Horizon: Optical Rectenna Solar Cell (National Renewable Energy Laboratory, U.S., 2009).
- 3 Adato, R., Yanik, A. A. & Altug, H. On Chip Plasmonic Monopole Nano-Antennas and Circuits. *Nano Lett* **11**, 5219-5226 (2011).
- 4 Zhao, Y. & Alu, A. Optical Nanoantennas and Their Applications. *Ieee Radio Wireless*, 58-60 (2013).

- 5 Alu, A. & Engheta, N. Wireless at the Nanoscale: Optical Interconnects using Matched Nanoantennas. *Phys Rev Lett* **104** (2010).
- 6 Mohammadi, A., Sandoghdar, V. & Agio, M. Gold nanorods and nanospheroids for enhancing spontaneous emission. *New J Phys* **10** (2008).
- 7 Anger, P., Bharadwaj, P. & Novotny, L. Enhancement and Quenching of Single-Molecule Fluorescence. *Phys Rev Lett* **96**, 113002 (2006).
- 8 Kuhn, S., Hakanson, U., Rogobete, L. & Sandoghdar, V. Enhancement of single-molecule fluorescence using a gold nanoparticle as an optical nanoantenna. *Phys Rev Lett* **97** (2006).
- 9 Rogobete, L., Kaminski, F., Agio, M. & Sandoghdar, V. Design of plasmonic nanoantennae for enhancing spontaneous emission. *Opt Lett* **32**, 1623-1625 (2007).
- 10 Alu, A. & Engheta, N. Hertzian plasmonic nanodimer as an efficient optical nanoantenna. *Phys Rev B* **78** (2008).
- 11 Pramod, P. & Thomas, K. G. Plasmon Coupling in Dimers of Au Nanorods. *Adv Mater* **20**, 4300-4305 (2008).
- 12 Ghenuche, P., Cherukulappurath, S., Taminiau, T. H., van Hulst, N. F. & Quidant, R. Spectroscopic mode mapping of resonant plasmon nanoantennas. *Phys Rev Lett* **101** (2008).
- 13 Muskens, O. L., Giannini, V., Sanchez-Gil, J. A. & Rivas, J. G. Strong enhancement of the radiative decay rate of emitters by single plasmonic nanoantennas. *Nano Lett* **7**, 2871-2875 (2007).
- 14 Fromm, D. P., Sundaramurthy, A., Schuck, P. J., Kino, G. & Moerner, W. E. Gap-dependent optical coupling of single "Bowtie" nanoantennas resonant in the visible. *Nano Lett* **4**, 957-961 (2004).
- 15 Schuck, P. J., Fromm, D. P., Sundaramurthy, A., Kino, G. S. & Moerner, W. E. Improving the mismatch between light and nanoscale objects with gold bowtie nanoantennas. *Phys Rev Lett* **94** (2005).
- 16 Curto, A. G. *et al.* Unidirectional Emission of a Quantum Dot Coupled to a Nanoantenna. *Science* **329**, 930-933 (2010).
- 17 Taminiau, T. H., Stefani, F. D. & van Hulst, N. F. Enhanced directional excitation and emission of single emitters by a nano-optical Yagi-Uda antenna. *Opt Express* **16**, 10858-10866 (2008).
- 18 Li, J. J., Salandrino, A. & Engheta, N. Shaping light beams in the nanometer scale: A Yagi-Uda nanoantenna in the optical domain. *Phys Rev B* **76** (2007).
- 19 Kosako, T., Kadoya, Y. & Hofmann, H. F. Directional control of light by a nano-optical Yagi-Uda antenna. *Nat Photonics* **4**, 312-315 (2010).
- 20 Dregely, D. *et al.* 3D optical Yagi-Uda nanoantenna array. *Nat Commun* **2** (2011).
- 21 Homola, J. Surface plasmon resonance sensors for detection of chemical and biological species. *Chemical reviews* **108**, 462-493 (2008).
- 22 Atwater, H. A. & Polman, A. Plasmonics for improved photovoltaic devices. *Nat Mater* **9**, 205-213 (2010).
- 23 Pala, R. A., White, J., Barnard, E., Liu, J. & Brongersma, M. L. Design of Plasmonic Thin - Film Solar Cells with Broadband Absorption Enhancements. *Adv Mater* **21**, 3504-3509 (2009).
- 24 Ferry, V. E., Sweatlock, L. A., Pacifici, D. & Atwater, H. A. Plasmonic nanostructure design for efficient light coupling into solar cells. *Nano Lett* **8**, 4391-4397 (2008).
- 25 Luk'yanchuk, B. *et al.* The Fano resonance in plasmonic nanostructures and metamaterials. *Nat Mater* **9**, 707-715 (2010).
- 26 Monticone, F. & Alu, A. Metamaterials and plasmonics: From nanoparticles to nanoantenna arrays, metasurfaces, and metamaterials. *Chinese Phys B* **23** (2014).

- 27 Liu, N. *et al.* Individual Nanoantennas Loaded with Three-Dimensional Optical Nanocircuits. *Nano Lett* **13**, 142-147 (2013).
- 28 Alu, A. & Engheta, N. Input impedance, nanocircuit loading, and radiation tuning of optical nanoantennas. *Phys Rev Lett* **101** (2008).
- 29 Chen, P. Y. & Alu, A. Optical nanoantenna arrays loaded with nonlinear materials. *Phys Rev B* **82** (2010).
- 30 Abasahl, B., Santschi, C. & Martin, O. J. F. Quantitative Extraction of Equivalent Lumped Circuit Elements for Complex Plasmonic Nanostructures. *Acs Photonics* **1**, 403-407 (2014).
- 31 Alu, A. & Engheta, N. Tuning the scattering response of optical nanoantennas with nanocircuit loads. *Nat Photonics* **2**, 307-310 (2008).
- 32 Neubrech, F. *et al.* Resonant Plasmonic and Vibrational Coupling in a Tailored Nanoantenna for Infrared Detection. *Phys Rev Lett* **101**, 157403 (2008).
- 33 Ditlbacher, H. *et al.* Silver Nanowires as Surface Plasmon Resonators. *Phys Rev Lett* **95**, 257403 (2005).
- 34 Shegai, T. *et al.* Unidirectional broadband light emission from supported plasmonic nanowires. *Nano Lett* **11**, 706-711 (2011).
- 35 Wang, H., Fu, K., Drezek, R. A. & Halas, N. J. Light scattering from spherical plasmonic nanoantennas: effects of nanoscale roughness. *Appl. Phys. B* **84**, 191-195 (2006).
- 36 Zou, S. & Schatz, G. C. Narrow plasmonic/photonic extinction and scattering line shapes for one and two dimensional silver nanoparticle arrays. *The Journal of Chemical Physics* **121**, 12606-12612 (2004).
- 37 Nikitin, A. G., Kabashin, A. V. & Dallaporta, H. Plasmonic resonances in diffractive arrays of gold nanoantennas: near and far field effects. *Opt Express* **20**, 27941-27952 (2012).
- 38 de Waele, R., Koenderink, A. F. & Polman, A. Tunable nanoscale localization of energy on plasmon particle arrays. *Nano Lett* **7**, 2004-2008 (2007).
- 39 Zhao, Y., Engheta, N. & Alù, A. Effects of shape and loading of optical nanoantennas on their sensitivity and radiation properties. *JOSA B* **28**, 1266-1274 (2011).
- 40 Berthelot, J. *et al.* Tuning of an optical dimer nanoantenna by electrically controlling its load impedance. *Nano Lett* **9**, 3914-3921 (2009).
- 41 Aizpurua, J. *et al.* Optical properties of gold nanorings. *Phys Rev Lett* **90** (2003).
- 42 Chang, T. Proximity effect in electron - beam lithography. *Journal of Vacuum Science & Technology* **12**, 1271-1275 (1975).
- 43 Rooks, M. *et al.* Low stress development of poly (methylmethacrylate) for high aspect ratio structures. *J Vac Sci Technol B* **20**, 2937-2941 (2002).
- 44 Hu, W. W., Sarveswaran, K., Lieberman, M. & Bernstein, G. H. Sub-10 nm electron beam lithography using cold development of poly (methylmethacrylate). *J Vac Sci Technol B* **22**, 1711-1716 (2004).
- 45 Ocola, L. & Stein, A. Effect of cold development on improvement in electron-beam nanopatterning resolution and line roughness. *J Vac Sci Technol B* **24**, 3061-3065 (2006).

## **Chapter 5**

### **Summary and Future Work**

#### **5.1 Summary**

The goal of this research was to realize plasmonic nanostructures with tailored optical properties by arranging nanoparticles building blocks on planar surfaces or within free-standing nanowire templates. To attain the desired properties, target nanostructures were first simulated utilizing either modified Generalized Mie Theory<sup>1</sup> (GMT) or finite element electromagnetic simulation methods. After optimized plasmonic structures were identified, several new hybrid top-down and bottom-up nanofabrication techniques were developed to overcome limitations of conventional top-down processes. The plasmonic structures studied in this thesis research included two-dimensional (2D) quasicrystal spherical Au nanoparticle arrays, freestanding self-organized one-dimensional (1D) spherical Au nanoparticle arrays, and nanoring-loaded plasmonic nanoantennas. All three types of structures were fabricated and optically characterized to compare theoretical modeling results with experimental measurement data.

In Chapter 2, quasicrystal plasmonic nanoparticle arrays with enhanced scattering and broadband properties were designed, fabricated, and characterized. A modified GMT modeling approach was adopted to quantitatively compare measured and simulated transmission spectra. Ammann-Beenker quasicrystal arrays were first fabricated using a conventional electron-beam lithography patterning and metal lift-off process. This produced cylindrical nanoparticles that differed from the spherical nanoparticles used in the simulation. A discrepancy was observed between the measured and simulated spectra. To investigate the origin of this difference, 2D periodic cylindrical Au nanoparticle arrays were fabricated using the same procedure. In this case,

strong agreement between theory and experiment was obtained when the measured thin-film dispersive optical properties and the cylindrical shape nanoparticles were included the simulation. This result suggested that the large discrepancy in the quasicrystal array was mainly due to difference in the particle shape between simulation and experiment.

To bridge the gap between simulation and experiment, a new nanofabrication approach that employed electron-beam lithography and subsequent thermal treatment was developed to synthesize 2D spherical plasmonic nanoparticle arrays. This technique combined the merits of lithographic patterning and laser heating approaches to realize Au nanoparticle arrays with control over sphere placement, diameter and spacing down to the nanometer scale. In this process, lithographically patterned cylindrical Au-Si nanoparticles are transformed into SiO<sub>2</sub> capped spherical Au particles when subjected to a high temperature thermal treatment in oxygen. The final spherical Au nanoparticle diameter and inter-particle spacing were determined entirely by the starting lithographic pattern and the evaporated Au volume.

A periodic plasmonic nanoparticle array as well as a broadband Ammann-Beenker and a multiband Penrose quasicrystal array were made using this hybrid fabrication process. Strong agreement was found between the transmission spectra determined by GMT simulation and experimental measurement. The inhomogeneous light distribution in the Ammann-Beenker and Penrose arrays in the far-field scattering map confirmed the optical properties of the two plasmonic quasicrystals. The transmission properties of Ammann-Beenker and Penrose arrays were also studied by modeling the interaction of the photonic resonance and the plasmonic resonance of Au nanoparticle, and each feature was associated with a specific real-space nanoparticle spacing in the array. This provided guidance for designing aperiodic arrays with tailored scattering properties.

The research in Chapter 3 developed a new fabrication process to create 1D arrays of freestanding spherical Au nanoparticle arrays encapsulated in a SiO<sub>2</sub> nanowire. This technique was based on the oxidation of Au-coated nanowires with predefined surface modulations, and lead to a

versatile platform for creating 1D Au nanoparticle arrays with highly tailorable and controllable particle diameters and interparticle spacing. Specifically, the resultant Au nanoparticle diameter was determined by the starting diameter of the Si nanowire and Au film thickness, while the interparticle spacing was controlled by the modulation of starting Si nanowire.

The optical properties of freestanding 1D plasmonic arrays composed 80nm diameter spherical Au nanoparticles with a 230nm interparticle spacing were characterized by optical absorption measurements on a randomly oriented ensemble of nanowire arrays as well as far-field optical scattering and electron energy loss spectrum (EELS) of individual nanoparticle arrays. Optical measurements of the ensemble exhibited a strong plasmonic response around 550nm, which agreed well with finite difference time domain (FDTD) simulations of the 1D arrays. The green color found in the far-field scattering map of a single nanowire array was consistent with the ensemble measurement result.

The plasmonic response of individual nanoparticle arrays was investigated by scanning transmission electron microscopy (STEM) and energy filtered transmission electron microscopy (EFTEM) measurements. A uniform plasmonic response around each nanoparticle in the array was observed by STEM, and weak coupling between nanoparticles within the array was demonstrated through EFTEM. The electron loss probability is determined by the photonic local density of states (LDOS)<sup>2</sup>, and  $|E|^2$  represents the scanning near field optical microscopy intensity<sup>3</sup> given by the LDOS<sup>4</sup>. Therefore, the weak coupling was consistent with the simulated electric field intensity distribution. This nanofabrication approach provides a scalable and low-cost route to fabricate freestanding plasmonic building blocks with independent control over the particle diameter and interparticle spacing.

Plasmonic structures with tailored multi-band scattering properties can be achieved by integrating more sophisticated nanoparticles, such as nanorings, into nanoantenna structures. In Chapter 4, air-loaded, solid nanoparticle-loaded and nanoring-loaded dimer nanoantennas were

studied to tailor the scattering properties of the structure. It was shown that the nanoring load element can be optimized to achieve a multiband scattering response, which is not possible for the air load and solid nanoparticle load structures. The three types of nanoantennas were fabricated by electron-beam patterning followed by metal lift-off. Simulation was used to optimize the process parameters to achieve the tight dimensional tolerances with resolution down to 10nm. The optical properties of the fabricated nanoantennas were characterized by far-field scattering measurements. The measured plasmonic response of all three structures, including the peak positions and bandwidth, exhibited strong qualitative agreement with simulation.

The origin of the multiband scattering response of the nanoring-loaded antennas was explored by comparing the simulated electric field, magnetic field and charge distribution to the air load and solid load cases. The field and charge distributions revealed that the short-wavelength resonance occurred when the three particles in the nanoring loaded array were coupled, while the long-wavelength response occurred when the particles were decoupled. This research demonstrated that the nanoantenna scattering response can be engineered by tailoring the properties of the nanoparticle load.

## **5.2 Recommendations for Future Work**

### **5.2.1 Three-Dimensional Nanoparticle Arrays**

In naturally occurring materials that have been used in conventional optical components, the permittivity tensor  $\epsilon$  and the permeability tensor  $\mu$  cannot be arbitrarily varied in three dimensions, limiting the components that can be made. Transformation optics offers the potential to greatly advance the design of optical components, enabling unprecedented flexibility in manipulating light as well as new functionalities, such as optical cloaking<sup>5</sup> and graded index



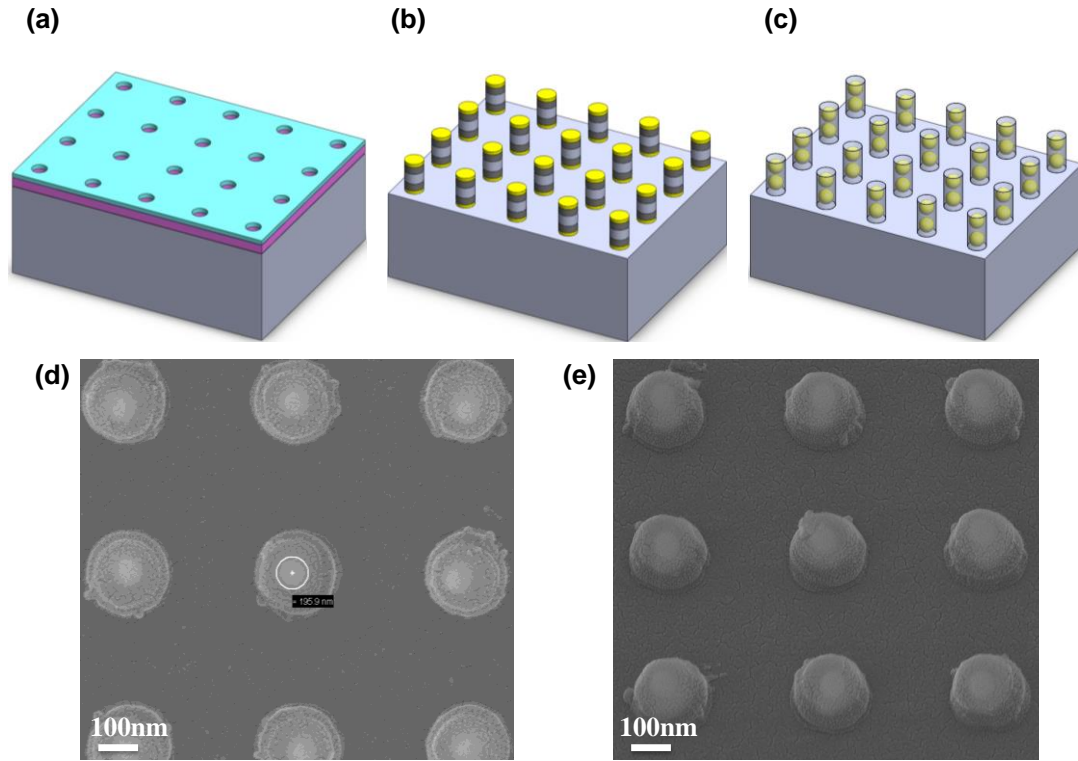


Figure 5-1. Schematic illustration of the nanofabrication process: (a) patterning the array features; (b) forming the Au/*a*-Si/SiO<sub>2</sub>/*a*-Si/Au cylindrical arrays by deposition and lift off; (c) forming the 3D spherical nanoparticle arrays by Au-enhanced oxidation; (d) Top view FESEM of fabricated 3D spherical nanoparticle arrays; (e) Cross-sectional FESEM of 3D spherical nanoparticle arrays.

lensing<sup>6,7</sup>. Although many interesting theoretical designs have been proposed, the experimental realization of these designs is lacking due to the challenges associated with fabricating inhomogeneous and anisotropic materials with nanoscale geometries. Controlled three-dimensional (3D) arrays of noble metal (*e.g.*, Au, Ag) offer a promising geometry to realize materials with these properties. By controlling the diameter of the nanoparticles and the spacing between adjacent nanoparticles in the array, values of  $\epsilon$  and  $\mu$  (and hence  $n_{eff}$ ) can be varied in 3D.

In Chapters 2 and 3, 2D uniform spherical nanoparticle periodic and quasicrystal arrays having properties that agree well with simulation were demonstrated. This process can be extended to 3D structures by patterning multilayer *a*-Si/Au stacks with SiO<sub>2</sub> spacers between each layer, as

illustrated in Figure 5-1. The process begins by using electron-beam lithography to define the array pattern, and electron-beam evaporation to deposit the Au/*a*-Si/SiO<sub>2</sub>/*a*-Si/Au stack. After the lift-off process, Au-enhanced oxidation is used to convert the deposited stack into a vertical array of Au nanoparticles.

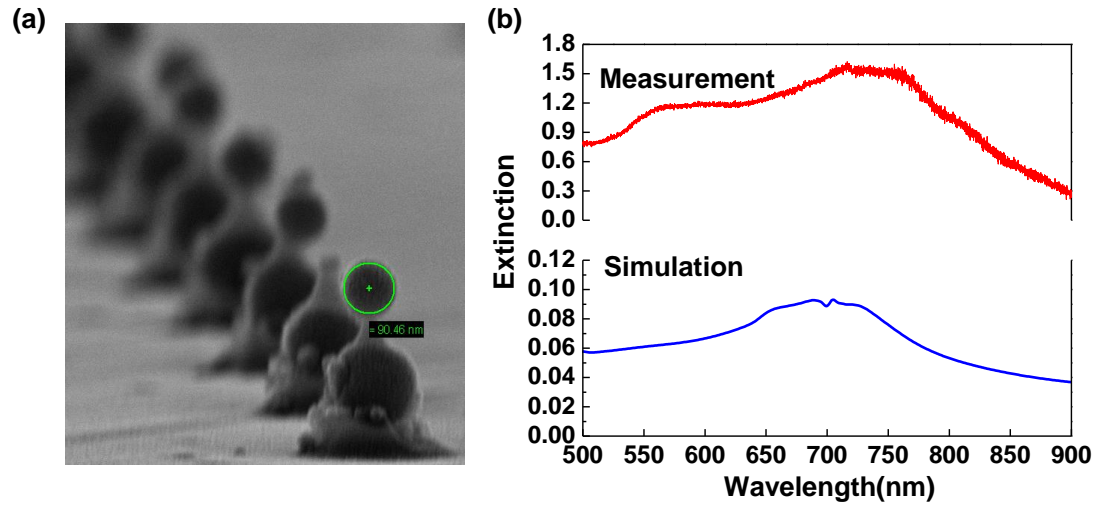


Figure 5-2. (a) FESEM image of the 3D spherical nanoparticle arrays that show the two Au nanoparticles stacked in the vertical direction; (b) Measured and simulated far-field scattering spectra for the 3D arrays.

A two-particle array was fabricated as a proof-of-concept, and top-view and cross-sectional field emission scanning electron microscope (FESEM) images of the resulting structures are shown in Figure 5-1 and Figure 5-2, respectively. This structure was fabricated by depositing a vertical stack composed of 10nm Au/30nm *a*-Si - 40nm SiO<sub>2</sub>/30nm *a*-Si/10nm Au. Following Au-enhanced oxidation, the diameter of top nanoparticle was 90nm and the bottom particle was 146nm. The interparticle spacing between the top and bottom particle was 60nm. The measured and simulated far-field scattering spectra of the 3D spherical Au nanoparticle arrays are compared Figure 5-2 (b), showing good qualitative agreement between the features in both. This demonstrates that the

process provides the control required to design and fabricate 3D structures for a desired optical function using the modified GMT method.

### 5.2.2 Alternative Patterning and Etching Processes for Plasmonic Nanoparticle Arrays

The preliminary research presented in this section explores alternative nanofabrication strategies to create Si-based nanowires with modulated surface texture for Au nanoparticle arrays. The process flow, which is illustrated in Figure 5-3 (a), creates vertically aligned arrays of surface-modulated nanowires using a deposited *a*-Si/*a*-SiGe stack and metal-assisted wet chemical etching (MACE) approach. The process begins by depositing an *a*-Si/*a*-SiGe superlattice structure on a fused silica substrate using plasma enhanced chemical vapor deposition (PECVD). The nanowire

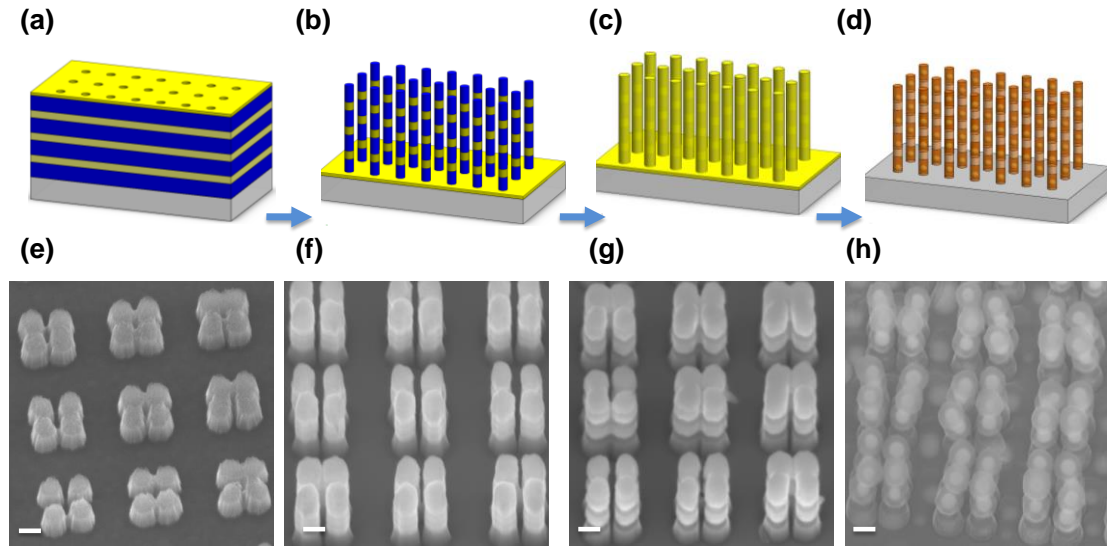


Figure 5-3. Schematic illustration of the fabrication process: (a) Deposit and lift-off Au mask; (b) MACE to form high aspect-ratio *a*-Si/*a*-SiGe superlattice nanowires; (c) Selective etching of the *a*-SiGe segment and conformal deposition of Au on the wire surface; (d) Au enhanced oxidation to form the 3D nanoparticle arrays. Preliminary experimental demonstration: (e) Photoresist features after electron-beam patterning; (f) *a*-Si/*a*-SiGe superlattice nanowires after etching; (g) *a*-Si/*a*-SiGe surface modulated nanowires after selective etching of the *a*-SiGe segment; (h) 3D nanoparticle arrays after Au-enhanced oxidation. Scale bar: 100nm.

array is formed by lithographic patterning and MACE, and then the *a*-SiGe layers are selectively etched with respect to the *a*-Si layers. This creates surface modulated nanowires with a modulation wavelength that is defined by the thickness of the superlattice layers. Following selective etching, a thin layer of Au is deposited on the surface of the wires, and the Au-enhanced oxidation process is used to convert the Au-coated surface modulated Si nanowires into SiO<sub>2</sub> encapsulated Au nanoparticle arrays.

The MACE process has been used previously to produce extreme aspect ratio Si and SiGe nanowire arrays for 3D integration<sup>8-12</sup>. In this method, nanoparticles or discontinuous thin films of Ag, Au or Pt have been used as a catalyst to increase the dissolution rate of Si in aqueous etchants. As illustrated in Figure 5-4<sup>9</sup>, the interface between the thin film of metal and the solution serves as the cathode, and the interface between the solution and Si serves as the anode. Etching begins when H<sub>2</sub>O<sub>2</sub> is catalytically reduced at the interface, and holes are created. The holes are then injected to the valence band of the Si, which leads to a hole-rich region of Si underneath the metal. Holes are then consumed at the solution/Si interface during oxidation of Si<sup>0</sup> to Si<sup>4+</sup> to produce soluble H<sub>2</sub>SiF<sub>6</sub>. The region beneath the metal is dissolved and catalyst drops onto the Si surface. This process creates nanowires with extreme aspect ratios.

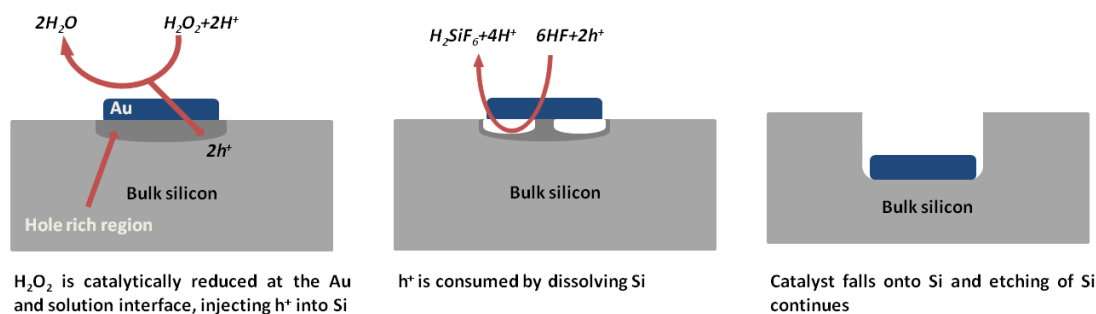


Figure 5-4. Schematic of the etching process. H<sub>2</sub>O<sub>2</sub> is reduced at the interface between metal and solution injecting holes (h) into the silicon valence band, creating a hole-rich region around the catalyst particle. The holes (h) are consumed by the oxidation of Si<sup>0</sup> to Si<sup>4+</sup> at the HF interface to form soluble H<sub>2</sub>SiF<sub>6</sub>. The metal travels into the silicon wafer as silicon around and beneath the metal is dissolved<sup>9</sup>.

In this preliminary research, a process was developed to create high-aspect ratio  $a$ -Si/ $a$ -SiGe nanowire arrays. The dense nanowire array was created by etching the structure using Au catalyst thin film in a solution of 4.6 M HF and 0.1 M H<sub>2</sub>O<sub>2</sub>. Once the nanowires were formed, the remaining Au metal at the base of the wires was removed by selective wet etching in Au etchant type TFA (Transene Company, Inc). The  $a$ -SiGe layers were selectively etched with respect to the  $a$ -Si layers using either a wet chemistry such as NH<sub>4</sub>OH, H<sub>2</sub>O<sub>2</sub> and H<sub>2</sub>O<sup>13</sup> or a dry process<sup>14</sup> with C<sub>2</sub>F<sub>6</sub> and O<sub>2</sub> to form the surface-modulated nanowire structure. The remainder of this process followed the procedure described in Chapter 3. A key advantage of this fabrication strategy is that the interparticle spacing is determined by the  $a$ -SiGe segment thickness, which can be controllably deposited with thicknesses of less than 10 nm. This enables the formation of Au nanoparticle arrays within the near-field coupling regime, which have important applications in surface enhanced Raman spectroscopy<sup>15</sup>, single molecular detection<sup>16</sup> and nonlinear optics<sup>17</sup>.

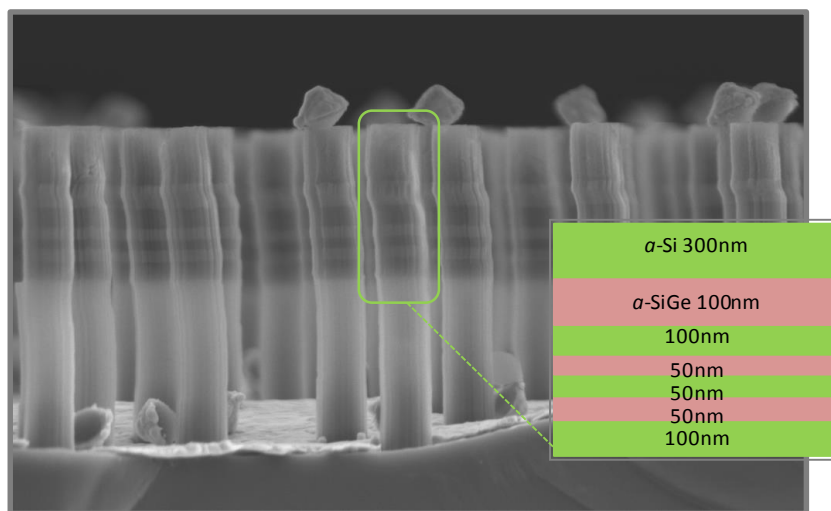


Figure 5-5. Preliminary result for  $a$ -Si/ $a$ -SiGe superlattice nanowire arrays with high aspect ratio.

Three-dimensional nanorod arrays can be realized using a similar nanofabrication process, as illustrated in Figure 5-6. Previous theoretical and experimental work has shown that 3D Yagi-Uda nanoantenna arrays<sup>18</sup> provide superior directional properties compared to a single planar optical antennas, particularly for emission and reception into the third dimension. However, the nanoantennas were fabricated using sequential top-down electron beam patterning and metal lift-off techniques. The process describe here has the potential to create 3D nanorod arrays in a single step without layer-by-layer patterning and deposition. Other building blocks for plasmonic structures such as nanorings and split rings could also be realized using this approach.

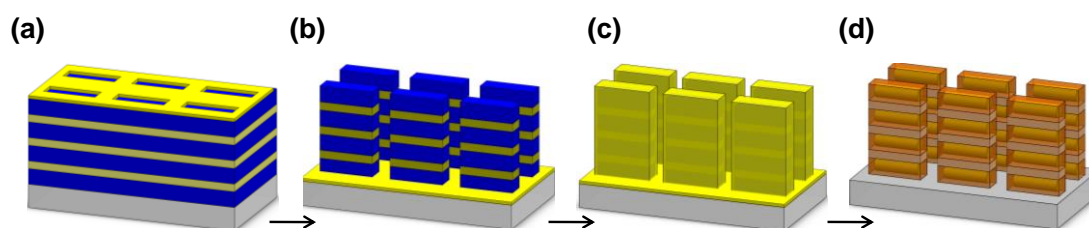


Figure 5-6. Schematic illustration of the fabrication process: (a) The Au deposition using the self-assembled polystyrene beads as a mask and removing the beads after the deposition via sonication; (b) MACE etch to form a high aspect-ratio *a*-Si/*a*-SiGe superlattice rectangle; (c) Selective etching the *a*-SiGe segment and conformally depositing Au on the rectangle surface; (d) Au enhanced oxidation to form the 3D nanoparticle arrays.

### 5.2.3 Multiplexed Nanoantenna Array as Bar-Codes

The nanoring-loaded dimer nanoantenna fabricated in Chapter 4 provided a multiband optical response. The structures showed that the two scattering peaks can be varied by changing the nanoring dimensions. Optical barcode structures with multiple peaks in the scattering spectrum can be realized by integrating different nanoparticle load elements. For example, core-shell nanoparticles<sup>19</sup> prepared by direct chemical synthesis methods could be used as the loading element. In this case, the plasmonic shell coating the non-plasmonic core gives the desired

properties, and can be scaled to smaller dimensions. With smaller dimensions, the displacement current across the nanoantenna is continuous, and it satisfies Kirchhoff voltage law. This allows the use of lumped equivalent circuit model<sup>20-24</sup> in the design of such structures, which simplifies the development of more advanced optical nanoantennas.

## 5.7 References

- 1 Namin, F. A., Wang, X. & Werner, D. H. Reflection and transmission coefficients for finite-sized aperiodic aggregates of spheres. *J. Opt. Soc. Am. B* **30**, 1008-1016 (2013).
- 2 de Abajo, F. J. G. Optical excitations in electron microscopy. *Rev Mod Phys* **82**, 209-275 (2010).
- 3 Babayan, Y. *et al.* Confining standing waves in optical corrals. *Acs Nano* **3**, 615-620 (2009).
- 4 Girard, C. Near fields in nanostructures. *Rep Prog Phys* **68**, 1883 (2005).
- 5 Cai, W. S., Chettiar, U. K., Kildishev, A. V. & Shalaev, V. M. Optical cloaking with metamaterials. *Nat Photonics* **1**, 224-227 (2007).
- 6 Driscoll, T. *et al.* Free-space microwave focusing by a negative-index gradient lens. *Appl Phys Lett* **88** (2006).
- 7 Greegor, R. B. *et al.* Simulation and testing of a graded negative index of refraction lens. *Appl Phys Lett* **87** (2005).
- 8 Chern, W. *et al.* Nonlithographic Patterning and Metal-Assisted Chemical Etching for Manufacturing of Tunable Light-Emitting Silicon Nanowire Arrays. *Nano Lett* **10**, 1582-1588 (2010).
- 9 Hildreth, O. J., Lin, W. & Wong, C. P. Effect of Catalyst Shape and Etchant Composition on Etching Direction in Metal-Assisted Chemical Etching of Silicon to Fabricate 3D Nanostructures. *Acs Nano* **3**, 4033-4042 (2009).
- 10 Peng, K. Q., Lu, A. J., Zhang, R. Q. & Lee, S. T. Motility of Metal Nanoparticles in Silicon and Induced Anisotropic Silicon Etching. *Adv Funct Mater* **18**, 3026-3035 (2008).
- 11 Chang, S. W., Chuang, V. P., Boles, S. T., Ross, C. A. & Thompson, C. V. Densely Packed Arrays of Ultra-High-Aspect-Ratio Silicon Nanowires Fabricated using Block-Copolymer Lithography and Metal-Assisted Etching. *Adv Funct Mater* **19**, 2495-2500 (2009).
- 12 Wang, X. *et al.* Arrayed Si/SiGe Nanowire and Heterostructure Formations via Au-Assisted Wet Chemical Etching Method. *Electrochem Solid St* **12**, K37-K40 (2009).
- 13 Carns, T. K., Tanner, M. O. & Wang, K. L. Chemical Etching of Si1-Xgex in Hf-H2o2-Ch3cooh. *J Electrochem Soc* **142**, 1260-1266 (1995).
- 14 Salvetat, T. *et al.* Comparison between three Si1-xGex versus Si selective etching processes. *ECS Transactions* **16**, 439-449 (2008).
- 15 Sawai, Y., Takimoto, B., Nabika, H., Ajito, K. & Murakoshi, K. Observation of a small number of molecules at a metal nanogap arrayed on a solid surface using surface-enhanced Raman scattering. *J Am Chem Soc* **129**, 1658-1662 (2007).

- 16 Acimovic, S. S., Kreuzer, M. P., González, M. U. & Quidant, R. Plasmon near-field coupling in metal dimers as a step toward single-molecule sensing. *Acs Nano* **3**, 1231-1237 (2009).
- 17 Marinica, D., Kazansky, A., Nordlander, P., Aizpurua, J. & Borisov, A. G. Quantum plasmonics: nonlinear effects in the field enhancement of a plasmonic nanoparticle dimer. *Nano Lett* **12**, 1333-1339 (2012).
- 18 Dregely, D. *et al.* 3D optical Yagi-Uda nanoantenna array. *Nat Commun* **2** (2011).
- 19 Panaretos, A. H. & Werner, D. H. Engineering the optical response of nanodipole antennas using equivalent circuit representations of core-shell particle loads. *J. Opt. Soc. Am. B* **30**, 2840-2848 (2013).
- 20 Liu, N. *et al.* Individual Nanoantennas Loaded with Three-Dimensional Optical Nanocircuits. *Nano Lett* **13**, 142-147 (2013).
- 21 Chen, P. Y. & Alu, A. Optical nanoantenna arrays loaded with nonlinear materials. *Phys Rev B* **82** (2010).
- 22 Alu, A. & Engheta, N. Tuning the scattering response of optical nanoantennas with nanocircuit loads. *Nat Photonics* **2**, 307-310 (2008).
- 23 Alu, A. & Engheta, N. Input impedance, nanocircuit loading, and radiation tuning of optical nanoantennas. *Phys Rev Lett* **101** (2008).
- 24 Abasahl, B., Santschi, C. & Martin, O. J. F. Quantitative Extraction of Equivalent Lumped Circuit Elements for Complex Plasmonic Nanostructures. *Acs Photonics* **1**, 403-407 (2014).



## Appendix A

### Periodic and Quasicrystal Nanoparticle Array Fabrication

#### A.1 Nanoparticle Array Fabrication and Characterization Processes

The two-dimensional nanoparticle arrays were prepared on fused silica substrates with an active area  $3.24 \times 3.24 \text{ mm}^2$ . The nanofabrication process for the cylindrical and spherical particle arrays began by spin coating a double layer electron-beam resist (Microchem PMGI and Microchem PMMA) onto a fused silica substrate. A 10nm thick of Au film was thermally evaporated onto the sample to minimize charging during the electron-beam exposure. Periodic of circular features with a pitch of 360nm were defined using electron-beam lithography (Vistec EBPG 5200) at 100keV with a dose of  $150 \mu\text{C}/\text{cm}^2$  for the cylindrical nanoparticles and  $300 \mu\text{C}/\text{cm}^2$  for the spherical nanoparticles. The patterns were developed using MIBK (Microchem):IPA (J.T. Baker)=1:3 for 2min and 101A developer (Microchem) for 1min, and an oxygen plasma descum was performed under 150sccm  $\text{O}_2$  with 200 W RF power for 15s (M4L). For the cylindrical particle array, Au (90nm) was deposited at a rate of  $1 \text{ \AA}/\text{s}$  with 1.5nm Ti serving as an adhesion layer. For the spherical particle array, a stack composed of *a*-Si (28nm)/ Au (60nm) films were deposited at a rate of  $1 \text{ \AA}/\text{s}$ . The deposited films were lifted off by dissolving the resist in Microposit Remover 1165 (Microchem). The spherical nanoparticle array was annealed in a 15-inch diameter quartz tube furnace at atmospheric pressure at  $850^\circ\text{C}$  in 90sccm oxygen flow for 3 hours. A  $3 \mu\text{m}$  thick layer of  $\text{SiO}_2$  was coated on the sample by plasma-enhanced chemical vapor deposition (Applied Materials P-5000). A second fused silica substrate was placed on the topside of the feature array and sealed with index matching oil (Nikon immersion oil for microscopy, Type A). The optical properties were characterized using a UV-VIS spectrometer (PerkinElmer) with a standard detector

accessory for normal specular transmission measurement. The measured transmittance was referenced to an unpatterned region of the same sample with the same area to determine the absolute transmission.

## A.2 Electromagnetic Simulation Method

Numerical simulations for the cylindrical and spherical Au nanoparticle arrays were performed by CST STUDIO SUITE. A unit cell composed of a single particle embedded in SiO<sub>2</sub> was used in the model. Periodic boundary conditions were applied at the x-z and y-z boundaries, and perfectly matched layers were applied on the top and bottom x-y faces. The simulation for Ammann-Beenker and Penrose arrays was implemented by GMT with an incident beam having a finite beam width. This was achieved by placing a circular aperture in front of a plane wave to obtain a beam width smaller than the array dimensions to avoid diffraction by the spheres at the edges of the lattice. For the Ammann-Beenker spherical nanoparticle quasicrystal array, the simulated array consisted of 401 Au spheres with a diameter of 135nm and minimum spacing of 300nm. At each wavelength  $\lambda$ , the aperture radius was set to  $a = 2\lambda$ . The distance of the aperture from the array ( $D$ ) was such that diffraction of the fields at the periphery of the array was avoided. This was determined using the first zero of the  $\frac{J_1(ka \sin \theta)}{\sin \theta}$ . Using this criteria, the Ammann-Beenker array was placed 22 $\mu$ m away from the aperture. For the Penrose nanoparticle array, the array consisted of 332 Au spheres with a diameter of 135nm and minimum spacing of 300nm. The Penrose array was placed 21 $\mu$ m away from the aperture.

### A.3 Optical Properties of Bulk Au and Au Thin Films

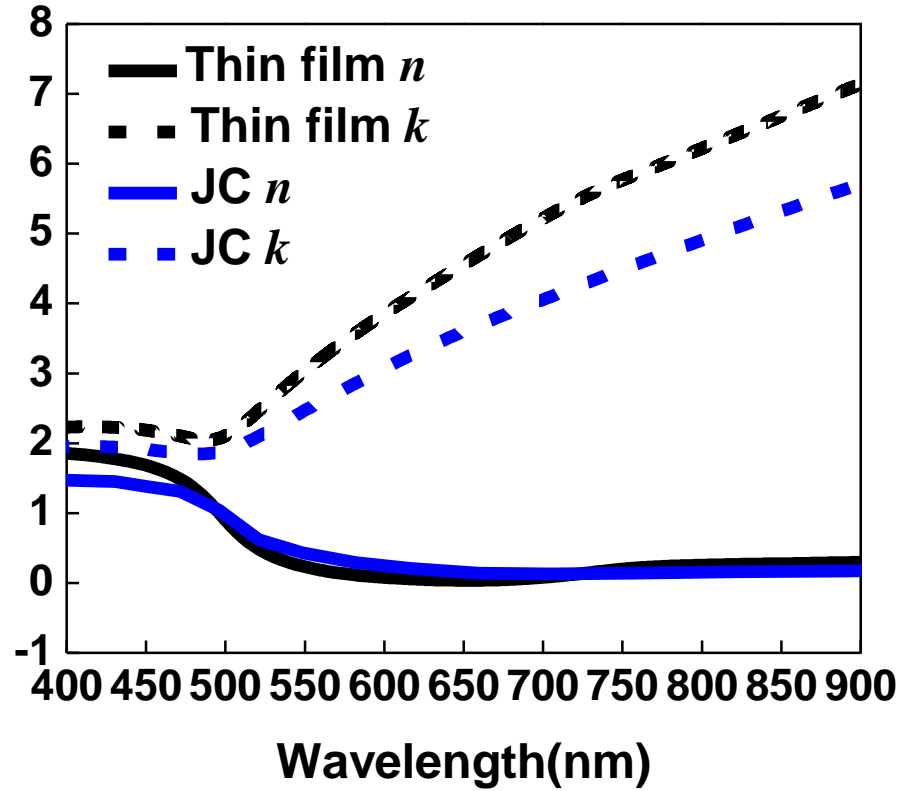


Figure A-2. The optical properties of Bulk Au and Au thin film. Johnson-Christy  $n$  (solid blue) and  $k$  (dash blue); Au thin film  $n$  (solid black) and  $k$  (dash black).

Figure A-1 plots the optical properties of bulk crystalline Au (Johnson-Christy) and measured thin film Au properties used in the electromagnetic simulation. The larger extinction coefficient  $k$  value of the thin film Au across the visible wavelength regime is due to the polycrystalline nature and surface roughness of the deposited film. The difference in the dispersive properties impacts the optical properties of the fabricated periodic and aperiodic Au nanoparticle arrays.

#### A.4 Polarization Dependent Measurements of the Periodic Array

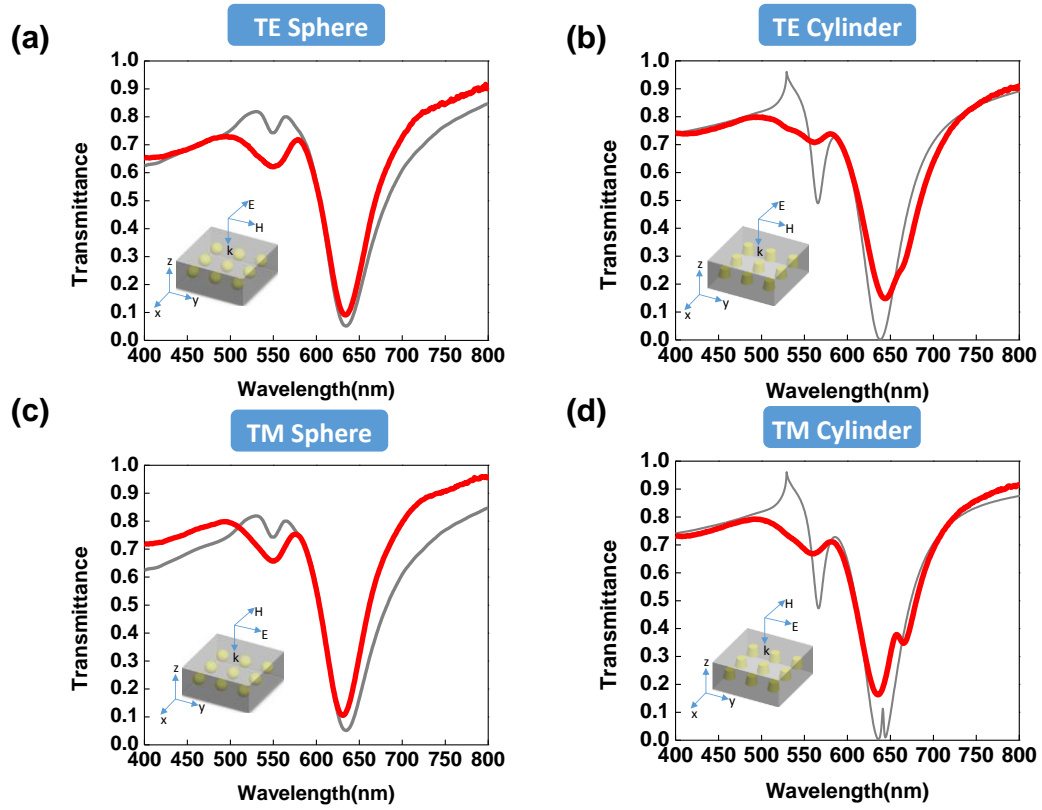


Figure A-2. Measured (red) and simulated (gray) transmission spectra of the periodic spherical nanoparticle arrays under transverse electric field (a) and transverse magnetic field (c) polarized light; Measured (red) and simulated (gray) transmission spectra of the periodic cylindrical nanoparticle arrays under transverse electric field (b) and transverse magnetic field (d) polarized light.

Normal incidence polarization dependent measurements of the 2D periodic spherical and cylindrical arrays are compared to the simulated response in Figure A-2 for the transverse electric mode and the transverse magnetic mode. The bulk JC Au properties are used in the simulation of the spherical nanoparticle arrays and the measured thin film Au properties are used for the cylindrical particle array.

## **Appendix B**

### **Self-Organized 1D Nanoparticle Arrays**

#### **B.1 Nanofabrication and Characterization Processes**

The fabrication process began by forming a template composed of dense arrays of Si microwires with 1.2 $\mu$ m nominal diameter and 3 $\mu$ m center-to-center spacing using projection lithography (GCA 8000 i-line stepper) followed by 2min Si deep reactive ion etch (DRIE, Alcatel Speeder 1000). The alternating dry etch and polymer deposition cycles were adjusted to controllably create the surface modulation – i.e., segments of concave regions and convex regions – on the wire surface. The cycle time of the etching and deposition steps was 3s/1.5s for 230nm, 7s/3.5s for 430nm and 10s/5s for 630nm modulation wavelengths. After DRIE, two cycles of wet oxidation at 1000°C for 90min and selective oxide removal in 5% hydrofluoric acid (JT Baker) were performed on the as-etched wire arrays to reduce the diameter of the wires down to 200nm. A third dry oxidation step was performed for 230nm surface modulation nanowires at 1000°C for 120min to further reduce the diameter to be less than 100nm. A thin Au film (5nm, 10nm, 20nm) was deposited on nanowires by thermal evaporation. The Au-coated nanowires were thermally oxidized at 850°C for 2 hours in pure O<sub>2</sub> with a flow rate of 0.8L/min. The absorption spectrum was acquired using a UV-VIS spectrometer (PerkinElmer). The transmitted beam energy was collected and referenced to the incident beam energy to extract the extinction spectra.

The surface plasmon studies were performed by scanning transmission electron microscopy (STEM), electron energy loss spectrum (EELS) and energy filtered transmission electron microscopy (EFTEM) imaging techniques using the TEAM-0.5 (NCEM, Berkeley, CA) TEM, which was operated at an accelerating voltage of 80kV. This system uses a high-brightness Schottky field emission electron source in combination with a Wein-filter monochromator and a

high resolution Gatan-Tridiem energy filter for EELS and EFTEM image acquisition. Under optimized experimental conditions, the energy spread in the electron beam was 0.12eV (FWHM). The STEM/EELS experiments were performed using a convergent electron probe that was approximately 1 nm in diameter, and the energy-loss spectrum at each pixel was acquired with an energy dispersion of 0.01eV/channel. The EFTEM images were acquired in the energy-loss spectral range 1eV - 6eV, using an energy selecting slit width of 0.2eV. The images were acquired with a spatial sampling of  $256 \times 256$  pixels and a field of view of  $1 \mu\text{m} \times 1 \mu\text{m}$ .

## B.2 Detailed Simulation Method

Numerical simulations for the cylindrical and spherical arrays were performed using Finite Difference Time Domain simulator (Lumerical). In the simulation setup, an array with five spherical Au particles was simulated. Each 80 nm diameter Au nanoparticle was encapsulated in  $\text{SiO}_2$ . The surface modulation was modeled as a two 115nm tall cones mirrored about the center plane of the nanoparticle, where the diameter at the base of the cone is 100nm and the diameter at the top of the cone is 60nm. The surrounding environment was isopropyl alcohol (IPA) with refractive index of 1.38. Perfectly matched layers were applied at the boundaries of the unit cell. The transmission spectra were collected using a power monitor that was placed 400nm away from the bottom of the array plane. The absorption was calculated by subtracting the transmittance from unity.

The electric field distribution of the nanoparticle array was simulated using COMSOL Multiphysics 4.2 RF module. The simulation setup for the array geometry is same as that used in the FDTD models. The surrounding environment was air with refractive index of  $n = 1$  and perfectly matched layers were applied at the boundaries of unit cell. The  $|E|^2$  was calculated and plotted.

# VITA

Yu Yuwen

## Education

- **The Pennsylvania State University**, University Park, PA    Sept., 2007-Aug., 2014 (expected)  
Ph.D. in Electrical Engineering, Minor in Statistics
- **Xi'an Jiaotong University**    Sept., 2003-July, 2007  
Bachelor of Electrical Engineering and Bachelor of Economics

## Publications

- **Yu A. Yuwen**, Frank Namin, Liu Liu, Anastasios H. Panaretos, Lei Kang, Douglas Werner, Theresa S. Mayer, "Synthesis of 2D Spherical Periodic and Aperiodic Nanoparticle Arrays via Au-enhanced Oxidation of Silicon," (in preparation).
- **Yu A. Yuwen**, Wenchong Hu, Seokho S. Yun, Theresa S. Mayer, Mahalingam Krishnamurthy, Kurt G. Eyink, "Self-organized freestanding one-dimensional Au nanoparticle arrays," (in preparation).
- **Yu A. Yuwen\***, Anastasios H. Panaretos\*, Douglas Werner, Theresa S. Mayer, "Tuning the optical response of a dimer using plasmonic nanoring loads," (in preparation) (\*equal contributions)
- Dongjin Won, Xiaojun Weng, **Yu A. Yuwen**, Yue Ke, Chito Kendrick, Haoting Shen, Theresa S. Mayer, Joan M. Redwing, "GaN growth on Si pillar arrays by metal organic chemical vapor deposition," *Journal of Crystal Growth* 370, 259 (2013).
- Y Ke, X Wang, X J Weng, C E Kendrick, **Y A Yu**, S M Eichfeld, H P Yoon, J M Redwing, T S Mayer and Y M Habib, "Single wire radial junction photovoltaic devices fabricated using aluminum catalyzed silicon nanowires," *Nanotechnology* 22, 445401(2011).
- Heayoung P. Yoon, **Yu A. Yuwen**, Chito E. Kendrick, Greg D. Barber, Nikolas J. Podraza, Joan M. Redwing, Thomas E. Mallouk, Christopher R. Wronski, and Theresa S. Mayer, "Enhanced conversion efficiencies for pillar array solar cells fabricated from crystalline silicon with short minority carrier diffusion lengths," *Appl. Phys. Lett* 96, 213503(2010).
- Chito E. Kendrick, Heayong P. Yoon, **Yu A. Yuwen**, Greg D. Barber, Haoting Shen, Thomas E. Mallouk, Elizabeth C. Dickey, Theresa S. Mayer, and Joan M. Redwing, "Radial junction silicon wire array solar cells fabricated by gold-catalyzed vapor-liquid-solid growth," *Appl. Phys. Lett* 97, 143108(2010).